Dependence of tropical cyclone intensification on latitude and sea surface temperature

Nina Črnivec

SIGILL·UNIVERSI·TAT·LUDOVIC·MAXIM·

Munich 2015

Abhängigkeit der Intensivierung tropischer Zyklone vom Breitengrad und von der Meeresoberflächentemperatur

Nina Črnivec

SIGILL. UNIVERSITAT. LUDOVIC. MAXIM.

München 2015

Dependence of tropical cyclone intensification on latitude and sea surface temperature

Nina Črnivec

MASTER THESIS
at the Faculty of Physics
Ludwig–Maximilians–University
Munich

by
Nina Črnivec
from Ljubljana, Slovenia

Munich, September 2015

First Examiner: Prof. Dr. Roger K. Smith
Second Examiner: Prof. Dr. George C. Craig
Submission Date: 30 September 2015

Abstract

The dependence of tropical cyclone intensification rate on latitude and sea surface temperature (SST) is examined in the prototype problem for tropical cyclone intensification on an f-plane using a three-dimensional, nonhydrostatic numerical model, namely the Bryan Cloud Model (CM1). The results of the recent paper by Smith *et al.* (2015), where the authors investigated why model tropical cyclones intensify more rapidly at low latitudes, are reproduced using a state-of-the-art CM1 model with higher horizontal resolution. Smith *et al.* used a different model in their study, namely the Pennsylvania State University/National Center for Atmospheric Research Mesoscale Model (MM5).

Evidence for a latitudinal dependence of tropical cyclone intensification in observations was found in a paper by Kaplan and DeMaria (2003). However, in reality, latitude is not the only environmental property affecting storm intensification. Because SST generally increases as the latitude decreases, it is an additional factor that may influence the latitudinal dependence found in the observations. To isolate and quantify the effects of changing the SST compared with those of changing the latitude on the rate of intensification of storms, nine numerical simulations are performed, taking combinations of three different latitudes (10°N, 20°N, 30°N) and three different SSTs (26°C, 28°C, 30°C). It is found that the dependence of intensification rate on latitude is largest when the SST is marginal for tropical cyclone intensification (26°C) and reduces in significance as the SST is increased. Further, at a given latitude, intensification begins earlier and the rate of intensification increases with increasing SST.

A physical explanation for this strong dependence of intensification on SST is offered. It is shown that, at a given latitude, an increase in the SST is accompanied by a significant increase in the surface water vapour fluxes. These higher fluxes result in higher values of near-surface moisture and equivalent potential temperature leading to a larger negative radial gradient of diabatic heating rate in the low to middle troposphere above the boundary layer. The larger radial gradient of heating rate leads to a stronger overturning circulation, which in turn gives rise to a stronger radial import of absolute angular momentum surfaces and therefore more rapid spin up. These arguments invoke the classical axisymmetric spin up mechanism. Nonaxisymmetric issues are touched upon briefly.

Zusammenfassung

In dieser Arbeit wird die Abhängigkeit der Intensivierungsrate tropischer Zyklone vom Breitengrad und von der Meeresoberflächentemperatur (SST, engl. Abkürzung) im Prototyp-Problem für die Intensivierung tropischer Zyklone auf der f-Ebene untersucht. Dazu werden numerische Experimente mittels eines dreidimensionalen, nicht-hydrostatischen Modells durchgeführt (Bryan Cloud Model; CM1). Die Ergebnisse der Arbeit von Smith *et al.* (2015), in der die Autoren untersuchten, warum tropische Wirbelstürme in numerischen Simulationen bei niedrigeren Breitengraden eine raschere Intensivierung aufweisen, werden anhand der CM1-Simulationen mit einer höheren horizontalen Auflösung reproduziert. In der Studie von Smith *et al.* wurde ein anderes numerisches Modell verwendet, nämlich das Pennsylvania State University/National Center for Atmospheric Research Mesoscale Model (MM5). Die Breitengradabhängigkeit der Intensivierung von tropischen Zyklonen wurde auch in einer Beobachtungsstudie nachgewiesen (Kaplan und DeMaria 2003). In der Realität gibt es jedoch noch weitere Umgebungsparameter, die die Sturmintensivierung beeinflussen. Da die Meeresoberflächentemperatur mit abnehmender geographischer Breite generell zunimmt, stellt sie einen zusätzlichen Faktor dar, der die in den Beobachtungsdaten nachgewiesene Breitengradabhängigkeit beeinflussen könnte. Um die Auswirkungen der SST-Änderung im Vergleich mit denen der Breitengradänderung auf die Intensivierungsrate zu isolieren und zu quantifizieren, werden neun numerische Simulationen durchgeführt. Hierbei werden jeweils drei verschiedene Werte geographischer Breite (10°N, 20°N, 30°N) mit jeweils drei verschiedenen Werten für Meeresoberflächentemperatur (26°C, 28°C, 30°C) kombiniert. Es ergibt sich, dass die Abhängigkeit der Intensivierungrate vom Breitengrad am stärksten ist, wenn die Meeresoberflächentemperatur den für die Intensivierung tropischer Wirbelstürme notwendigen Wert von mindestens 26°C aufweist und an Bedeutung verliert, wenn die Meeresoberflächentemperatur erhöht wird. Außerdem stellt es sich heraus, dass die Intensivierung früher beginnt und die Intensivierungsrate größer ist, wenn die Meeresoberflächentemperatur bei fest vorgegebener geographischer Breite erhöht wird. Bei einem bestimmten Breitengrad nehmen die latenten Wärmeflüsse mit zunehmender SST signifikant zu. Dies führt zu höheren Werten der bodennahen Feuchtigkeit und der potentiellen Äquivalenttemperatur, sowie einem erhöhten negativen radialen Gradienten der diabatischen Erwärmungsrate in der unteren und mittleren Troposphäre. Dadurch verstärkt sich die Sekundärzirkulation mit stärkerem Einströmen, welches zu einem stärkeren radialen Import von Gesamtdrehimpuls führt. Dies ruft eine raschere Intensivierung hervor. Die physikalischen Argumente basieren auf den klassischen achsensymmetrischen Intensivierungsmechanismus. Nicht-achsensymmetrische Aspekte werden kurz diskutiert.

Contents

1 Introduction **1**
- 1.1 Background and motivation 1
- 1.2 Structure of the thesis 4

2 Tropical cyclone intensification - Theoretical background **5**
- 2.1 Tropical cyclone dynamics 5
  - 2.1.1 The primary circulation 5
  - 2.1.2 The secondary circulation 7
- 2.2 Basic principles of vortex spin up 10
  - 2.2.1 Absolute angular momentum 10
  - 2.2.2 Conventional spin up mechanism 11
  - 2.2.3 Importance of the boundary layer in vortex intensification 11
  - 2.2.4 Boundary layer spin up mechanism 12
  - 2.2.5 Convergence of M during intensification 13
- 2.3 Limitations of axisymmetric theories 14
- 2.4 Prototype problem for tropical cyclone intensification 16

3 Numerical model **17**
- 3.1 The governing equations 17
- 3.2 Model configuration 20

4 Initialization problem **25**
- 4.1 Motivation 25
- 4.2 Determination of a balanced axisymmetric vortex 25
- 4.3 Implementation in the CM1 model 27

5 Dependence of tropical cyclone intensification on latitude **31**
- 5.1 Model results 31
- 5.2 Interpretation of the latitudinal dependence 33
  - 5.2.1 Thermodynamic issues 33
  - 5.2.2 Convective instability issue 35
  - 5.2.3 Diabatically-forced overturning circulation 37
  - 5.2.4 Rotational stiffness 39

5.2.5 Convective mass flux . . . 42
5.2.6 Boundary layer dynamics . . . 43
5.3 Synthesis . . . 45

6 Dependence of tropical cyclone intensification on SST 47
6.1 Model results . . . 49
6.1.1 Dependence on latitude for different SSTs . . . 49
6.1.2 Dependence on SST at different latitudes . . . 51
6.2 Interpretation of the SST dependence . . . 53
6.2.1 Boundary layer moisture budget . . . 53
6.2.2 Convective instability issue . . . 54
6.2.3 Diabatically-forced overturning circulation . . . 54
6.2.4 Convective mass flux . . . 60
6.3 Synthesis . . . 61
6.4 Two remaining issues . . . 62
6.4.1 Dependence of the ambient profile on the SST . . . 62
6.4.2 Nonaxisymmetric features . . . 64

7 Summary and Outlook 67
7.1 Summary . . . 67
7.2 Future work . . . 69

Bibliography 71

Eidesstattliche Erklärung 74

Acknowledgements 76

Chapter 1

Introduction

1.1 Background and motivation

Tropical cyclones are rotating, organized low pressure weather systems comprising of deep convective clouds, that form mostly over the warm tropical oceans. They are called hurricanes over the Atlantic Ocean, the East Pacific Ocean and the Caribbean Sea, and typhoons over the Western North Pacific Ocean. Their circulation is cyclonic, meaning that they rotate counterclockwise in the northern hemisphere and clockwise in the southern hemisphere. In contrast to the mid-latitude cyclones, the strongest horizontal winds in a tropical cyclone occur in a ring some tens of kilometres from the circulation centre near the earth's surface, typically at a height of 1 - 2 km. Above this altitude the tangential wind decreases with height and the vortex is warm-cored. Another special characteristic unique to mature tropical cyclones is a cloud-free region with comparatively light winds at the storm centre, called the eye. The eye is surrounded by a roughly circular ring of deep convective clouds, called the eyewall clouds, that slope outwards with height. At larger radii from the circulation centre, storms usually show spiral rainbands. Figure 1.1 shows a satellite view of the tropical cyclones Kilo, Ignacio and Jimena in the Pacific Ocean on August, 31, 2015.

Tropical cyclones are among nature's most powerful phenomena and those making landfall often cause extensive damage and loss of life. Thus a lot of work has been done throughout the history of tropical cyclone research, aiming to improve forecasts of these deadly storms. Tropical cyclone forecasting comprises two major challenges: (1) forecasting the track, and (2) forecasting the intensity. While the first has significantly improved over the last few decades, the latter still remains a challenge. Figure 1.2 shows National Hurricane Center (NHC) annual average track and intensity error trends for the Atlantic Basin tropical cyclones.

When studying tropical cyclone intensity change, one needs to define storm intensity first. The intensity of tropical cyclones is defined in terms of the maximum sustained wind speed at the standard meteorological height of 10 m, but the exact definition varies among forecast centres around the globe. In the United States, NHC uses 1-minute averaging

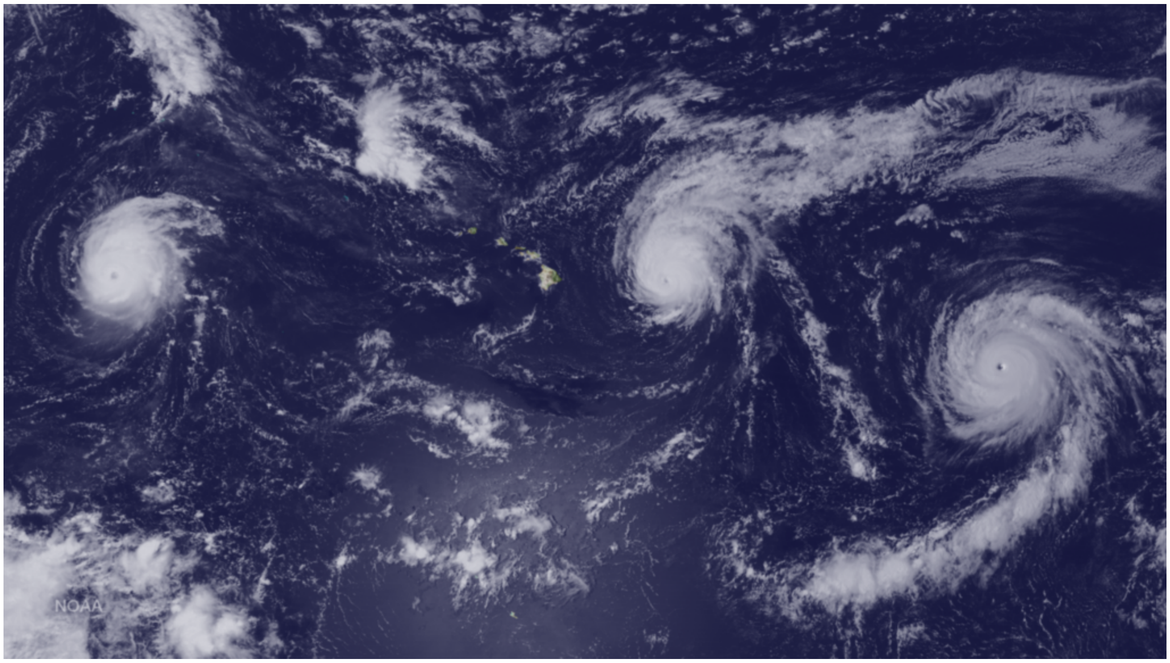

Figure 1.1: Tropical cyclones Kilo, Ignacio and Jimena in the Central Pacific on August, 31, 2015. Courtesy NOAA.

period for reporting sustained winds, while elsewhere normally a 10-minute average is used. Based on the value of the maximum sustained wind speed, tropical cyclones are classified into categories 1 - 5, according to the Saffir-Simpson intensity scale (see NHC website for more information[1]).

Tropical cyclones often undergo rapid intensification - a phase in which maximum sustained winds increase significantly in a short interval of time. NHC defines rapid intensification as an increase in storm intensity of at least 30 knots (35 mph; 55 km h^{-1}; 15 m s^{-1}) in a 24-hour period. A rapidly-intensifying tropical cyclone located in the vicinity of a populated coastal region poses a threat to human life and property. Therefore the improvement of understanding and forecasting of rapid intensification is of special interest.

There have been significant advances in numerical computing in the last few decades, making it possible to simulate tropical cyclones with high resolution numerical models. Nevertheless, important questions about the key physical processes involved in the tropical cyclone intensification and their coupling still remain unanswered. A better solution of the tropical cyclone intensification problem requires an extensive knowledge and comprehension of fluid dynamics and moist air thermodynamics. In order to improve the forecast models we need to understand the individual processes that operate in them. We need to identify and understand the essential processes that lead to rapid intensification of tropical cyclones and that may require an improved representation in the models.

---

[1] http://www.nhc.noaa.gov/aboutsshws.php

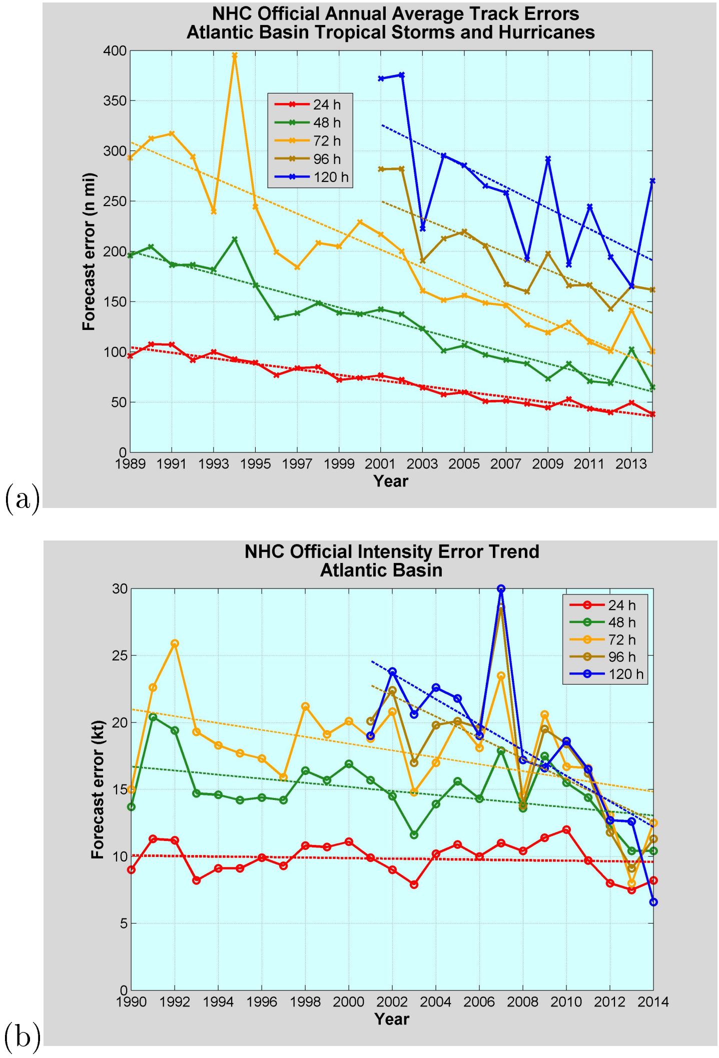

Figure 1.2: Annual average (a) track and (b) intensity errors for Atlantic basin tropical cyclones for the period 1989 (1990) - 2014, with least-squares trend lines superimposed. Courtesy NHC.

In this study we aim to gain a better understanding of the dependence of tropical cyclone intensification on latitude and sea surface temperature (SST). This work follows on from the recent study of Smith *et al.* (2015) who used The Pennsylvania State University/National Center for Atmospheric Research Mesoscale Model (MM5) to investigate why model tropical cyclones intensify more rapidly at low latitudes. The first goal of this thesis is to verify the results of Smith *et al.* (2015) using a state-of-the-art numerical model, namely Cloud Model 1 (CM1; Bryan and Fritsch 2002).

Evidence for latitudinal dependence of storm intensification can be found also in the observations of tropical cyclones. A comprehensive statistical analysis of Atlantic hurricanes by Kaplan and DeMaria (2003) indicates that a larger proportion of low-latitude storms undergo rapid intensification than storms at higher latitudes. However, latitude is not the only environmental property affecting storm intensification: vertical wind shear and sea surface temperature are additional effects that may be factors playing a role in the statistics. Since sea surface temperature typically increases as the latitude decreases, the question arises as to whether this effect might overwhelm the effects discussed by Smith *et al.* (2015) in relation to the observations. To address this question, we seek here to isolate and quantify the effect of changing the SST on the rate of intensification of storms in relation to the effect of changing the latitude. This represents the second goal of this thesis. A third aim is to find a physical explanation for the dependence of tropical cyclone intensification rate on sea surface temperature. To accomplish these tasks, we perform a total of nine numerical simulations taking combinations of three different latitudes (10°N, 20°N, 30°N) and three different sea surface temperatures (26°C, 28°C, 30°C). The basic structure of this work is outlined in the next section.

1.2 Structure of the thesis

In Chapter 2 we provide the theoretical background for understanding tropical cyclone intensification. Next, in Chapter 3, the numerical model and the experimental setup used in the current study are presented. As a new option for the initial state, a tropical-cyclone-like vortex was implemented in the model. A method for determining a balanced axisymmetric vortex in a compressible atmosphere as defined by Smith (2006) is introduced in Chapter 4, together with technical issues that arose during its implementation in the model. The latitudinal dependence of tropical cyclone intensification is discussed in Chapter 5, following the work of Smith *et al.* (2015). In Chapter 6 we present a series of results of all nine numerical simulations concurrently, aiming to quantify the effect of changing SST relative to the effect of changing the latitude on tropical cyclone intensification rate. The focus of this chapter is the dependence of tropical cyclone intensification on SST. A physical explanation for this dependence is offered, based on an axisymmetric perspective. Nonaxisymmetric aspects are briefly discussed also. Chapter 7 summarizes this work and gives an outlook for future studies.

Chapter 2

Tropical cyclone intensification - Theoretical background

In this chapter we provide a theoretical background for understanding the tropical cyclone intensification problem. We begin by reviewing the underlying balance theory for the structure and dynamics of tropical cyclones. Next, we present the basic principles of tropical cyclone spin up, based on an axisymmetric view. We introduce briefly a new paradigm for the intensification, in which also the nonaxisymmetric processes play an important role. Lastly, we outline a basic thought experiment for tropical cyclone intensification.

2.1 Tropical cyclone dynamics

2.1.1 The primary circulation

We consider the full set of governing equations for frictional flow in a rotating frame of reference on an f-plane in cylindrical polar coordinates (r, λ, z). The primitive equations of motion comprise the three components of momentum equation (Eqs. 2.1, 2.2, 2.3), the continuity equation (Eq. 2.4), the thermodynamic equation (Eq. 2.5) and the equation of state (Eq. 2.6) that are expressed as:

$$\frac{\partial u}{\partial t} + u\frac{\partial u}{\partial r} + \frac{v}{r}\frac{\partial u}{\partial \lambda} + w\frac{\partial u}{\partial z} - \frac{v^2}{r} - fv = -\frac{1}{\rho}\frac{\partial p}{\partial r} + F_r, \tag{2.1}$$

$$\frac{\partial v}{\partial t} + u\frac{\partial v}{\partial r} + \frac{v}{r}\frac{\partial v}{\partial \lambda} + w\frac{\partial v}{\partial z} + \frac{uv}{r} + fu = -\frac{1}{\rho r}\frac{\partial p}{\partial \lambda} + F_\lambda, \tag{2.2}$$

$$\frac{\partial w}{\partial t} + u\frac{\partial w}{\partial r} + \frac{v}{r}\frac{\partial w}{\partial \lambda} + w\frac{\partial w}{\partial z} = -\frac{1}{\rho}\frac{\partial p}{\partial z} - g + F_z, \tag{2.3}$$

$$\frac{\partial \rho}{\partial t} + \frac{1}{r}\frac{\partial(\rho r u)}{\partial r} + \frac{1}{r}\frac{\partial(\rho v)}{\partial \lambda} + \frac{\partial(\rho w)}{\partial z} = 0, \tag{2.4}$$

$$\frac{\partial \theta}{\partial t} + u\frac{\partial \theta}{\partial r} + \frac{v}{r}\frac{\partial \theta}{\partial \lambda} + w\frac{\partial \theta}{\partial z} = \Theta, \tag{2.5}$$

$$p = \rho R_d T. \tag{2.6}$$

The variables u, v and w represent the velocity components in the radial, azimuthal and vertical direction, respectively. The variables p, ρ, T and θ are the total pressure, density, temperature and potential temperature, respectively. Terms F_r, F_λ, F_z represent frictional terms. Further, g is the acceleration due to gravity, Θ is the diabatic heating rate, R_d is the gas constant of dry air and f is the Coriolis parameter ($2\Omega \sin\varphi$, where Ω is the angular velocity of Earth's rotation and φ is the latitude).

A simple picture of tropical cyclone structure can be obtained by assuming that the flow $\vec{v} = (u, v, w)$ is steady ($\partial/\partial t = 0$), axisymmetric ($\partial/\partial\lambda = 0$), frictionless ($F_r = F_\lambda = F_z = 0$) and purely tangential $\vec{v} = (0, v, 0)$. Furthermore we assume there is no diabatic heating and that the vortex is stationary. Then, from the radial momentum equation (Eq. 2.1) we obtain the gradient wind equation, which expresses the balance of the pressure gradient force per unit mass with the sum of the centrifugal and Coriolis forces per unit mass:

$$\frac{1}{\rho}\frac{\partial p}{\partial r} = C, \tag{2.7}$$

where:

$$C = \frac{v^2}{r} + fv. \tag{2.8}$$

Similarly, from the vertical momentum equation (Eq. 2.3), we obtain the hydrostatic equation:

$$\frac{1}{\rho}\frac{\partial p}{\partial z} = -g. \tag{2.9}$$

The circulation determined by the Eqs. (2.7) and (2.9) is referred to as the *primary circulation* of a tropical cyclone. It is simply the tangential flow rotating around the central axis, satisfying the hydrostatic and gradient wind balance. The primary circulation of a tropical cyclone is shown schematically in Figure 2.1.

Eliminating the pressure from the Eqs. (2.7) and (2.9) by cross-differentiation gives the unapproximated form of the thermal wind equation, which relates the radial and vertical density gradients to the vertical gradient of the tangential wind:

$$\frac{\partial}{\partial r}\ln\rho + \frac{C}{g}\frac{\partial}{\partial z}\ln\rho = -\frac{1}{g}\frac{\partial C}{\partial z}. \tag{2.10}$$

Thus by definition, the primary circulation of a tropical cyclone satisfies thermal wind balance. We will return to this equation in Chapter 4.

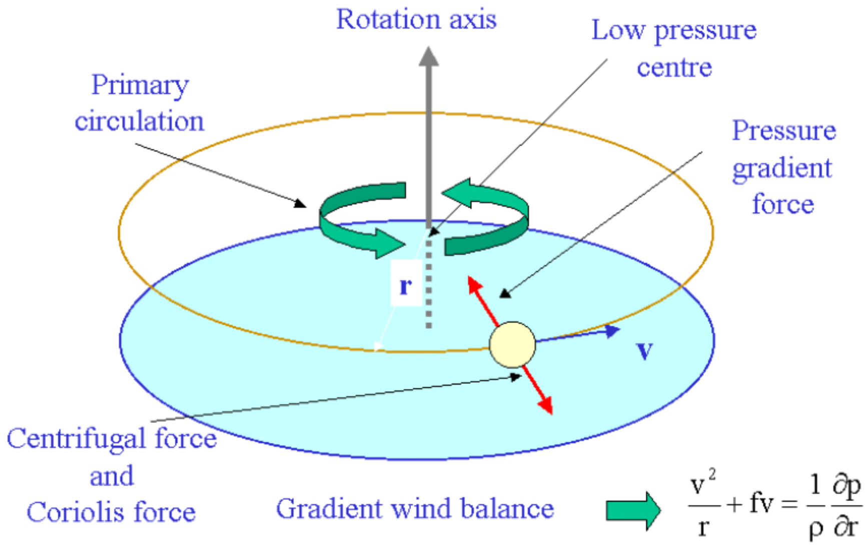
Rotation axis
Low pressure centre
Primary circulation
Pressure gradient force
r
v
Centrifugal force and Coriolis force
Gradient wind balance
$\frac{v^2}{r} + fv = \frac{1}{\rho}\frac{\partial p}{\partial r}$

Figure 2.1: Schematic illustrating the gradient wind balance in the primary circulation of a tropical cyclone. Courtesy R. K. Smith.

2.1.2 The secondary circulation

Observations and numerical model simulations of tropical cyclones show air parcels spiralling inwards in the lower layers, upwards near the circulation centre and outwards in the upper layers of the vortex. Thus there is a circulation in the vertical (r, z) plane that is superposed on the primary circulation from the previous section. This circulation is referred to as the *secondary circulation*, also overturning circulation or *in-up-and-out* circulation. The components of the flow in the radial and vertical directions (u, w) are determined by the scalar streamfunction ψ:

$$u = -\frac{1}{\rho r}\frac{\partial \psi}{\partial z}, \tag{2.11}$$

$$w = \frac{1}{\rho r}\frac{\partial \psi}{\partial r}. \tag{2.12}$$

These expressions for radial and vertical velocity ensure that the steady axisymmetric form of the continuity equation (Eq. 2.13) is satisfied;

$$\frac{\partial}{\partial r}(\rho r u) + \frac{\partial}{\partial z}(\rho r w) = 0. \tag{2.13}$$

The next step would be to derive the equation for the streamfunction ψ. The derivation of this equation is long, but mathematically straightforward. First, the thermal wind equation is differentiated with respect to time and the azimuthal momentum and thermodynamic equations are used to eliminate time derivatives. The derivation is simplified by expressing the azimuthal and thermodynamic equations in the following forms - Eqs. (2.14) and (2.15), respectively:

$$\frac{\partial v}{\partial t} + u(\zeta + f) + wS = \dot{V}, \tag{2.14}$$

where $\zeta = (1/r)(\partial(rv)/\partial r)$ is the vertical component of relative vorticity at radius r, $S \equiv \partial v/\partial z$ and $\dot{V}$ is a tangential momentum source term;

$$\frac{\partial \chi}{\partial t} + u\frac{\partial \chi}{\partial r} + w\frac{\partial \chi}{\partial z} = -\chi^2\dot{\theta}, \tag{2.15}$$

where $\chi \equiv 1/\theta$ and $\dot{\theta} = \frac{d\theta}{dt}$ is the diabatic heating rate for the azimuthally-averaged potential temperature. It can be shown that the diagnostic equation for the streamfunction of the secondary circulation, commonly known as the Sawyer-Eliassen equation, has the following form:

$$\frac{\partial}{\partial r}\left\{g\frac{\partial \chi}{\partial z}\frac{1}{\rho r}\frac{\partial \psi}{\partial r} + \frac{\partial}{\partial z}(\chi C)\frac{1}{\rho r}\frac{\partial \psi}{\partial z}\right\} - \frac{\partial}{\partial z}\left\{\left(C\frac{\partial \chi}{\partial r} + \chi\xi(\zeta + f)\right)\frac{1}{\rho r}\frac{\partial \psi}{\partial z} - \frac{\partial}{\partial z}(\chi C)\frac{1}{\rho r}\frac{\partial \psi}{\partial r}\right\}$$

$$= g\frac{\partial Q}{\partial r} + \frac{\partial}{\partial z}(CQ) + \frac{\partial}{\partial z}(\chi\xi\dot{V}), \tag{2.16}$$

where $Q \equiv -\chi^2\dot{\theta}$ and $\xi \equiv 2v/r + f$ is twice the local absolute angular momentum at radius r. Equation (2.16) provides a basis for the development of a theory for the evolution of a rapidly-rotating vortex that is undergoing slow forcing by heat and azimuthal momentum sources. The Sawyer-Eliassen balance equation is a linear second-order partial differential equation for ψ, which can be solved numerically, if suitable boundary conditions on ψ are specified (e.g., $\psi = 0$ along the domain boundary), if the discriminant of the equation is positive meaning that the equation is elliptic and if the forcing terms on the right-hand side (RHS) of the equation are known. Precisely, these forcing terms are the radial and vertical gradients of the diabatic heating rate and the vertical gradient of the azimuthal momentum forcing.

The Sawyer-Eliassen equation is liner in ψ, which enables solutions for the transverse streamfunction by summing the solutions forced individually by the three forcing terms on the right-hand side. The Sawyer-Eliassen equation contains three physically-meaningfull parameters, that contain some information about the form of the solutions. These are static stability characterized by N^2, where N is the Brunt-Väisälä frequency, inertial stability I^2 (i.e., centrifugal stability or stability in the radial direction) and baroclinity B. They are defined as follows:

$$N^2 = \frac{g}{\theta}\frac{\partial \theta}{\partial z} = -g\frac{\partial ln\chi}{\partial z}, \tag{2.17}$$

$$I^2 = \frac{1}{r^3}\frac{\partial M^2}{\partial r} = \xi(\zeta + f), \tag{2.18}$$

$$B = \frac{1}{r^3}\frac{\partial M^2}{\partial z} = \xi S, \tag{2.19}$$

where M is the absolute angular momentum, an important quantity that will be discussed in more detail in section 2.2.

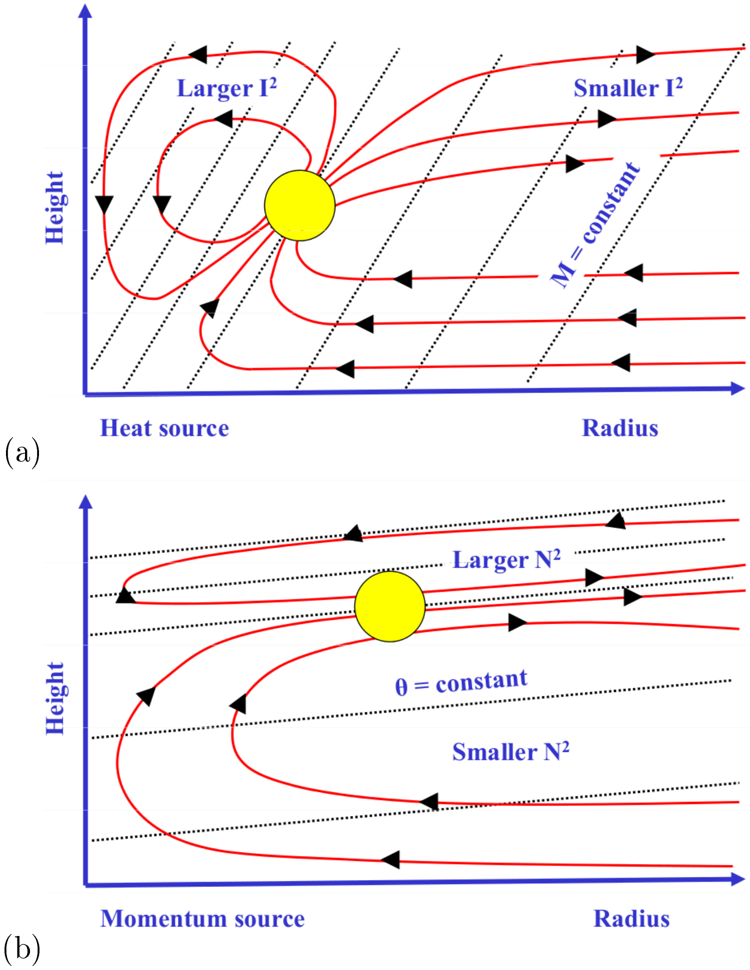
Larger I²
Smaller I²
Height
M = constant
Heat source
Radius
(a)
Larger N²
θ = constant
Smaller N²
Height
Momentum source
Radius
(b)

Figure 2.2: Schematic showing the circulation in the height-radius plane when the Sawyer-Eliassen equation is solved for a positive point source of heating (panel a) and a positive point source of momentum (panel b) in regions with different inertial and static stability. Adapted from Willoughby (1995).

Figure 2.2 shows examples of the solutions of Eq. (2.16), depicting the overturning circulation induced by point sources of heat (panel a) and absolute angular momentum (panel b) in a balanced vortex in a partially bounded domain (Shapiro and Willoughby 1982). Both sources are assumed to be positive in Figure 2.2. As noted by Shapiro and Willoughby, op. cit., the streamlines form two counter-rotating cells of circulation that extend well outside the source in both cases. The flow emerges from the source, spreads outwards through a large surrounding area, and finally converges back into the source. In the vicinity of the heat source, the secondary circulation follows a surface of constant absolute angular momentum and is thus primarily vertical. In the region close to momentum source, the circulation is congruent to surfaces of constant potential temperature (i.e., isentropic surfaces) and is therefore primarily horizontal.

A scale analysis of the radial and vertical momentum equations dictates that the flow satisfies gradient and hydrostatic balance, i.e., thermal wind balance (Willoughby 1979). The imposed sources of heat and momentum drive the flow away from balance. Thus the secondary circulation represents a balanced response of the vortex as it opposes the effects of these forcing mechanisms. Precisely, the flow through the source is directed so that it opposes the effect of forcing. For example, the induced flow (i.e., rising air) through the heat source causes an adiabatic cooling tendency that tries to oppose the effects of heating. Similarly, the induced outflow through the positive absolute angular momentum source in Figure 2.2b tends to reduce the local increase of M in the source region (Willoughby 1995).

Another feature of the Sawyer-Eliassen solutions can be examined with the aid of Figure 2.2, where, inter alia, the regions with different magnitudes of inertial and static stability are marked, as typically observed in tropical-cyclone-like vortices. For example, there is high inertial stability in the inner-core region of the vortex, which implies a smaller radial scale of the overturning circulation in this part compared with the radial extent of the secondary circulation in the outer regions of the vortex. While the inertial stability affects the radial scale of the overturning circulation cells, the static stability determines their vertical extent. For a fixed inertial stability, the circulation cells tend to be deeper when N^2 is small.

The above findings about the Sawyer-Eliassen solutions for idealized point sources can be qualitatively applied also to more realistic source distributions of heat and momentum as typically found in tropical cyclones. The dominant heat source in tropical cyclones is associated with deep convection in the eyewall region (i.e., latent heat release in deep convective clouds) and induces inflow in the lower troposphere. A negative or anticyclonic source of momentum is the surface friction, which induces inflow in the boundary layer and outflow in a layer above it. The effects of these convectively- and frictionally-induced circulation branches on the vortex spin up will be discussed further in section 2.2.

2.2 Basic principles of vortex spin up

2.2.1 Absolute angular momentum

An important quantity in the analysis of tropical cyclone intensification is the absolute angular momentum. The absolute angular momentum per unit mass (M) of an air parcel on a rotating planet is defined by the following expression:

$$M = rv + \frac{1}{2}fr^2. \tag{2.20}$$

The first term on the RHS of Eq. (2.20) is the relative angular momentum of the circulation with respect to the axis of rotation. The second term is the component of planetary angular momentum that projects onto the local vertical (i.e., the axis of rotation). An important conservation equation can be derived from the tangential momentum equation (Eq. 2.2). We multiply this equation by r and after a little manipulation we obtain:

$$\frac{\partial M}{\partial t} + u\frac{\partial M}{\partial r} + \frac{v}{r}\frac{\partial M}{\partial \lambda} + w\frac{\partial M}{\partial z} = -\frac{1}{\rho}\frac{\partial p}{\partial \lambda} + rF_{\lambda}. \tag{2.21}$$

If the flow is axisymmetric ($\partial/\partial\lambda = 0$) and frictionless ($F_{\lambda} = 0$), Eq. (2.21) reduces to:

$$\frac{dM}{dt} = 0, \tag{2.22}$$

where:

$$\frac{d}{dt} = \frac{\partial}{\partial t} + u\frac{\partial}{\partial r} + w\frac{\partial}{\partial z}. \tag{2.23}$$

Equation (2.22) states that in axisymmetric theory, assuming there is no friction, absolute angular momentum is materially conserved. The conservation of M above the boundary layer in tropical cyclones is a key element for understanding the tropical cyclone intensification and the essential feature of the conventional spin up mechanism discussed in the next section.

2.2.2 Conventional spin up mechanism

In the presence of latent heat release associated with deep convection, the radial and vertical gradients of the diabatic heating rate induce radial inflow in the lower and mid troposphere. The vortex spins up as air parcels move to smaller radii while conserving their absolute angular momentum. The latter follows immediately from Eqs. (2.20) and (2.22). Alternatively, we can rewrite Eq. (2.20) to get an expression for the tangential velocity:

$$v = \frac{M}{r} - \frac{1}{2}fr. \tag{2.24}$$

When M is materially-conserved, both terms in Eq. (2.24) lead to an increase in v as r decreases, and vice versa. The acceleration of tangential winds by the convectively-induced inflow above the boundary layer, where absolute angular momentum is approximately conserved, forms the basis of the *conventional spin up mechanism* (Ooyama 1969, Montgomery and Smith 2014). It is assumed that the inner-region deep convection can be maintained.

2.2.3 Importance of the boundary layer in vortex intensification

The tropical cyclone boundary layer is a shallow layer adjacent to the ocean surface or land, typically about 1 km deep, in which gradient wind balance is disrupted by friction. Frictional stresses reduce the tangential wind speed and thereby the centrifugal and Coriolis forces. On the other hand, a scale analysis of the momentum equations shows that the radial pressure gradient in the boundary layer is essentially the same as that above it. The resulting imbalance of forces in the radial direction leads to a net inward force, called the agradient force, that drives an inflow in the boundary layer. This boundary layer inflow has a number of effects on vortex intensification:

(1) Negative dynamical role

Frictionally-induced inflow in the boundary layer is accompanied by the outflow in the layer above it. This leads to a spin down above the boundary layer as a result of the conservation of M in this region. This mechanism for vortex spin down involving the frictionally-induced secondary circulation is the primary one in a vortex at high Reynolds number[1] and overshadows the direct effect of the frictional torque on the tangential wind in the friction layer (Montgomery and Smith 2014, Greenspan and Howard 1963).

(2) Positive thermodynamical role

The evaporation from the ocean surface is the primary source of moisture that fuels convection. The frictional convergence in the moist surface boundary layer leads to an abundant supply of moisture in the inner-core region. The increased moisture amount in the boundary layer inner-core increases the latent heat release in deep convective clouds. From here on, the vortex intensification above the boundary layer occurs via the conventional spin up mechanism, assuming that the inner-core convection can be maintained.

The effects of the boundary layer summarized in paragraphs (1) and (2) encompass the general view of the boundary layer in the early paradigms for tropical cyclone intensification. It was believed that the boundary layer plays an important role in converging moisture to sustain deep convection, but its dynamical role is to oppose spin up (Ooyama 1969).

(3) Positive dynamical role

Recently, a new dynamical role of the boundary layer inflow was recognized (Smith *et al.* 2009). It is known as the boundary layer spin up mechanism and it is the focus of the next section.

2.2.4 Boundary layer spin up mechanism

The frictionally-induced inflow, if sufficiently strong, directly causes spin up of tangential winds in the boundary layer. Although M is not conserved in the friction layer, we can still apply the formula for tangential velocity from the section 2.2.2 (Eq. 2.24) with the following consideration: If the inflow is sufficiently strong, meaning that the air parcels are brought towards the storm centre relatively quickly, before they have lost too much of their M by spiralling around, then there is a possibility that M may not decrease as rapidly as the radius following an inward moving air parcel. In this case again both terms in Eq. (2.24) lead to an increase in the tangential wind speed. This raises the possibility that the tangential wind in the boundary layer may exceed that above it in the inner-core region of tropical cyclones. The observations show that this is often the case in reality, where maximum tangential winds occur slightly below the top of the boundary layer (Kepert 2006a, Montgomery *et al.* 2006).

---

[1] The Reynolds number is a nondimensional parameter that identifies the relative importance of the inertial and viscous terms in the Navier Stokes equations. It is defined as: $Re = UL/\nu$, where U is the velocity scale, L is the horizontal length scale and ν is the kinematic viscosity of the fluid.

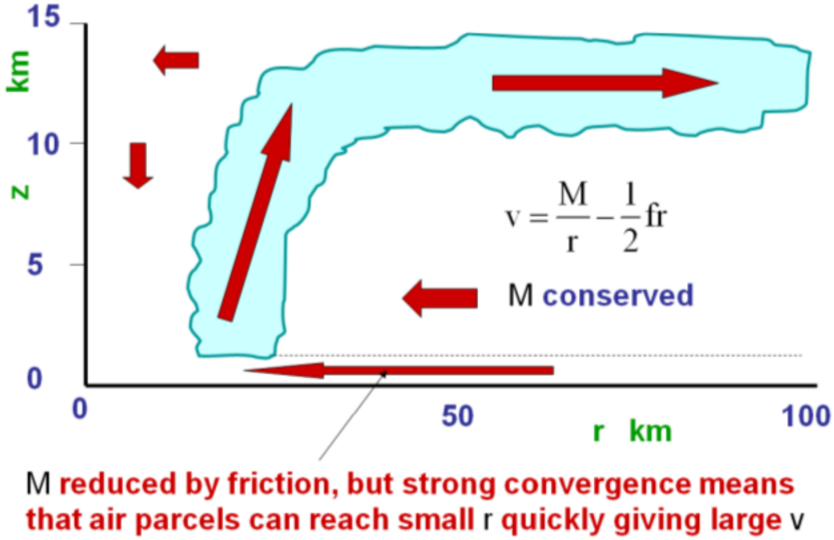
15
10
5
0
z km
0
50
100
r km
$v = \frac{M}{r} - \frac{1}{2}fr$
M conserved
M reduced by friction, but strong convergence means that air parcels can reach small r quickly giving large v

Figure 2.3: Schematic illustrating the two mechanisms for tropical cyclone intensification: The conventional spin up mechanism based on the conservation of M above the boundary layer, and the boundary layer spin up mechanism, signifying the spin up of tangential winds within the boundary layer, if the frictional inflow is sufficiently strong. Courtesy R. K. Smith.

2.2.5 Convergence of M during intensification

The conventional mechanism and boundary layer mechanism for the spin up of the azimuthal-mean tangential circulation of a tropical cyclone both involve radial convergence of absolute angular momentum. In Figure 2.4 we show an example of the convergence of M during the intensification process for one of our numerical calculations (experiment at latitude 20°N and with an SST of 28°C). Panel (a) of this figure shows height-radius cross sections of the M-surfaces in the initial idealized vortex. There is a positive radial gradient of M throughout the entire domain depth. When air parcels move towards the vortex centre, they bring inwards larger values of M from the outer regions of circulation. Figure 2.4b shows the M surfaces 72 h later. During this time the M-surfaces have moved inwards throughout much of the lower and part of the middle troposphere (i.e., in the layer below 10 - 12 km), resulting in a local increase of M in these regions. Above a height of about

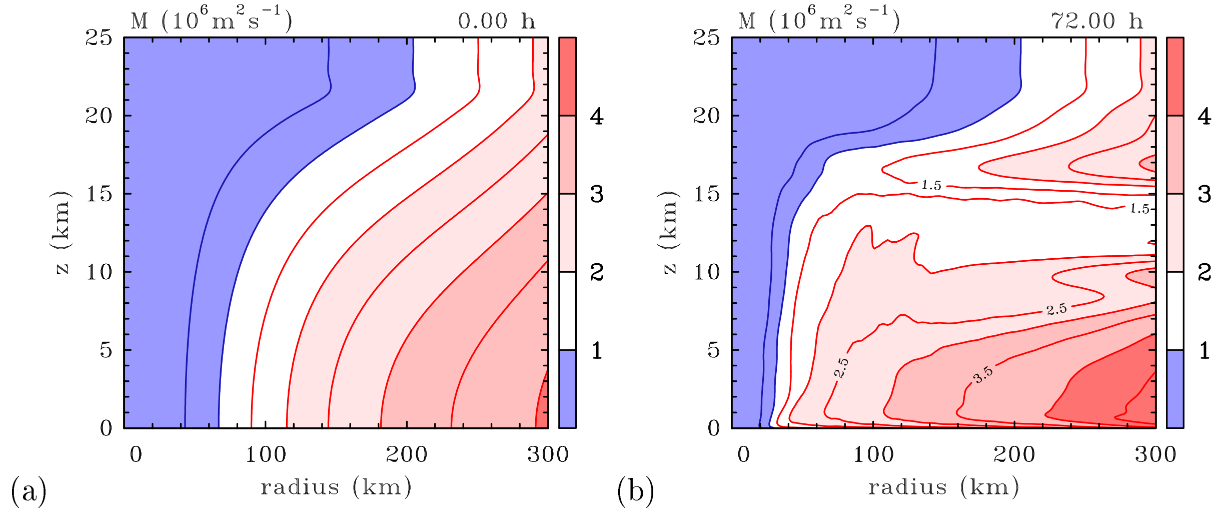

Figure 2.4: Height-radius cross sections of absolute angular momentum in the CM1 simulation at latitude 20°N with an SST of 28°C at (a) 0 h and (b) 72 h, supporting the radial convergence of M during the intensification process. Contour interval is 0.5 x 10^6 m^2 s^{-1}.

12 km, an approximately 5 km thick layer with reduced M has developed on account of upper-level outflow. Furthermore, at 72 h, the M surfaces in the lowest 1 km slope inwards with height, indicating the reduction of M in the boundary layer due to friction. However, despite this loss of M near the surface, the values of M have locally (i.e., at a given fixed radius) increased over the 72 h simulation time also within the boundary layer. For example, at the surface at a radius of 100 km from the vortex centre, the initial value of M is approximately 1.75 x 10^6 m^2 s^{-1}. After 72 h, the M value at this location has increased to approximately 2.5 x 10^6 m^2 s^{-1}. The local increase of M implies an increase in tangential wind in the boundary layer, because at a given radius on an f-plane, all other parameters in the expression for M (Eq. 2.20) are constant.

In summary, the results of the numerical simulation show the inward movement of the M-surfaces above the boundary layer as well as in the boundary layer, confirming the existence of both - conventional and boundary layer spin up mechanisms.

2.3 Limitations of axisymmetric theories and the new paradigm for intensification

The theory for tropical cyclone intensification presented in the above sections is based on axisymmetric perspective, although the intensification process is far from axisymmetric, at least in the early stages. The development of flow asymmetries is evident in all three-dimensional simulations of tropical cyclones, even in the prototype intensification problem on an f-plane (Montgomery and Smith 2014). Furthermore, the flow asymmetries develop in minimal models (for example, in a minimal three-layer model used in papers by Zhu and Smith 2002, 2003), as well as in sophisticated numerical models and are thus not a manifestation of a coarse resolution or some other model aspect. The emerging flow asymmetries are a reflection of a key physical process, namely moist convective instability (Montgomery and Smith 2014).

The asymmetric features found in the numerical simulations dominate the fields of vertical velocity, vertical component of relative vorticity (ζ) and diabatic heating rate. Despite initializing the model simulation with an axisymmetric vortex, the vertical velocity and relative vorticity fields at the beginning of the intensification phase, when the deep convective updraughts form, are no longer axisymmetric. Several patches of vertical velocity and ζ emerge in the inner-core region of the vortex. These cyclonically-rotating updraughts are sometimes referred to as *vortical hot towers* (VHTs). Typically, there is a relatively high number of VHTs at the beginning of the intensification (i.e., 10 - 20 or even more; their number depends primarily on the horizontal resolution of the model and moisture amount). During the period of rapid intensification, an upscale growth of the VHTs occurs. Their number decreases as they consolidate, but they grow horizontally in scale (Montgomery and Smith 2014). By the end of the rapid intensification period, no more than a few VHTs are active around the vortex centre (i.e., typically 3 to 5, but this number is again resolution and model dependent). Their structure remains spatially irregular. Nevertheless, the degree of vortex asymmetry at the end of intensification phase is usually reduced, since the aggregation process is typically accompanied with axisymmetrization (Montgomery and Smith 2014).

The nonaxisymmetric features dominating the early stages of the intensification process have been documented also in recent observations of tropical cyclones. Multiple evidence for the existence of VHT-like structures was found in the observations of genesis and intensification of the following storms: Hurricane Dolly (1996), Tropical Storm Alison (2001), Hurricane Ohpelia (2005), Typhoon Hagupit (2014), Typhoon Nuri (2014). The observational evidence for VHTs is summarized in Montgomery and Smith 2014 (see their section 6.2).

The existence of VHTs in numerical models as well as in observations raises the following question: To what extent can axisymmetric theories explain spin up in the three-dimensional model? In particular, can the axisymmetric theory be applied to the azimuthally-averaged fields from the three-dimensional model?

Hendricks *et al.* (2004) and Montgomery *et al.* (2006) addressed this question in the following way. They extracted the azimuthal averages of diabatic heating and azimuthal momentum sources at selected times from their three-dimensional model. Then they solved the Sawyer-Eliassen equation with these forcing terms. To investigate the extent to which the evolution of the azimuthally-averaged fields in three-dimensional models can be understood in terms of axisymmetric theory, they compared the azimuthal-mean radial and vertical velocity fields from the numerical model with those derived from the balanced streamfunction. As stated by Montgomery and Smith (2014): “Hendricks *et al.* and Montgomery *et al.* found good agreement between the two measures of the azimuthal-mean secondary circulation and concluded that the vortex evolution proceeded in a broad sense as a balanced response to the azimuthal-mean forcing by the VHTs."

Thus the axisymmetric theory still provides an acceptable basic framework for understanding the tropical cyclone intensification problem. However, it is necessary to develop an improved theory that would consider also the coherent asymmetric vortex structures controlling the intensification process. This is done in the new rotating-convective updraught paradigm for tropical cyclone intensification. The new paradigm is three-dimensional, as it recognizes the presence of localized, buoyant, rotating deep convection, which greatly amplifies the local vorticity. As in the axisymmetric theory, this convection collectively draws air parcels inwards towards the storm centre and, in an azimuthally-averaged sense, draws in surfaces of constant absolute angular momentum in the lower troposphere. For an extensive description of the new paradigm see Montgomery and Smith (2014).

2.4 Prototype problem for tropical cyclone intensification

The numerical experiments presented in this study are based on the typical thought experiment for tropical cyclone intensification, which is schematically shown in Figure 2.5. This thought experiment relates to the prototype problem for tropical cyclone intensification, which examines the evolution of a prescribed, initially cloud free, axisymmetric, baroclinic vortex in a quiescent environment. The vortex is placed over a warm ocean with a constant sea surface temperature. An f-plane is assumed. A mean environmental sounding of temperature and moisture is specified and used as a background state.

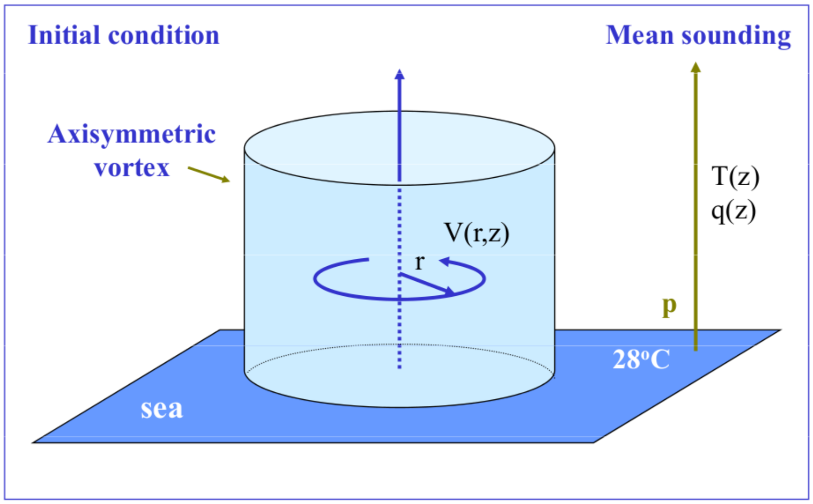

Figure 2.5: Schematic illustrating a basic thought experiment for tropical cyclone intensification. Courtesy R. K. Smith.

Chapter 3

Numerical model

The numerical model used for the study is the Bryan Cloud Model (CM1; Bryan and Fritsch 2002), version 16. It is a three-dimensional, nonhydrostatic, nonlinear, time-dependent numerical model designed for idealized studies of atmospheric phenomena. The model has been developed mainly by George Bryan at The Pennsylvania State University and at the National Center for Atmospheric Research (NCAR). It was designed primarily for idealized research, particularly for deep precipitating convection (i.e., thunderstorms). However, it has been significantly improved over the recent years and can nowadays be used to investigate a broad range of problems that span many scales. The model is freely available on the web.[1]

The governing equations of CM1 are presented in section 3.1. The description of the model configuration as used in this study is presented in section 3.2.

3.1 The governing equations

The model integrates the governing equations for the three components of the velocity vector, mixing ratio of moisture variables, perturbation Exner function, and perturbation density potential temperature, where perturbation quantities are defined relative to a prescribed hydrostatic basic state. The predicted variables of CM1 are listed in Table 3.1.

The model has the ability to use the traditional equation set that does not conserve energy and total mass in a moist atmosphere. This nonconservative set of equations has traditionally been used in many compressible nonhydrostatic models, such as Advanced Regional Prediction System (ARPS), Pennsylvania State University/National Center for Atmospheric Research Mesoscale Model (MM5) and Klemp-Wilhelmson Model. In addition, the model can be executed using the option that yields the mass- and energy-conserving equations of Bryan and Fritsch (2002) as is done in the present study.

The complete set of equations, including the momentum equation, thermodynamic equation, pressure equation, the equation for the moisture variables and the equation of state as used in this study is presented below.

---

[1] http://www2.mmm.ucar.edu/people/bryan/cm1/

Table 3.1: Predicted variables in the CM1 model.

Symbol	**Description**
u	velocity in x direction
v	velocity in y direction
w	velocity in z direction
π'	perturbation Exner function
θ'	perturbation potential temperature
q_ν	mixing ratio of moisture variables (for $\nu = v, l, i$):
	q_v - water vapour mixing ratio
	q_l - mixing ratio of liquid water
	q_i - mixing ratio of solid water (ice)

Momentum equation

The three components of the momentum equation are expressed as:

$$\frac{du}{dt} + c_p\theta_\rho\frac{\partial\pi'}{\partial x} - fv = T_u + D_u + N_u \tag{3.1}$$

$$\frac{dv}{dt} + c_p\theta_\rho\frac{\partial\pi'}{\partial y} + fu = T_v + D_v + N_v \tag{3.2}$$

$$\frac{dw}{dt} + c_p\theta_\rho\frac{\partial\pi'}{\partial z} - B = T_w + D_w + N_w \tag{3.3}$$

where c_p is the specific heat of dry air at constant pressure, θ_ρ is the density potential temperature, f is the Coriolis parameter and B is the buoyancy. T terms represent tendencies from subgrid turbulence, D terms represent optional tendencies from other diffusive processes and N terms represent Newtonian relaxation (i.e., Rayleigh damping).

The density potential temperature is expressed as:

$$\theta_\rho = \theta\left(\frac{1+\frac{q_v}{\epsilon}}{1+q_t}\right), \tag{3.4}$$

where θ is the potential temperature of dry air, ϵ is the ratio between specific heat of dry air and specific heat of water vapour, and q_t is the total water mixing ratio: $q_t = q_v + q_l + q_i$.

Buoyancy is defined as:

$$B = g\frac{\theta_\rho - \theta_{\rho 0}}{\theta_{\rho 0}}. \tag{3.5}$$

Herein, a subscript 0 denotes the base-state variable, which is by definition invariant in time and is a function of z only.

The tendencies from the subgrid turbulence are formulated as follows:

$$T_i = \frac{1}{\rho}\sum_{j=1}^{3}\frac{\partial(\rho\tau_{ij})}{\partial x_j}, \tag{3.6}$$

where ρ is the dry air density and τ_{ij} are the subgrid stress terms defined as: $\tau_{ij} \equiv \overline{u_i' u_j'}$.

Thermodynamic equation

The potential temperature of dry air is defined as:

$$\theta = \frac{T}{\pi}. \tag{3.7}$$

The first law of thermodynamics is formulated as:

$$\begin{aligned}\frac{d\theta'}{dt} =& -\theta\Big(\frac{R_m}{c_{vm}} - \frac{R}{c_p}\frac{c_{pm}}{c_{vm}}\Big)\Big(\frac{\partial u}{\partial x} + \frac{\partial v}{\partial y} + \frac{\partial w}{\partial z}\Big) + T_\theta + D_\theta + \dot{Q}_\theta \\ &+ N_\theta\frac{c_v}{c_{vm}c_p\pi}\Big(L_v\dot{q}_{cond} + L_s\dot{q}_{dep} + L_f\dot{q}_{frz}\Big) - \theta\frac{R_v}{c_{vm}}\Big(1 - \frac{R}{c_p}\frac{c_{pm}}{R_m}\Big)\Big(\dot{q}_{cond} + \dot{q}_{dep}\Big),\end{aligned} \tag{3.8}$$

where R, R_v and R_m are the gas constants of dry air, water vapour and moist air, respectively. Constants c_p and c_v are specific heat of dry air at constant pressure and volume, respectively. Similarly, c_{pm} and c_{vm} represent the specific heat of moist air at constant pressure and volume, respectively. The $\dot{q}$ terms represent phase changes between the three moisture components q_v, q_l and q_i (i.e., $\dot{q}_{cond}$ for condensation, $\dot{q}_{dep}$ for deposition and $\dot{q}_{frz}$ for freezing). L_v, L_s and L_f are the latent heat coefficients for vaporization, sublimation and freezing, respectively. The term $\dot{Q}_\theta$ captures radiative heating and/or cooling, all other tendency terms are as defined above.

Pressure equation

The non-dimensional pressure or the Exner function is defined as:

$$\pi = \Big(\frac{p}{p_0}\Big)^{\frac{R}{c_p}}. \tag{3.9}$$

The prognostic equation for the perturbation Exner function has the following form:

$$\begin{aligned}\frac{d\pi'}{dt} - \frac{g}{c_p\theta_{\rho 0}}w =& \frac{R}{c_v}\frac{\pi}{\theta}\Big(T_\theta + D_\theta + N_\theta + \dot{Q}_\theta\Big) + \frac{R}{c_v}\frac{\pi}{(\epsilon + q_v)}\Big(T_{qv} + D_{qv}\Big) \\ &- \frac{R}{c_p}\frac{c_{pm}}{c_{vm}}\pi\Big\{\Big(\frac{\partial u}{\partial x} + \frac{\partial v}{\partial y} + \frac{\partial w}{\partial z}\Big) - \frac{1}{c_{pm}\theta\pi}\Big(L_v\dot{q}_{cond} + L_s\dot{q}_{frz}\Big) + \frac{R_v}{R_m}(\dot{q}_{cond} + \dot{q}_{dep})\Big\}.\end{aligned} \tag{3.10}$$

Equation for the moisture variables

Conservation laws for water vapour, liquid water and solid water (ice) are expressed by the equations (3.11), (3.12) and (3.13), respectively:

$$\frac{dq_v}{dt} = T_{qv} + D_{qv} - \dot{q}_{cond} - \dot{q}_{dep}, \tag{3.11}$$

$$\frac{dq_l}{dt} = T_{ql} + D_{ql} + \dot{q}_{cond} - \dot{q}_{frz} + \frac{1}{\rho}\frac{\partial(\rho V_l q_l)}{\partial z}, \tag{3.12}$$

$$\frac{dq_i}{dt} = T_{qi} + D_{qi} + \dot{q}_{dep} + \dot{q}_{frz} + \frac{1}{\rho}\frac{\partial(\rho V_i q_i)}{\partial z}, \tag{3.13}$$

where V is the terminal fall velocity of hydrometeors. Specifically, V_l is the terminal fall velocity of liquid water and V_i that of ice.

Equation of state

Variables must also obey the equation of state, which has the following form:

$$p = \rho R T (1 + \frac{q_v}{\epsilon}). \tag{3.14}$$

A more detailed description of the governing equations and the variable definitions can be found in the technical document *The governing equations for CM1* (Bryan 2014).

3.2 Model configuration

The CM1 model can be used in a variety of configurations for different applications. A special feature of the model is that it can be run in axisymmetric as well as in a three-dimensional configuration. Furthermore, the model can be executed using the compressible equations, but it can also be used with the anelastic equations, and even incompressible equations. The model equations are discretized on the Arakawa C-grid (Arakawa and Lamb 1977), which is schematically shown in Figure 3.1. In this framework the momentum points are staggered half a grid spacing from the locations of scalar variables (i.e., θ, π, q_v, etc.). CM1 uses terrain-following coordinates and can therefore be used with terrain also. Over the sea, as is the case in our study, the terrain-following coordinates simplify to regular Cartesian coordinates. Moreover, CM1 can be used with stretched grids in all three coordinates. An analytic stretching function (Wilhelmson and Chen 1982) is used to create smoothly varying grid spacing. CM1 contains several different explicit moisture schemes for resolving clouds and precipitation. It contains also several different advection, diffusion and subgrid turbulence schemes, and various options for base-state sounding and initialization. These and many other available settings provide that CM1 can be applied to

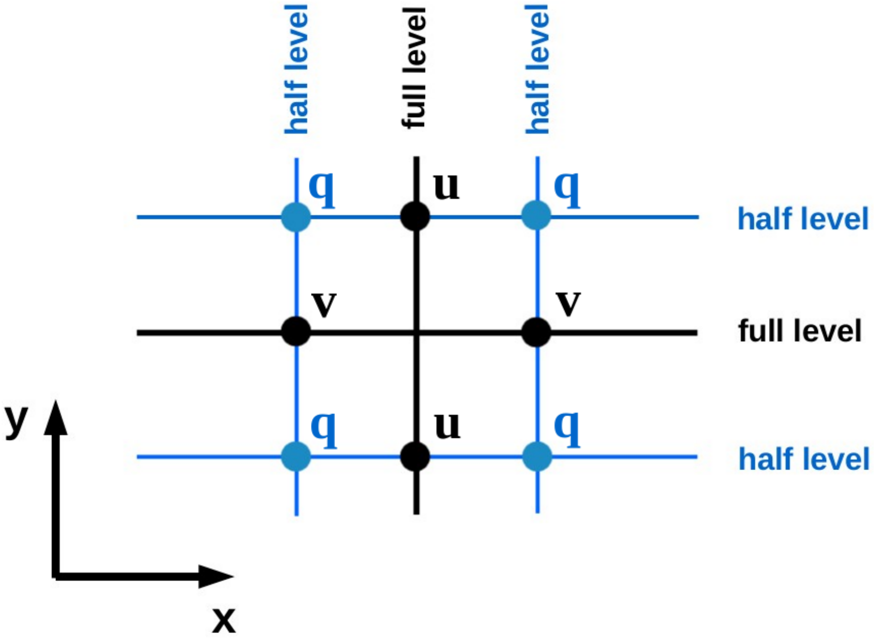

Figure 3.1: Horizontal view of Arakawa C grid. The u- and v-momentum points are located on full model levels. The scalar variables (denoted here with q) are calculated on half levels, that are staggered half a grid spacing from the position of full levels. Vertical view of this grid is qualitatively similar, with the w-momentum points being located half a grid spacing apart from the scalar grid points.

a variety of problems for investigation of different phenomena. In the following paragraphs the model setup as used in this study is summarized.

The experiments are carried out using the three-dimensional model configuration, assuming a compressible atmosphere. The domain is 3005 × 3005 km in size with 570 grid points in each horizontal direction. The inner part of the domain has the dimensions 600 × 600 km with a constant grid spacing of 3 km. Beyond the inner 600 km, the horizontal grid is gradually stretched to a spacing of 10 km at the outer edges in horizontal directions. A schematic of the stretched grid in the horizontal direction is shown in Figure 3.2. The domain has 40 vertical levels extending to a height of 25 km. The vertical grid spacing expands gradually from 50 m near the surface to 1200 m at the top of the domain, as is shown in Figure 3.3. There are nine vertical levels within the lowest 1.5 km. The vertical resolution in the boundary layer is therefore believed to be adequate for proper representation of boundary layer dynamics.

To suppress the artificial reflection of internal gravity waves from the upper boundary, a Rayleigh damping layer is added at heights above 20 km. The e-folding time scale for this damping is 5 min. Rayleigh damping is applied also within 100 km of the lateral boundaries, which are rigid walls.

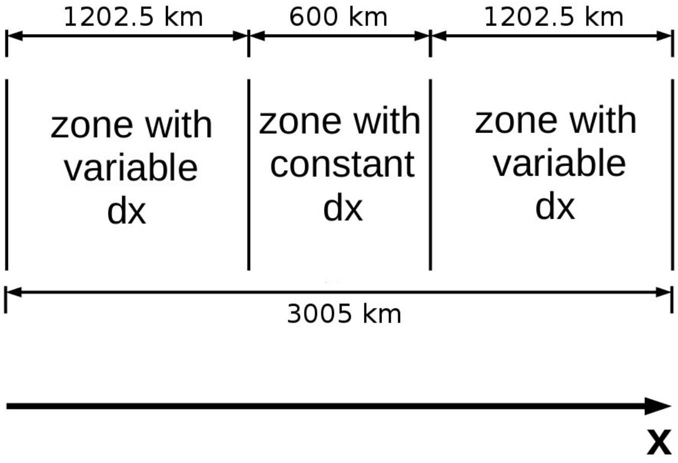
1202.5 km
600 km
1202.5 km
zone with variable dx
zone with constant dx
zone with variable dx
3005 km
X

Figure 3.2: Schematic of the stretched grid in the horizontal x direction. In CM1 the middle of the domain has no stretching. This no-stretching zone is flanked on both sides by equal-length stretching zones. The dimensions labelled on the schematic are used in this study. The configuration in y direction is equivalent.

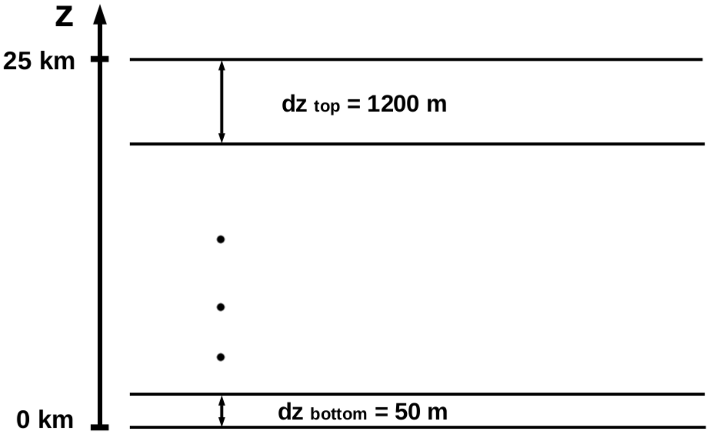
Z
25 km
dz top = 1200 m
dz bottom = 50 m
0 km

Figure 3.3: Schematic of the stretched grid in the vertical z direction as used in the present study. The stretching layer extends throughout the entire domain depth with the vertical grid spacing increasing gradually from 50 m near the surface to 1200 m at the domain top.

The simple Rotunno-Emanuel (1987) water-only scheme with a 7 m s^{-1} terminal fall velocity of rain is used as a warm-rain convection scheme. For simplicity, ice microphysical processes and dissipative heating are not included. Radiative effects are represented by adopting a simple Newtonian cooling approximation with a time scale of 12 h. Following Rotunno and Emanuel (1987), the magnitude of the cooling rate is capped at 2 K per day.

In our experiments fifth-order horizontal and vertical advection schemes are being used. Technically, the advantage of the fifth-order advection scheme over the sixth-order advection scheme, which is also one of the options available in the model, is that it does not require any artificial diffusion for stability.

There is a representation of subgrid-scale turbulence in the model. It is assumed that no turbulent eddies are resolved on the grid, and hence their affects must be accounted completely via the T terms introduced in section 4.1. The parameterized turbulence scheme follows the formulation of Blackadar (1962). Here the horizontal mixing length l_h is taken to be constant, while the vertical length scale l_v is a function of height and approaches zero near the surface. In our experiments, the horizontal turbulence length scale is set to be 700 m, while the asymptotic vertical turbulence length scale l_{inf} (i.e., vertical length scale at z = infinity) is set equal to 50 m.

The parameters determining the exchange of heat and momentum between the ocean and the atmosphere are set as follows. The surface exchange coefficient for enthalpy C_e is set to a constant value of 1.29 x 10^{-3}, based on the results from the Coupled Boundary Layer Air-Sea Transfer (CBLAST) experiment. The surface exchange coefficient for momentum (i.e., surface drag coefficient) C_d is also taken to be constant and set to 2.58 x 10^{-3}, which is twice the C_e value. This is again in agreement with the estimated value of C_d from CBLAST observations.

The background thermodynamic state is based on the Dunion moist tropical sounding (Dunion 2011), shown in Figure 3.4. The prescribed initial vortex is axisymmetric and in thermal wind balance. It is placed in the centre of the domain. The initial tangential wind speed has a maximum of 15 m s^{-1} at the surface and at a radius of 100 km from the centre of circulation. It decreases sinusoidally with height, becoming zero at a height of 20 km. The balanced pressure, density and temperature fields consistent with this prescribed tangential wind distribution are obtained using the method described by Smith (2006). A more detailed description of this method is presented in the next chapter, together with technical issues that arose during its implementation in the model.

All in all we perform nine numerical simulations taking combinations of three different latitudes (10°N, 20°N, 30°N) and three different sea surface temperatures (26°C, 28°C, 30°C), as schematically shown in Figure 3.5. The calculations are carried out on an f-plane. Although the model has an option to use an ocean mixed layer model, for simplicity the sea-surface temperature is held fixed in all nine experiments. Our interest is focussed on the initial period of vortex intensification whereupon the calculations are carried out for a period of 3 days with data output every 15 min.

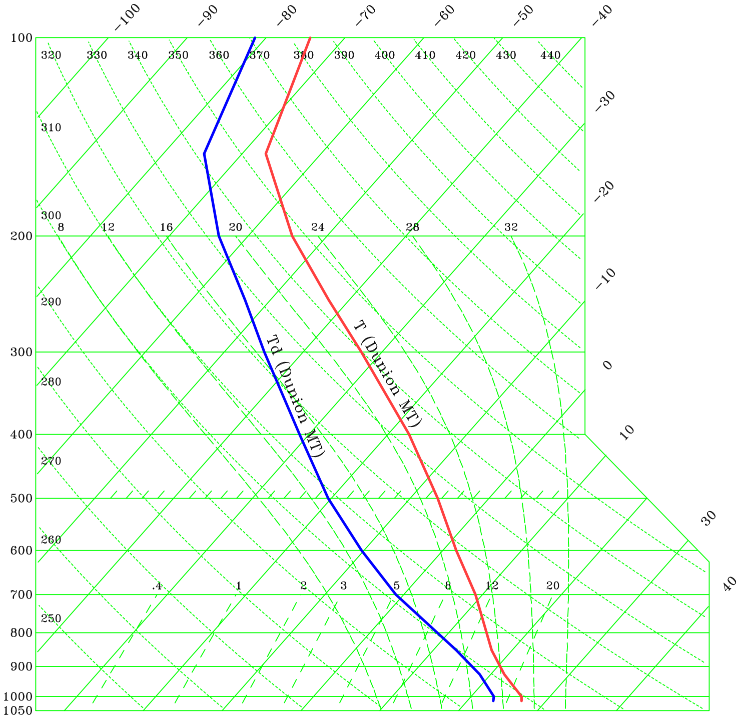

Figure 3.4: Skew-*T* log-*p* diagram of the Dunion moist tropical (MT) thermodynamic sounding used as a background state in the numerical experiments carried out in this study. Red curve shows the vertical profile of temperature, while blue curve shows the dew-point temperature profile.

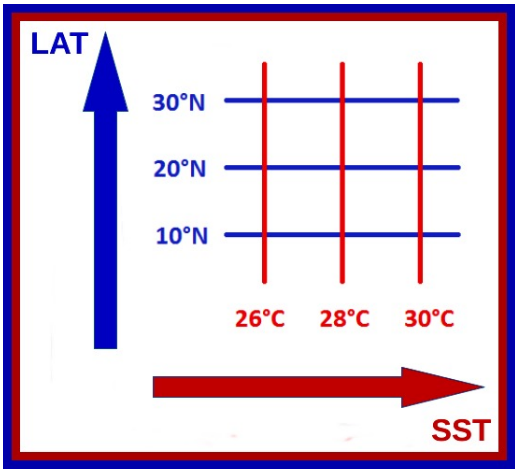

Figure 3.5: Matrix depicting the nine numerical experiments carried out in this study, being combinations of one of three different latitudes (10°N, 20°N, 30°N) with one of three different sea surface temperatures (26°C, 28°C, 30°C).

Chapter 4

Initialization problem: Implementation of a balanced axisymmetric vortex into CM1 model

4.1 Motivation

There are several initialization options available in the CM1 model (i.e., warm bubble, cold pool, forced convergence, etc.), but only one of these initializes a tropical-cyclone-like vortex. This option is based on the vortex used by Rotunno and Emanuel (1987) and has the disadvantage that the vortex wind profile is a function of latitude (Fig. 4.1). This feature makes it unsuitable for the present study where it is desirable to initialize the same vortex at different latitudes. For this reason we implemented a new 3D initialization option into CM1 model - an idealized axisymmetric balanced vortex with a prescribed tangential wind field distribution that is independent of latitude.

4.2 Determination of a balanced axisymmetric vortex

We present a simple method to calculate a tropical-cyclone-like vortex, which is axisymmetric and in thermal wind balance. The problem is to determine the balanced pressure, density and temperature fields consistent with a prescribed initial tangential wind distribution and a prescribed ambient thermodynamic profile at some large radius from the vortex centre. The method is extensively described by Smith (2006), where the author solves the thermal wind equation in various coordinate systems. In this section we review the basic steps of this method in height-radius coordinates (r, z). We recall the unapproximated form of the thermal wind equation that has already been derived in Chapter 2:

$$\frac{\partial}{\partial r}\ln\rho + \frac{C}{g}\frac{\partial}{\partial z}\ln\rho = -\frac{1}{g}\frac{\partial C}{\partial z}, \tag{4.1}$$

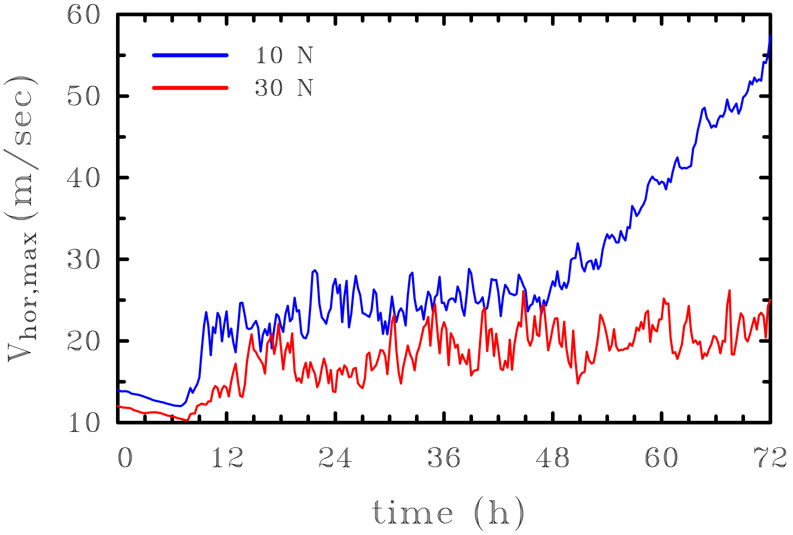

Figure 4.1: Time series of the maximum total horizontal wind speed in the CM1 experiments initialized with the Rotunno-Emanuel tropical cyclone at latitudes 10°N and 30°N. Note the different initial intensities of the two vortices. The maximum initial wind speed at 10°N is 14,0 m s^{-1}, while at 30°N it is 12,0 m s^{-1}.

wherein the term C is defined as the sum of the centrifugal and Coriolis forces per unit mass:

$$C = \frac{v^2}{r} + fv. \tag{4.2}$$

It should be borne in mind that the prescribed tangential wind speed distribution is a function of both radius and height, $v(r, z)$, and therefore also $C = C(r, z)$. The thermal wind equation (Eq. 4.1) is a first-order partial differential equation (PDE), which can be solved with the method of characteristics. In general, the method of characteristics is a technique for solving partial differential equations by reducing them to a family of ordinary differential equations (ODE). In the case of Eq. (4.1), the characteristics, $z(r)$, are solutions of the following ODE:

$$\frac{dz}{dr} = \frac{C}{g}. \tag{4.3}$$

It can be easily shown that these characteristics are the isobaric surfaces (see Smith, 2006). Eq. (4.1) then becomes:

$$\frac{d}{dr} \ln \rho = -\frac{1}{g}\frac{\partial C}{\partial z}, \tag{4.4}$$

and determines the variation of density along the characteristics. Equations (4.3) and (4.4) provide a suitable way to tackle the problem of initializing tropical cyclones in numerical models, where typically one has to specify the vortex at a set of grid points. Consider an arbitrary grid point P with coordinates (r_p, z_p) as illustrated in Figure 4.2. We can integrate the equation (4.3) radially outwards to some large radius R, where the ambient vertical profile is known, to find the height of the isobaric surface through the observed grid point P, z_R, at this radius. In this way we have determined the pressure at point P, because we know the pressure at point (R, z_R) and it is constant along the characteristics. Similarly, by integrating the equation (4.4) radially outwards to radius R along the characteristics we obtain the change in $ln\rho$ between the point P and the point (R, z_R). Because the density at radius R is also known, we can immediately determine ρ at the point P. Knowing both p and ρ at the point P we can finally calculate the temperature at this point using the ideal gas equation. The foregoing calculation is repeated for every grid point in the domain to determine the balanced pressure, density and temperature fields throughout the entire height-radius plane.

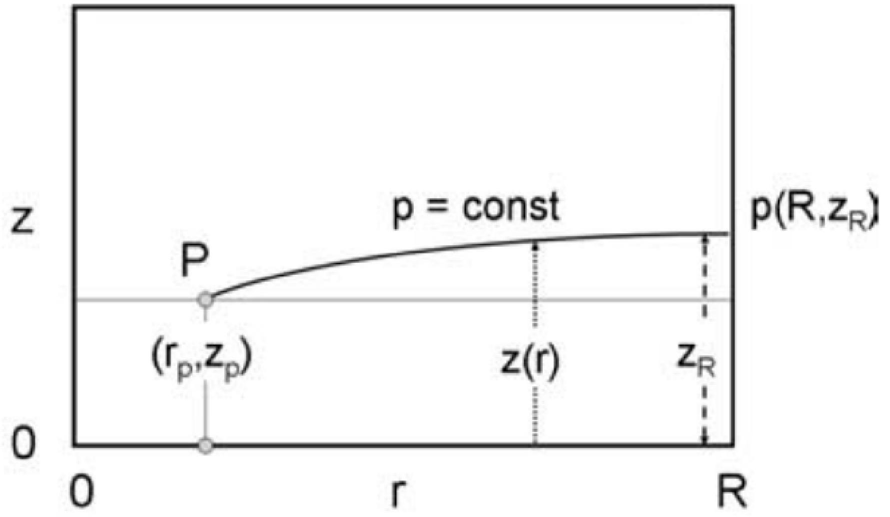

Figure 4.2: Illustration related to the calculation of the balanced fields at an arbitrary grid point P with coordinates $(r_P,\ z_P)$, based on the method of characteristics. The curved line indicates an isobaric surface through point P. We can integrate the equation (4.3) to find the height of this isobaric surface at $r = R$, where the vertical thermodynamic profile is known. Courtesy R. K. Smith.

4.3 Implementation in the CM1 model

A few technical issues arose when implementing the balance code into the CM1 model. The method described by Smith (2006) was originally applied to the determination of a balanced axisymmetric vortex in a dry atmosphere. When carrying out the numerical experiments in a moist atmosphere, as is done in the present study, one needs to decide how to incorporate moisture initially. We assumed that the initial moisture is constant

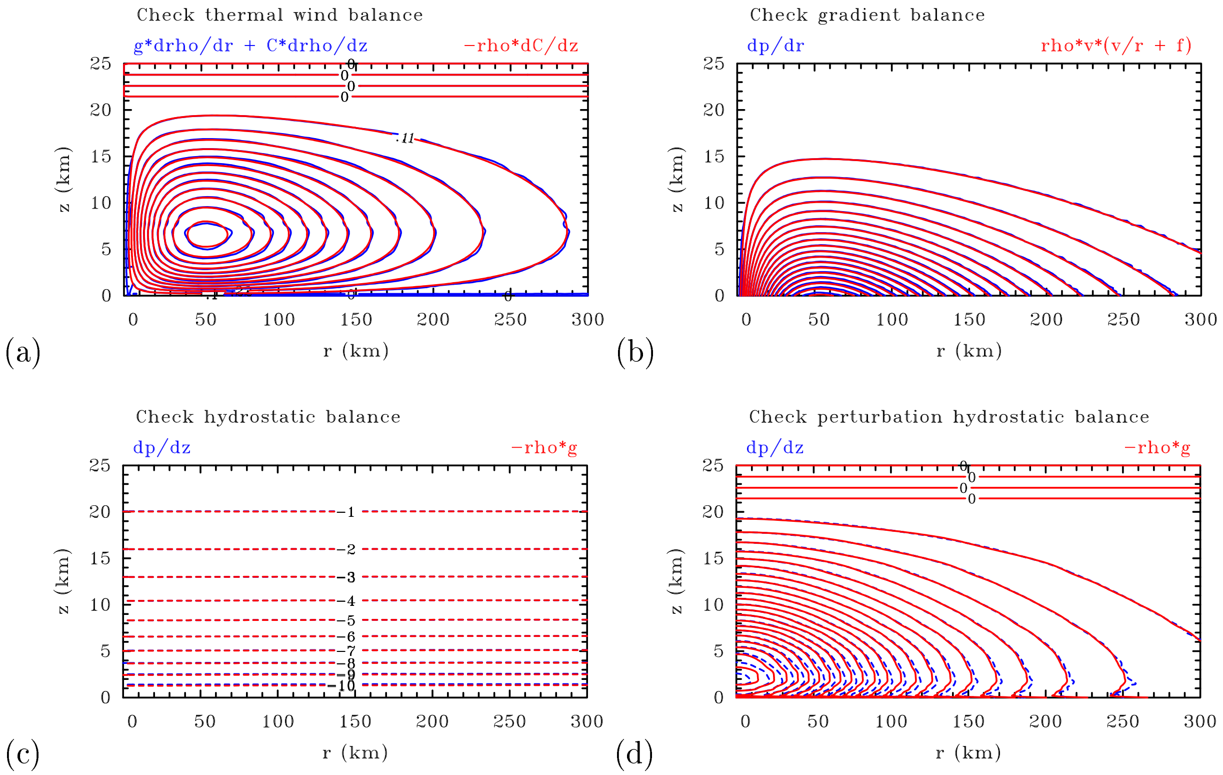

Figure 4.3: Balance checks for the vortex at latitude 10°N. (a) Check of thermal wind balance; (b) Check of gradient wind balance; (c) Check of hydrostatic balance; (d) Check of perturbation hydrostatic balance. Left-hand sides of the corresponding balance equations are plotted blue, while the right-hand sides of the equations are plotted red. The blue curves are hardly visible, because they are covered with red curves, which means that the balance equations are satisfied with a high level of accuracy. Similar balanced results were obtained also for the vortices at latitudes 20°N and 30°N.

along height levels[1] and solved the thermal wind equation in a qualitatively similar way as described in section 4.2, except that the virtual temperature has been used in the equation of state instead of the dry air temperature.

Moreover, the vertical grid in the CM1 model is stretched, therefore some additional interpolation was required in the vertical direction. Furthermore, the balanced fields obtained by the method of characteristics are defined in a height-radius plane, whereas the 3D configuration of the CM1 model requires an initialization of the 3D arrays. Because the stretching of the model levels is applied in the horizontal directions also, the recalculation of the 2D arrays into 3D arrays required some additional interpolation as well.

Due to technical issues discussed above, it is reasonable to ask whether the implemented

---

[1] An alternative option would be to assume that the initial moisture content is constant along the isobaric surfaces.

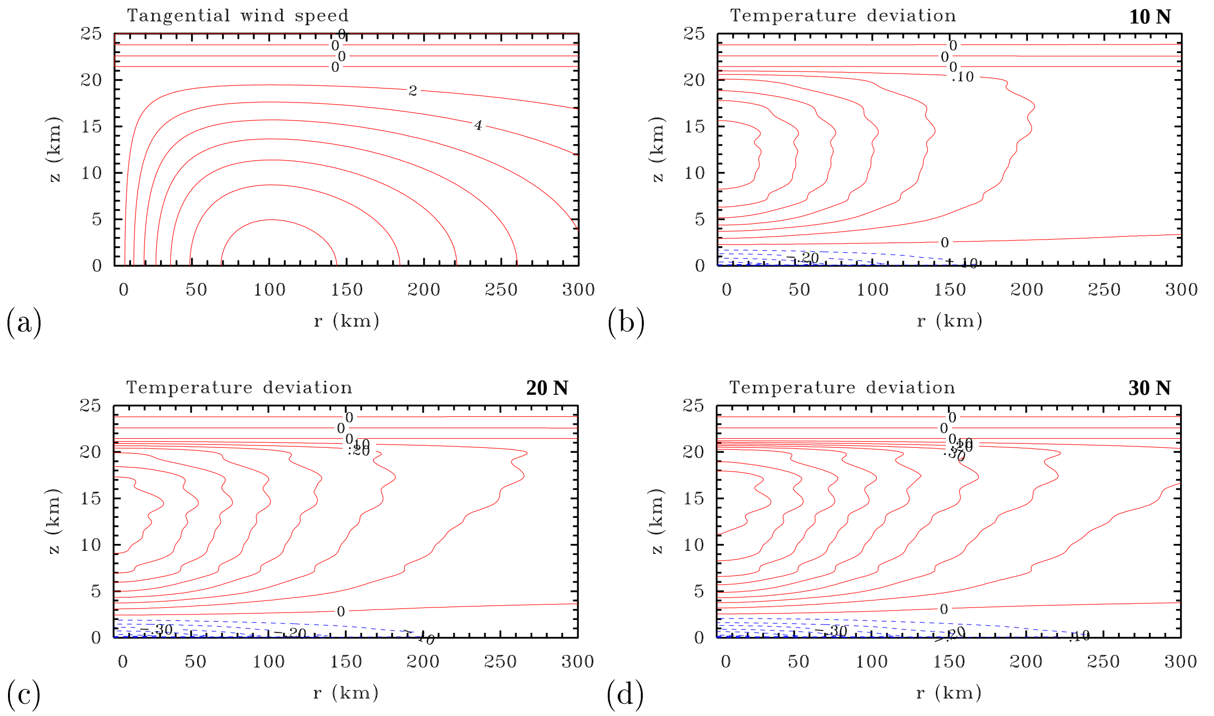

Figure 4.4: Height-radius cross sections of: (a) tangential wind speed in the idealized warm-cored vortex used as the initial state in the CM1 simulations (contour interval: 2 m s^{-1}) and the corresponding balanced temperature perturbations at latitudes (b) 10°N, (c) 20°N and (d) 30°N. Contour interval in (b), (c) and (d) is 0.1°C, positive contours are solid red, negative contours are dashed blue.

vortex is still in balance after it has been subjected to several interpolation steps, which are always a source of numerical errors. In Figure 4.3 we show the balance checks for the vortex at 10°N, confirming that the implemented vortex is in thermal wind balance with a very high accuracy. In summary, the idealized axisymmetric vortex has been successfully implemented in the CM1 model and can be used from now on as an initial state in both axisymmetric and three-dimensional model configurations.

At this stage one additional remark should be pointed out. Our aim, as outlined in the beginning of this chapter, is carrying out the nine numerical experiments with the same initial state. Using the method presented in section 4.2 we are able to initialize the whole set of experiments with the vortices that have exactly the same initial wind speed distribution. Thus, the vortices possess the same initial intensity. However, because the thermal wind equation contains the Coriolis parameter, the vortices at different latitudes have different initial temperature and density distributions for the same initial wind profile. Figure 4.4a shows the height-radius cross section of the initial tangential wind speed distribution that has been used in all nine experiments. Panels (b) - (d) of this figure show the corresponding balanced temperature perturbations at the three latitudes used in this study. The temperature deviations are calculated as the differences between the total temperature and the base-state temperature. One can see that the magnitude and radial extent of the temperature deviation increase with increasing latitude. The maximum temperature deviation at 10°N, 20°N and 30°N amounts to approximately 0.6 K, 0.7 K and 0.8 K, respectively. The differences in the temperature field affect the degree of the initial stability of the vortices at various latitudes (i.e., reduced upper-level stability in the low-latitude vortex). In other words, the decreased breadth and magnitude of temperature anomaly with decreasing latitude would imply an increase in Convective Available Potential Energy (CAPE). This issue will be discussed in more detail in the next chapter.

Chapter 5

Dependence of tropical cyclone intensification on latitude

The numerical model used in this study is different from that used by Smith *et al.* (2015), namely version 16 of CM1: Smith *et al.* (2015) used a modified version of the Pennsylvania State University/National Center for Atmospheric Research Mesoscale Model (MM5). The most important differences between the two models are as follows. CM1 has more accurate numerics and a more accurate representation of moisture than MM5. Moreover, the new calculations using CM1 are performed with an increased horizontal resolution - the inner part of the domain with the dimensions 600 km × 600 km has a constant grid spacing of 3 km (this compares with a grid spacing of 5 km used by Smith *et al.* 2015). For these reasons we have sought here to reproduce and verify the results of Smith *et al.* (2015), before going on to investigate the dependence of intensification rate on sea surface temperature.

In the next section we present the key results of the CM1 simulations at three different latitudes (10°N, 20°N, 30°N) for an SST of 28°C. In the subsequent section we offer an explanation of the latitudinal dependence of tropical cyclone intensification, following the work of Smith *et al.* (2015). Ultimately, a summary of the main findings is given.

5.1 Model results

Figure 5.1a shows time series of the maximum azimuthally-averaged tangential wind speed (v_{max}) in the three CM1 calculations at different latitudes for an SST of 28°C. The horizontal lines at the bottom of the figure denote the period of rapid intensification, often abbreviated "RI", during which the intensification rate (IR) exceeds the threshold value of 15 m s^{-1} day^{-1}. Here, the IR at time t is calculated as the 24 hour change in maximum azimuthally-averaged tangential wind speed, i.e. $v_{max}(t+12\text{ h})-v_{max}(t-12\text{ h})$. [1] All three

---

[1] The calculation of IR based on the 24 hour difference in v_{max} is possible only between 12 and 60 h. Because of the delay in the onset of RI for the vortex at 30°N, the end of the RI is not captured within 60 h. The dashed black line in Figure 5.1(a) and in the right panels of Figure 5.2 for the vortex at 30°N denotes the presumed continuation of RI period after 60 h, following the equivalent calculation of IR based on the 6 hour change in v_{max} and multiplied by 4.

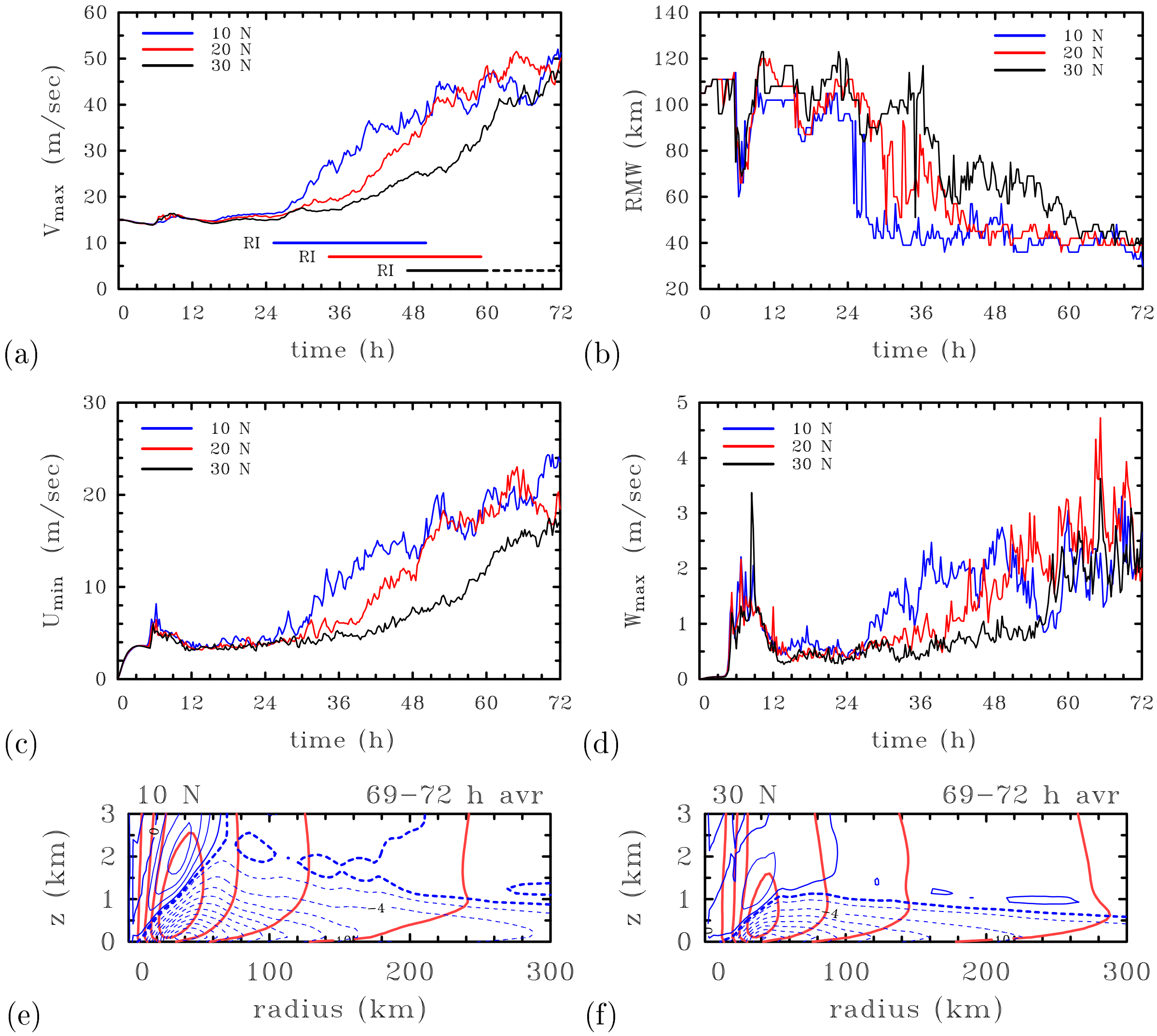

Figure 5.1: Time series of azimuthally-averaged quantities including: (a) the maximum tangential wind speed, (b) RMW, (c) maximum radial inflow, (d) maximum vertical velocity in the CM1 calculations at latitudes 10°N, 20°N and 30°N with an SST of 28°C. The horizontal lines in (a) denote the period of rapid intensification at each latitude. Panels (e) and (f) show height-radius cross sections of the azimuthally-averaged tangential (red contours) and radial wind (blue contours) in the lowest 3 km at 10°N and 30°N, respectively (contour interval: 10 m s^{-1} for the tangential wind, 2 m s^{-1} for the radial wind). Dashed curves indicate negative values. The thick dashed blue contour shows the -1 m s^{-1} contour of radial wind.

vortices undergo a period of rapid intensification, but the intensification begins earlier and is more rapid when the latitude is decreased. Specifically, the vortices at 10°N, 20°N and 30°N enter a rapid intensification phase at about 25, 35 and 47 hours after the beginning of simulation, respectively. The intensification rates of the vortices at 10°N and 20°N attain similar maximum values of almost 30 m s^{-1} day^{-1}, while the maximum IR for the vortex at 30°N is slightly lower. The final intensity of the vortices after 3 days does not differ much as they reach similar value of v_{max} of about 50 m s^{-1}. Typically, the maximum tangential wind speed occurs at a height of approximately 650 m in the second half of simulation. This value is only slightly dependent on latitude.

Panels (b)-(d) of Figure 5.1 show time series of radius of maximum azimuthally-averaged tangential wind speed (RMW), minimum azimuthally-averaged radial wind speed u_{min} (i.e., maximum radial inflow) and maximum azimuthally-averaged vertical velocity w_{max}, respectively. Consistent with the idea that the closer air parcels can approach the axis of rotation, the faster they can spin, the RMW decreases with latitude during the intensification (Fig. 5.1b). The largest contraction of the RMW occurs during the period of RI. The larger inward displacements of air parcels as the latitude is decreased is consistent with the increase in the maximum radial inflow (Fig. 5.1c). Typically, the maximum radial inflow occurs close to the ocean surface at a height of 90 m (i.e., at the second vertical model level) at all three latitudes. Finally, the maximum vertical velocity is largest for the vortex at 10°N and the lowest for the vortex at 30°N, at least during first 50 hours (Fig. 5.1d).

Panels (e) and (f) of Figure 5.1 show the height-radius cross sections of the azimuthally-averaged tangential and radial wind, time-averaged during the last three hours of the calculation (i.e., from 69 to 72 h), in the experiments at 10°N and 30°N. It can be seen that the boundary layer at 10°N is deeper and stronger than at 30°N. The maximum boundary layer inflow at 10°N amounts to approximately 23 m s^{-1}, compared with 16 m s^{-1} at 30°N. Another noteworthy feature is the steady increase of the boundary layer depth (as characterized, for example, by the depth of appreciable inflow indicated by the $-$ 1 m s^{-1} contour of the radial wind) with decreasing radius to approximately the radius of maximum tangential wind speed. The depth of the boundary layer at this radius exceeds 2 km in the 10°N calculation, while the maximum depth of the boundary layer at 30°N is only about 1 km.

The results described above are consistent with those of Smith *et al.* (2015).

5.2 Interpretation of the latitudinal dependence

In seeking an explanation for the dependence of tropical cyclone intensification on latitude, we discuss a range of physical processes that could explain the more rapid spin up of storms as the latitude is decreased, focusing on the two calculations at latitudes 10°N and 30°N.

5.2.1 Thermodynamic issues

Smith *et al.* (2015) showed that even if the tangential wind profile at the top of the boundary layer is held fixed, a simple, steady slab boundary layer model produces stronger low-level inflow as the latitude is decreased. An increase in near-surface wind at lower latitudes would imply an increase in evaporation from the ocean surface, at least if one assumes the unchanged thermodynamic disequilibrium between the ocean and the lowest

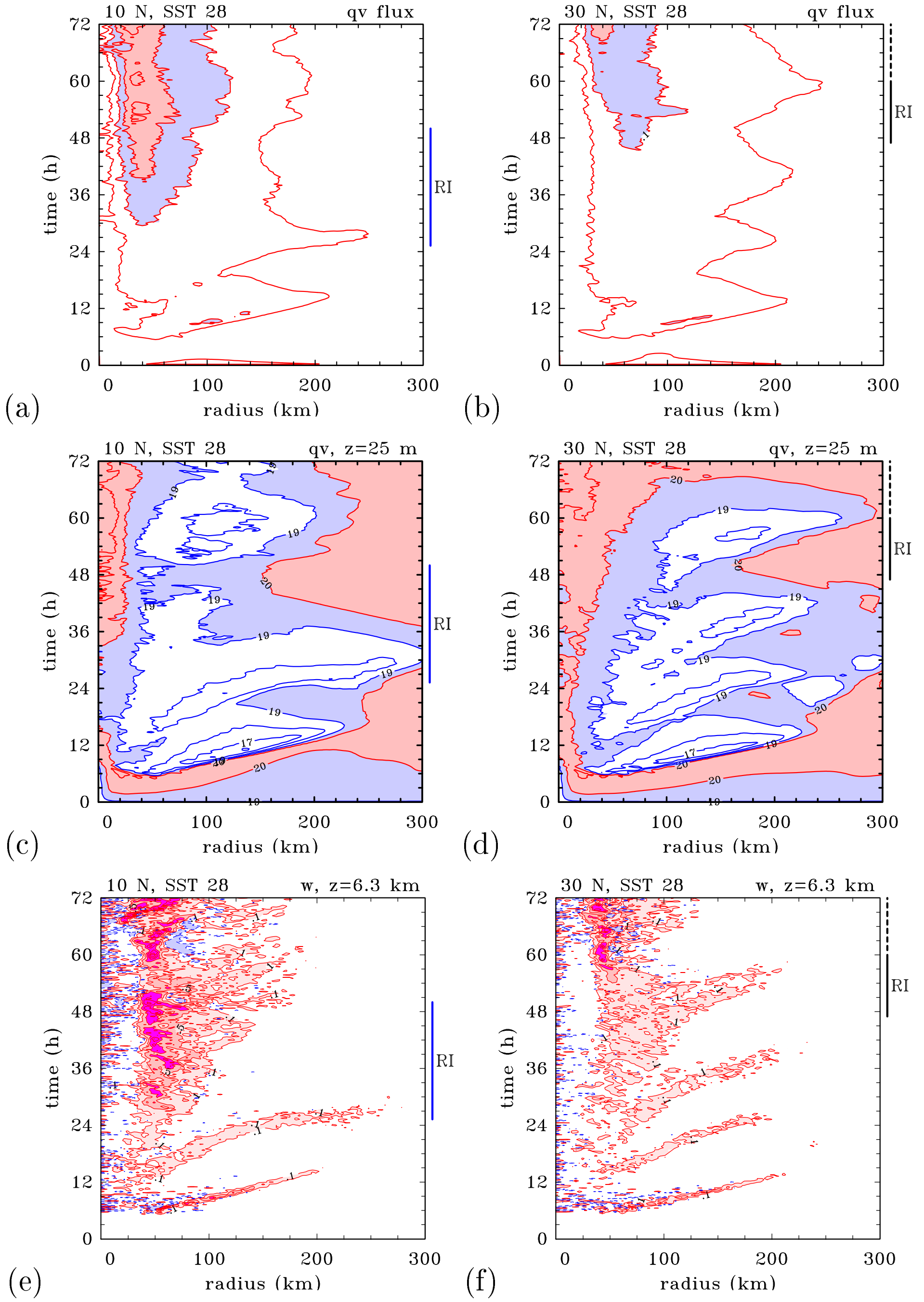

Figure 5.2: Time-radius plots of azimuthally-averaged surface water vapour fluxes (upper panels), water vapour mixing ratio at 25 m (middle panels) and vertical velocity at 6.3 km (bottom panels) in the CM1 calculations at latitudes 10°N (left) and 30°N (right) for an SST of 28°C. Contour interval in (a) and (b) is 0.05 g kg^{-1} s^{-1}, values between 0.10 and 0.15 g kg^{-1} s^{-1} are shaded blue and those $\geq$ 0.15 g kg^{-1} s^{-1} are shaded pink. Contour interval in (c) and (d) is 1 g kg^{-1}, values between 19.0 and 20 g kg^{-1} are shaded blue and those $\geq$ 20 g kg^{-1} are shaded pink. Shading in (e) and (f): Values between 0.1 and 0.5 m s^{-1} are shaded light pink, values between 0.5 and 1.0 m s^{-1} are shaded light red, values $\geq$ 1.0 m s^{-1} are shaded purple and those $\leq$ -0.1 m s^{-1} are shaded blue. The vertical line to the right of each panel shows the period of RI at the particular latitude (see Fig 5.1a).

layer of the atmosphere. This is a reasonable assumption because the saturation specific humidity increases with decreasing pressure. The Hovmöller diagrams of azimuthally-averaged surface enthalpy fluxes in the two calculations at 10°N and 30°N are shown in the upper panels of Figure 5.2. Confirming the expectations, the fluxes are higher at 10°N than at 30°N.

As shown by Smith *et al.* (2015), an elevation of latent heat flux does not necessarily lead to an increase in low-level moisture and thereby to an increase in CAPE. In their study, the amount of low-level moisture at 10°N is slightly less than that at 30°N, in spite of the larger surface evaporation at 10°N. The results of the present study confirm these results as shown in panels (c) and (d) of Figure 5.2. These panels show the time-radius diagrams of surface water vapour mixing ratio in the two CM1 calculations. Smith *et al.* (2015) pointed out that stronger convection at 10°N is accompanied by stronger downdraughts, which bring dry air from aloft to the boundary layer, thereby decreasing the low-level moisture. This is especially true in the early stages of vortex intensification when there is still dry air aloft.

However, the fact that the amount of low-level moisture is slightly less at 10°N than at 30°N may still seem surprising, especially because the vertical motion in the eyewall is notably stronger at 10°N, suggesting a larger degree of convective instability at a lower latitude. Figures 5.2e and 5.2f show time-radius diagrams of azimuthally-averaged vertical velocity in the middle troposphere at a height of 6.3 km in the two calculations. As expected, a positive vertical motion develops in the inner-core region of the vortices as they begin to intensify, but the strength of the eyewall updraught during the rapid intensification is considerably larger at 10°N. There is generally subsidence at outer radii (not shown). We know that the presumed larger convective instability at 10°N that could account for the stronger vertical motion in the eyewall at this latitude does not arise from an increase in low-level moisture, so where would it come from? We address this question in the next section.

5.2.2 Convective instability issue

As already discussed briefly in Chapter 4, the initial idealized vortices at various latitudes have different balanced temperature and density distributions, since the initial wind field distribution is defined to be the same in all experiments. The height-radius cross sections of the initial temperature perturbation fields at latitudes 10°N, 20°N and 30°N, corresponding to the same prescribed tangential wind, were shown in Figure 4.4. As discussed by Smith *et al.* (2015), the increased strength and radial extent of the temperature anomaly with increasing latitude would imply a decrease in CAPE and an increase in Convective Inhibition (CIN). However, since the differences in the initial temperature fields were shown to be relatively small (i.e., the difference in maximum temperature deviation between 10°N and 30°N are less than 0.2 K), one might suppose that this minor reduction of the initial upper-level stability associated with the low-latitude vortex cannot alone account for the stronger eyewall updraught at 10°N.

To test the foregoing assumption we show in Figure 5.3 the time-radius diagrams of

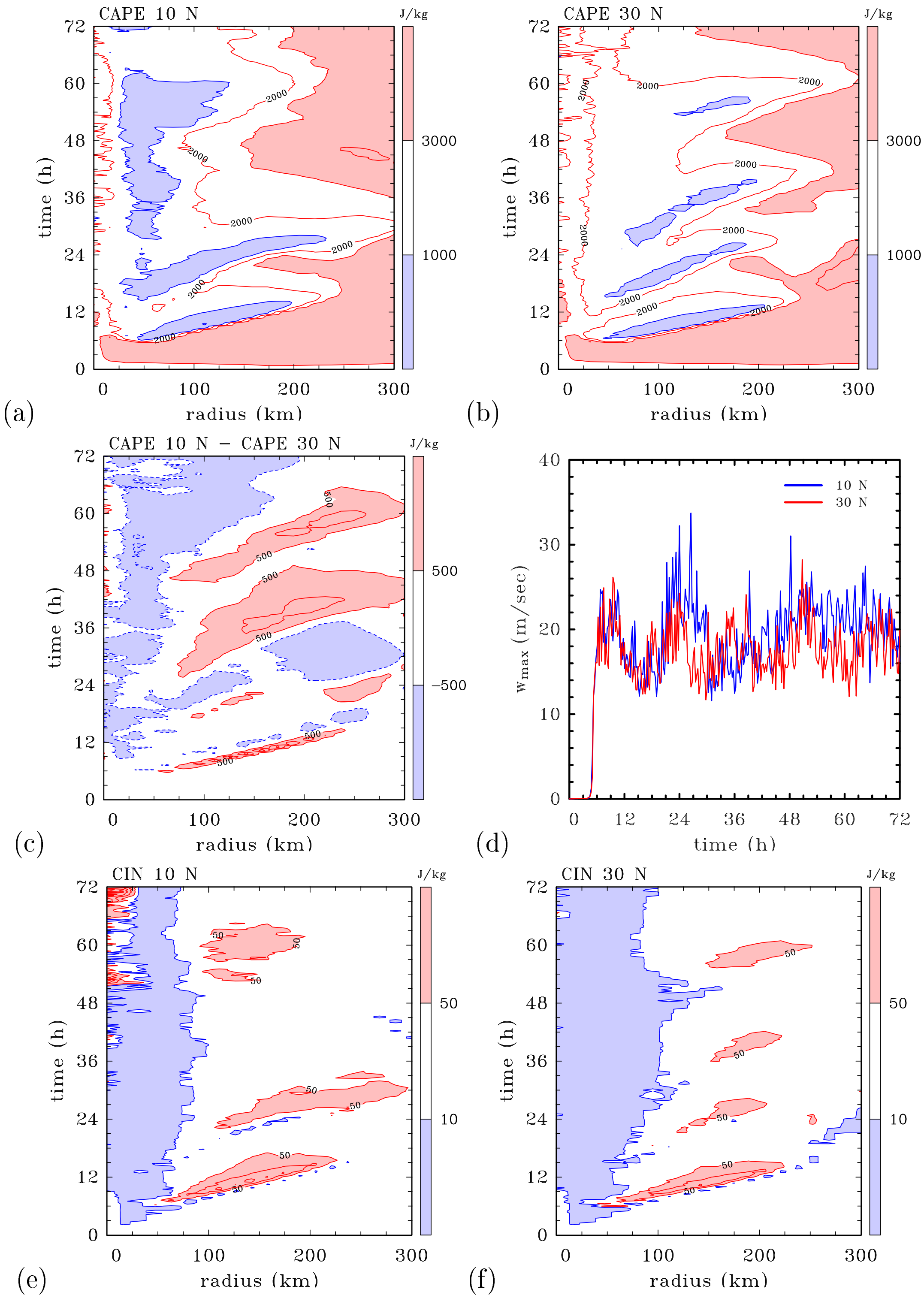

Figure 5.3: Time-radius plots of CAPE (panels a and b) and CIN (panels e and f) based on azimuthally-averaged thermodynamic data in the CM1 calculations at 10°N and 30°N with an SST of 28°C. Panel (c) shows the difference in CAPE between these two calculations, while panel (d) shows time series of the maximum vertical velocity (not azimuthally averaged) in the two calculations. The contour interval in (a), (b) and (c) is 1000 J kg^{-1}. Shading as indicated in the colour bar.

CAPE[2] (panels a and b) and CIN (panels e and f), based on azimuthally-averaged thermodynamic data in the calculations at 10°N and 30°N. Panel (c) shows the difference in CAPE between 10°N and 30°N, while panel (d) shows a time series of maximum vertical velocity in the two calculations and provides an insight into the evolution of the inner-core convection (i.e., its start and strength).

Initially (at $t = 0$ h), the distribution of CAPE at 10°N exhibits a monotonic increase with radius from approximately 2350 J kg^{-1} in the inner-core region of the vortex to 2660 J kg^{-1} at the radius of 300 km from the storm centre. As predicted above, the initial CAPE at 30°N is only marginally lower, increasing radially outwards from about 2270 J kg^{-1} at the centre to a value of 2640 J kg^{-1} at 300 km. Also the initial CIN values are similar at both latitudes (Figs. 5.3e and 5.3f), amounting to approximately 30 J kg^{-1}. In the first few hours of simulation CAPE is rapidly created by the surface moisture fluxes and CIN is rapidly reduced, but the differences in CAPE and CIN between the two latitudes remain negligible. After about 6 hours the convection begins to develop in both calculations (Fig. 5.3d) and consumes the low-level moisture as well as the CAPE. As time proceeds, the stronger convection at 10°N leads to a larger reduction of surface moisture and CAPE, compared with the 30°N calculation. From about 12 h until the end of integration time, CAPE at 10°N is generally less than that at 30°N throughout the entire inner-core region, with the differences exceeding 500 J kg^{-1} (Fig. 5.3c).

These results indicate that the differences in CAPE and CIN between the 10°N and 30°N do not provide an explanation for the differences in the vertical velocity between the two calculations diagnosed in the middle troposphere.

5.2.3 Diabatically-forced overturning circulation

The balanced theory for the secondary circulation of tropical cyclones introduced in section 2.1.2 dictates that the latent heat release in deep convective clouds will produce an inflow in the lower troposphere. The upper panels of Figure 5.4 show the distribution of azimuthally-averaged diabatic heating rate, $<\dot{\theta}>$, in the lowest 12 km for the calculations at 10°N (panel a) and 30°N (panel b). Moreover, these quantities are time averaged over a three hour period (30–32 h). One can see there is a profound difference in magnitude of the mean diabatic heating rate and its radial gradient between the two latitudes. The maximum $<\dot{\theta}>$ at 10°N exceeds 19 K h^{-1}, while at 30°N it is only 4 K h^{-1}. Following the theory of Sawyer and Eliassen, the larger negative radial gradient of the diabatic heating rate at 10°N would lead to a stronger overturning circulation, even if the latitudes were the same. In addition, a lower latitude is a second beneficial factor, because the inertial stability parameter I^2, defined in section 2.1.2, decreases with decreasing latitude. Lower inertial (centrifugal) stability at a lower latitude implies that the air parcels can be displaced further radially inwards towards the axis of rotation. Due to issues discussed above, we expect the secondary circulation to be stronger at 10°N than at 30°N. Furthermore, we

---

[2] The calculation of CAPE and CIN values given in this study is identical to that of Smith *et al.* (2015). For more details, see their Appendix [A]: Calculation of CAPE.

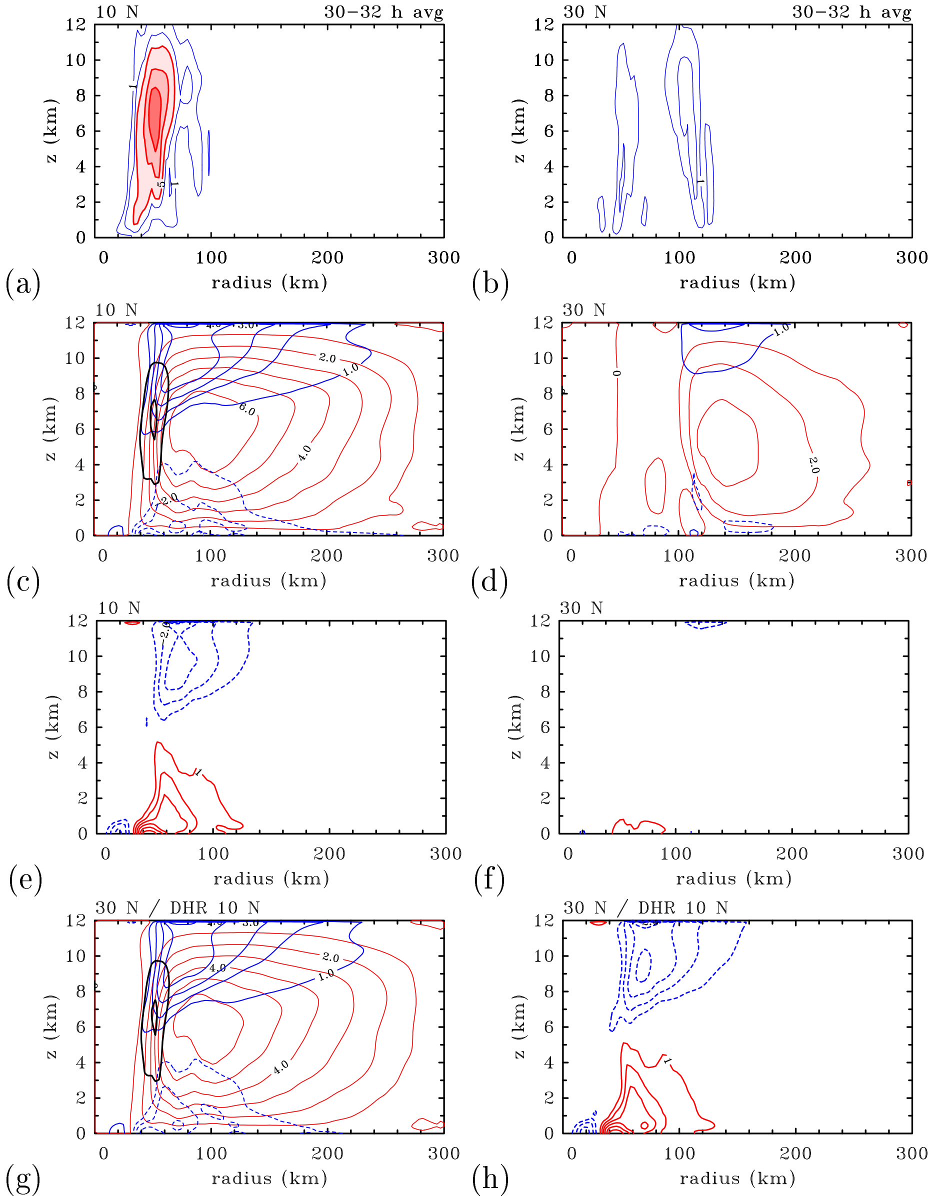

Figure 5.4: Height-radius plots of the time-averaged diabatic heating rate for the period 30-32 h, based on azimuthally-averaged fields from the CM1 calculations at (a) 10°N and (b) 30°N with an SST of 28°C. Contour interval is 2 K h^{-1} for thin blue contours and 5 K h^{-1} for thick red contours. Values between 5 and 10 K h^{-1} are shaded light pink, values between 10 and 15 K h^{-1} are shaded light red and those greater than 15 K h^{-1} are shaded darker red. Panels (c) and (d) show the corresponding streamfunction of the secondary circulation obtained by solving the Sawyer-Eliassen equation for the initial vortex with these heating rates as forcing (red contours, interval 1 x 10^8 kg s^{-1}). These panels show also the contours of radial wind (interval 1 m s^{-1}, positive values are solid blue, negative values are dashed blue) and vertical velocity (black contours, interval 0.5 m s^{-1}). Panels (e) and (f) show the corresponding tendencies of the balanced tangential wind (contour interval 1 m s^{-1} h^{-1}, positive values are solid red, negative values are dashed blue). Panels (g) and (h) show the streamfunction and tendency when the Sawyer-Eliassen equation is solved for the heating rate in (a) at latitude 30°N.

expect the maximum inflow to occur closer to the storm axis at 10°N compared with 30°N.

Figures 5.4c and 5.4d show the contours of the streamfunction obtained by solving the Sawyer-Eliassen equation[3] for the initial vortex forced with the heating rate distributions from panels (a) and (b), respectively, and with the corresponding Coriolis parameter. The isotachs of radial and vertical velocities derived from the balanced streamfunction (using Eqs. 2.11 and 2.12 from section 2.1.2) are shown also. The balanced secondary circulation is clearly much stronger in the 10°N calculation. The maximum vertical velocity at this latitude is 1.1 m s^{-1}, compared with only 0.2 m s^{-1} in the 30°N calculation. Similarly, the maximum inflow velocity at 10°N amounts to approximately 4.3 m s^{-1}, compared with 1.4 m s^{-1} at 30°N. However, the stronger inflow at a lower latitude will not necessarily lead to a faster spin up, because the tendency of the tangential wind due to radial influx of absolute vorticity is the product of the inflow velocity and the absolute vorticity:

$$\frac{\partial v}{\partial t} = -u(\zeta + f) - wS + \dot{V}. \tag{5.1}$$

The upper equation is the azimuthal momentum equation from section 2.1.2, but written here as a diagnostic expression for the tangential wind tendency. Because the absolute vorticity is the sum of relative vorticity and the Coriolis parameter, which increases with increasing latitude, one has to do the calculation to determine the net effect of the vorticity flux term on the tangential wind tendency. The results of this calculation are shown in Figures 5.4e and 5.4f for latitudes 10°N and 30°N, respectively. The tangential wind tendency is significantly larger in the 10°N calculation with the maximum reaching 6.8 m s^{-1} h^{-1}, compared with 1.8 m s^{-1} h^{-1} in the 30°N calculation.

Since we have shown in the previous section that the CAPE is actually less in the 10°N calculation than in the 30°N calculation, the large difference in diagnosed diabatic heating rates, which are closely tied to the vertical velocity ($\dot{\theta} \propto w$), cannot be explained in terms of differences in updraught buoyancy. As noted by Smith *et al.* (2015), the explanation for this difference must be attributed either to the difference in the vertical velocity exiting the boundary layer, or to the effects of rotational stiffness above the boundary layer. Larger inertial stability at higher latitudes would suppress the inflow and thereby, via the continuity equation, inhibit the vertical motion. We aim to quantify the effect of rotational stiffness in the next section.

5.2.4 Rotational stiffness

As noted above, the stronger secondary circulation as well as the larger positive tangential wind tendency in the 10°N calculation compared with the 30°N calculation could arise from two favourable factors: a larger negative radial gradient of diabatic heating rate and decreased inertial stability at a lower latitude. The bottom panels of Figure 5.5 show the height-radius distribution of the inertial stability parameter I^2 in the initial vortices at

---

[3] Specifically, we solve Equation (14) of Bui *et al.* (2009), neglecting both frictional forcing and the "eddy terms" as defined therein in this equation.

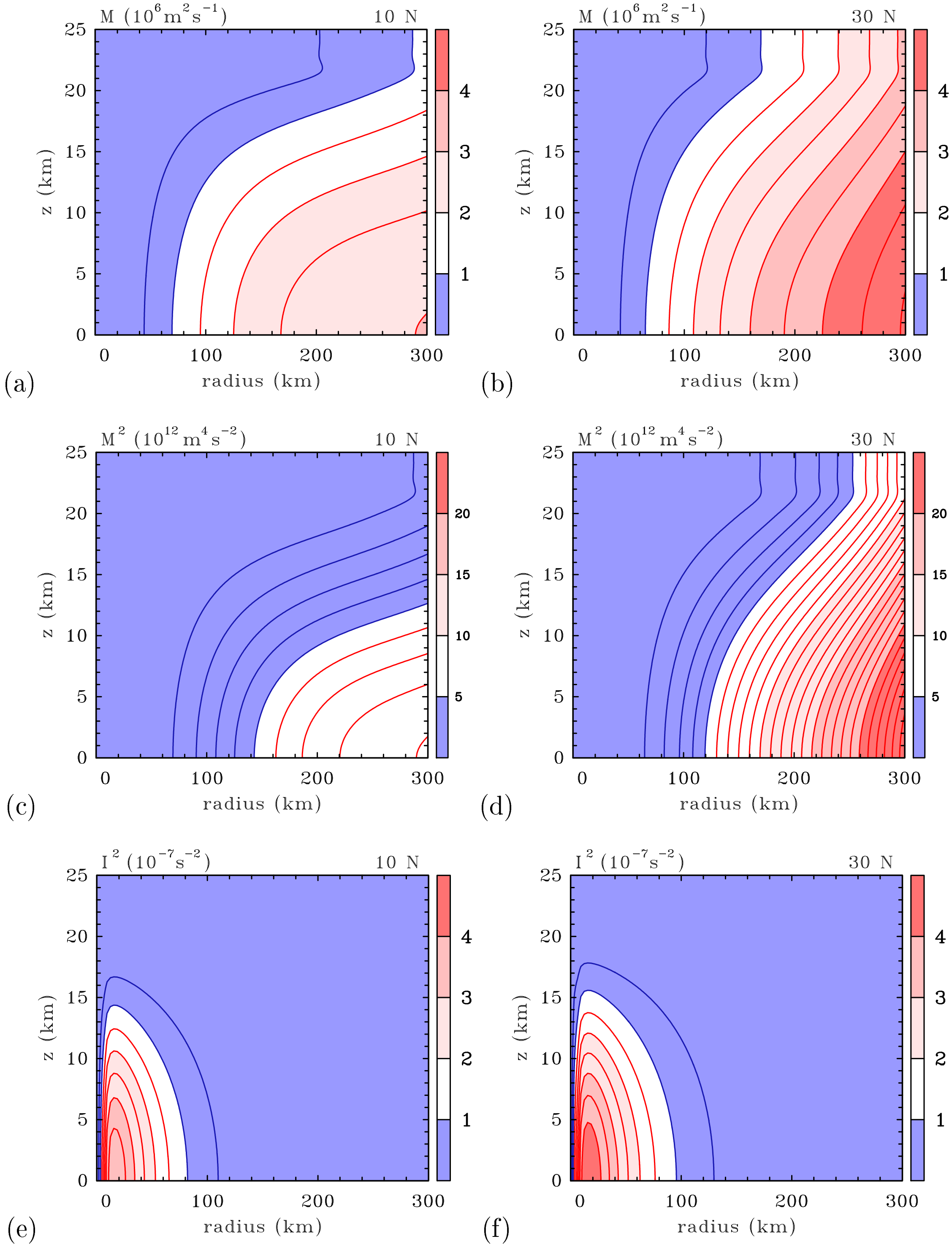

Figure 5.5: Height-radius distributions of M (top panels), M^2 (middle panels) and I^2 (bottom panels) in the initial idealized balanced vortices at 10°N (left) and 30°N (right). Here M and M^2 are the absolute angular momentum and its square, respectively, and I^2 is the inertial frequency squared. Contour interval is 0.5 x 10^6 m^2 s^{-1} in panels (a) and (b), 1 x 10^{12} m^4 s^{-2} in panels (c) and (d), and 0.5 x 10^{-7} s^{-2} in panels (e) and (f). Shading as indicated in the colour bar.

latitudes 10°N and 30°N. The parameter I^2 is proportional to radial derivative of M^2 (Eq. 2.18), the distribution of which is shown in Figures 5.5c and 5.5d for the two latitudes. As predicted above, the inertial stability is especially high in the inner-core region and increases with increasing latitude. However, if the Rossby number[4] is of order 1 or greater, as is often the case in tropical cyclones, especially in their inner-core, we do not expect this effect to be large. Nevertheless, it should be examined and quantified. In order to isolate the effect of inertial stability (rotational stiffness) we solve the Sawyer-Eliassen equation with the stronger diabatic heating rate distribution from the 10°N calculation as forcing, but with the Coriolis parameter for latitude 30°N.

The results of this calculation are shown in the bottom panels of Fig. 5.4. Figure 5.4g shows the streamfunction of the secondary circulation, together with the balanced radial and vertical wind components, while Fig. 5.4h shows the corresponding isotachs of the tangential wind tendency. These panels should be compared with panels (c) and (e), respectively, which show the results when the Sawyer-Eliassen equation was solved for the same heating rate from 10°N, but also with the corresponding Coriolis parameter for 10°N. The first important finding is that the maximum vertical velocity stays the same as before (1.1 m s^{-1}). This directly demonstrates that the rotational stiffness can not explain the stronger vertical motion diagnosed in the middle troposphere at 10°N and that the explanation for this behaviour must be attributed to the larger values of vertical velocity exiting the boundary layer at 10°N.

As expected, there is a small reduction in the maximum inflow velocity from 4.3 m s^{-1} to 4.0 m s^{-1}. However, as discussed in the previous section with the aid of tangential momentum equation (Eq. 5.1), the stronger inflow does not necessarily lead to a larger tangential wind tendency, because it is the radial flux of absolute vorticity that directly determines the tendency of the tangential wind, and not the inflow alone. Multiplication of Eq. (5.1) by r and a little manipulation leads to the equation:

$$\frac{\partial M}{\partial t} = -u\frac{\partial M}{\partial r} - w\frac{\partial M}{\partial z} - \dot{M}, \tag{5.2}$$

where $\dot{M} = r\dot{V}$. The equation (5.2) offers an alternative, but equivalent interpretation to that above, involving the radial flux of absolute angular momentum as an analogue to radial flux of absolute vorticity. This view is equivalent, because at a given radius on an f-plane M depends solely on the tangential wind (Eq. 2.20). Thus the M-tendency that can be diagnosed using the Eq. (5.2) is proportional to the tangential wind tendency.

Figures 5.5a and 5.5b show the height-radius distribution of absolute angular momentum surfaces in the initial vortices at 10°N and 30°N, respectively. Although the initial tangential wind profile is the same in both vortices, M is initially larger in the vortex at 30°N, due to a larger value of planetary vorticity at this latitude. One can see that the radial gradient of M at 30°N is larger also. In the light of Eq. (5.2) it follows that although the balanced inflow is stronger at a lower latitude, it does not necessarily imply a larger spin up, because the radial gradient of M is larger at a higher latitude and it can outweigh the effect of smaller inflow. Figure 5.4h shows that this is the case here, because the maximum tangential wind tendency at 30°N, but forced with $< \dot{\theta} >$ from 10°N, amounts to 6.9 m s^{-1} h^{-1}. This is slightly higher than the maximum tendency in the calculation at 10°N forced with the same heating rate (6.8 m s^{-1} h^{-1}). Taken together, these results demonstrate that a smaller intensification rate of a high-latitude vortex compared with a low-latitude vortex in the CM1 calculations can not be attributed to the larger inertial stability at higher latitude.

---

[4] The Rossby number is a nondimensional parameter that identifies the relative importance of the inertial and Coriolis terms in the Navier Stokes equations. It is defined as: $Ro = U/(fL)$, where U is the velocity scale, L is the horizontal length scale and f is the Coriolis parameter.

5.2.5 Convective mass flux

A complementary measure of the strength of the secondary circulation is the vertical mass flux carried by the circulation in the eyewall updraught (Kilroy *et al.* 2015). To be precise, it is the difference between the azimuthally-averaged vertical mass flux in the middle troposphere and that above the boundary layer (i.e., the net mass flux) that characterizes the ability of the eyewall convection to ventilate the air mass expelled by the inner-core boundary layer. If not all of the mass ejected from the boundary layer can be accepted by eyewall updraught, the residual will flow radially outwards above the boundary layer, causing a spin down of the tangential wind as a result of absolute angular momentum conservation. The upper panels of Figure 5.6 show time series of radially integrated mass flux at heights of 6.3 km and 1.7 km in the calculations at 10°N and 30°N. The integration was carried out to 300 km in the radial direction.

All four curves shown in these panels reach their first peak at about 9 h. Recall from Fig. 5.4d that this is approximately the time at which the convection is initiated in both calculations. During the initial period lasting about 16 hours, the mass flux at each of the two height levels is approximately the same at both latitudes. From then on until the end of integration time, the mass flux at 10°N greatly surpasses that at 30°N at both observed heights. On average, the convective mass flux at 10°N is about twice as large as that at 30°N. Since vertical mass flux is proportional to the vertical velocity, the differences in mass flux between 10°N and 30°N at a height of 6.3 km are consistent with the diagnosed differences in vertical velocity at this height (Figs. 5.2e and 5.2f). Equivalently, larger mass flux at a height of 1.7 km in the 10°N calculation compared to that in the 30°N calculation suggests that the vertical velocity at the top of the boundary layer must be larger at 10°N, at least if one assumes that the density variation is small between 10°N and 30°N.

Panels (c) and (d) of Figure 5.6 show time series of the corresponding difference between mass fluxes at 6.3 km and 1.7 km in the calculations at 10°N and 30°N, respectively. As for the diabatic heating rate, this difference is larger at 10°N than at 30°N, indicating that the convection is more efficient in ventilating the air from the boundary layer at a lower latitude. Moreover, a positive convective mass flux difference is a direct indicator of a net mass inflow in the layer between 1.7 km and 6.3 km. Thus the larger positive mass flux difference at 10°N implies a stronger inflow in the lower troposphere above the boundary layer, leading to a more rapid intensification in terms of conventional spin up mechanism.

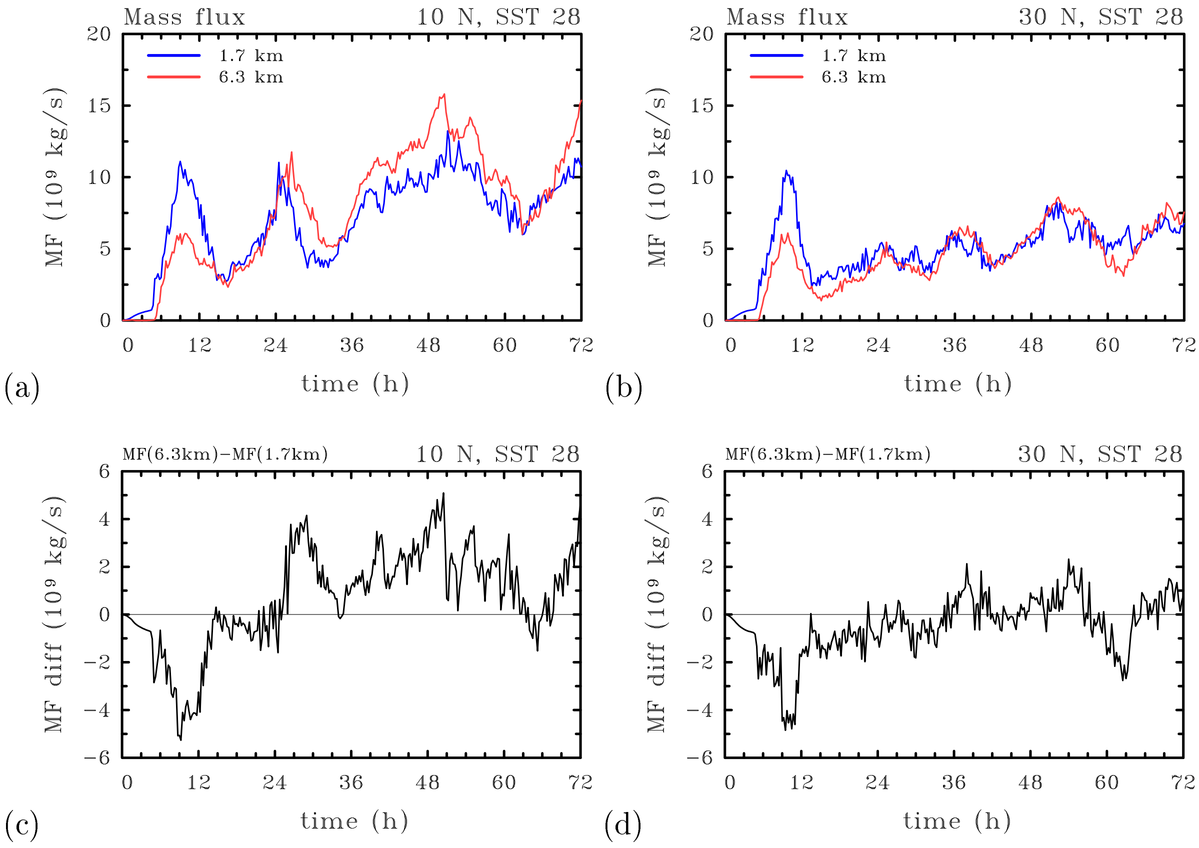

Figure 5.6: Time series of azimuthally-averaged radially integrated vertical mass flux at heights of 6.3 km and 1.7 km in the CM1 calculations at (a) 10°N and (b) 30°N with an SST of 28°C. This quantity is calculated by integrating the vertical mass flux, where it is positive, radially out to 300 km. Panels (c) and (d) show the corresponding difference between mass flux at 6.3 km and 1.7 km.

5.2.6 Boundary layer dynamics

Eliminating the effect of rotational stiffness in section 5.2.4, we have concluded that the differences in vertical velocity between 10°N and 30°N diagnosed in the middle troposphere must be due to the differences in vertical velocity of air exiting the boundary layer. An additional support for this result is larger vertical mass flux at 1.7 km in the 10°N calculation compared with the 30°N calculation. To demonstrate the idea we show in Figures 5.7a and 5.7b the time-radius distributions of azimuthally-averaged vertical velocity at the top of the boundary layer (at a height of 1.7 km) in the two calculations at 10°N and 30°N. It is clear that the vertical velocity exiting the inner-core boundary layer at 10°N is considerably larger than that at 30°N. These results are consistent with the stronger boundary layer found at 10°N compared with 30°N (Figs. 5.1e and 5.1f).

To help isolate the effect of the boundary layer, Smith *et al.* (2015) carried out addi-

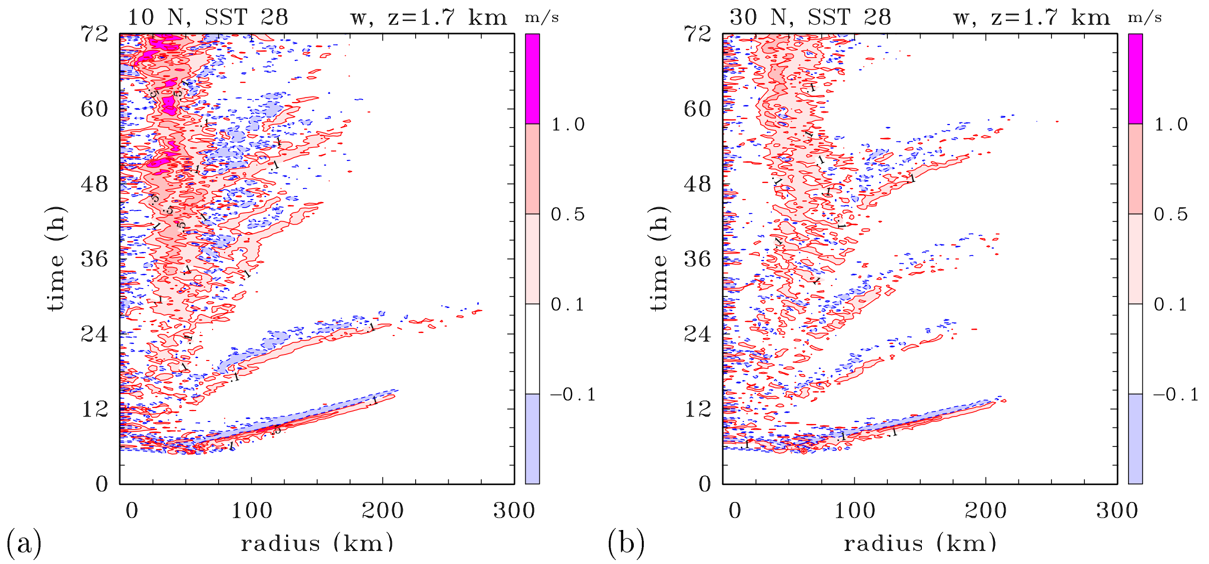

Figure 5.7: Time-radius plots of azimuthally-averaged vertical velocity at a height of 1.7 km in the CM1 calculations at latitudes (a) 10°N and (b) 30°N with an SST of 28°C.

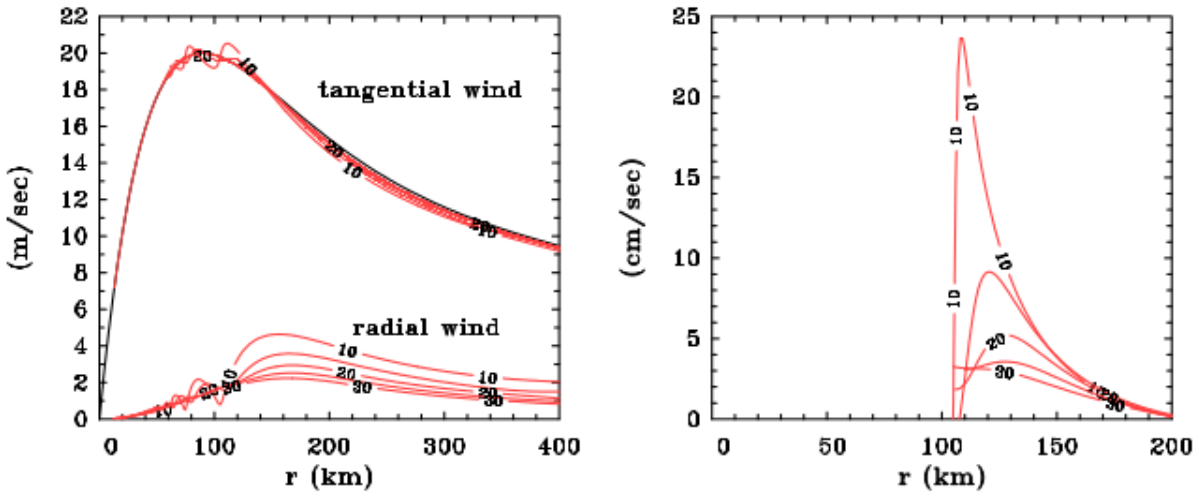

Figure 5.8: Results from the steady slab boundary layer model, adapted from Smith *et al.* (2015). Left panel shows radial profiles of radial and tangential wind components in the boundary layer for different latitudes (10°, 15°, 20°, 25° and 30°N) for a fixed profile of gradient wind at the top of the boundary layer (black line). Right panel shows the corresponding radial profiles of vertical velocity at the top of the boundary layer. The calculations are based on the assumption of a fixed boundary layer depth of 1 km.

tional boundary layer calculations for different latitudes using the steady slab boundary layer model described by Smith and Vogl (2008). They showed that, even if the tangential wind profile at the top of the boundary layer is held fixed, a simple, steady boundary layer model produces stronger low-level inflow and stronger, more confined ascent out of the boundary layer as the latitude is decreased. These results are shown in Figure 5.8 for latitudes 10°, 15°, 20°, 25° and 30°N. For a detailed discussion of the boundary layer model and its solutions see sections 3 and 4 of Smith *et al.* (2015).

5.3 Synthesis

In this chapter we investigated why numerical model simulations of tropical cyclone intensification in a quiescent environment on an f-plane show a larger rate of intensification as the latitude is decreased. After considering a number of physical processes involved in the intensification of storms, it was concluded that the dynamics of the frictional boundary layer play a key role in the explanation (Smith *et al.* 2015). In an azimuthally-averaged view of the problem, the most pronounced quantitative difference between the CM1 simulations at 10°N and 30°N is the larger radial gradient of diabatic heating rate above the boundary layer at the lower latitude. These differences were attributed to the larger vertical velocity found through the troposphere at 10°N because the heating rate, itself, is approximately proportional to the vertical velocity. Since the differences in CAPE were found to be relatively small between the two latitudes, the differences in the vertical velocity must be due to the differences in vertical velocity exiting the boundary layer. The much larger radial gradient of diabatic heating rate at 10°N produces a larger radial inflow in the low and middle troposphere, leading to an increase in the rate at which absolute angular momentum surfaces are drawn inwards. Although the radial gradient of M is larger at 30°N than at 10°N, the much larger inflow at 10°N is sufficient to give the larger rate of intensification at this latitude. These arguments for the dependence of intensification rate on latitude invoke the conventional spin up mechanism together with a boundary layer feedback mechanism linking the strength of the boundary layer inflow to that of the diabatic forcing (Smith *et al.* 2015). It was shown that the foregoing differences greatly surpass the effects of rotational stiffness and evaporative-wind feedback that have been proposed in some prior studies.

These results are consistent with those of Smith *et al.* (2015), who used an older numerical model with coarser horizontal resolution in their study, namely the Pennsylvania State University/National Center for Atmospheric Research Mesoscale Model (MM5).

Chapter 6

Dependence of tropical cyclone intensification on sea surface temperature

From the results of the previous chapter, the question immediately arises, whether there is evidence of a latitudinal dependence in observations of tropical cyclones. The answer is a qualified yes. A comprehensive statistical analysis of Atlantic hurricanes by Kaplan and DeMaria (2003) indicates that a larger proportion of low-latitude storms undergo rapid intensification[1] than storms at higher latitudes. Figure 5c from their study (Fig.

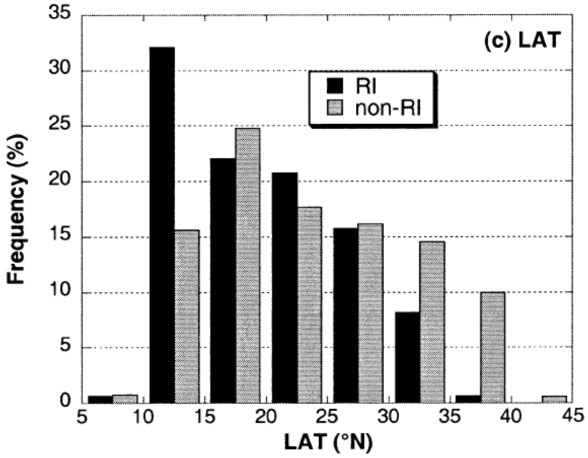

Figure 6.1: The latitudinal distribution of rapidly intensifying (RI) tropical cyclones that developed from 1989 to 2000 in the Atlantic. Shown is also the distribution of tropical cyclones from the same dataset that did not undergo RI (non-RI cases). Adapted from Kaplan and DeMaria (2003).

---

[1] In the paper by Kaplan and DeMaria (2003, p1098) an increase in maximum sustained surface wind speed of 30 kt (15.4 m s^{-1}) over a 24-hour period is used to define the RI threshold. This corresponds roughly to the definition of RI in the current study.

6.1 herein) shows notable differences between the latitudinal distributions of the RI and non-RI tropical cyclones that developed from 1989 to 2000 in the Atlantic basin. Rapid intensification occurs most frequently from 10°N to 15°N, and the fraction of RI cases generally decreases with increasing latitude. In contrast, the non-RI cases occur most frequently from 15°N to 20°N and exhibit a much slower poleward decrease (Kaplan and DeMaria 2003).

Of course, latitude is not the only environmental property affecting storm intensification: vertical shear and sea surface temperature are additional effects that may be factors playing a role in the statistics. Since sea surface temperature typically increases as the latitude decreases (Fig. 6.2), the question arises as to whether this effect might overwhelm the effects discussed in Chapter 5 in relation to the observations.

To answer this question, we present in section 6.1 the results of nine numerical simulations being combinations of three different latitudes (10°N, 20°N, 30°N) and three different SSTs (26°C, 28°C, 30°C), allowing us to isolate and quantify the effect of changing the SST on tropical cyclone intensification rate in relation to the effect of changing the latitude. A physical explanation for the dependence of tropical cyclone intensification rate on sea surface temperature is offered in section 6.2, based on axisymmetric perspective. The main findings of sections 6.1 and 6.2 are summarized in section 6.3. Some issues associated with a drift in the far-field ambient sounding, especially at the higher sea surface temperatures are examined in section 6.4.1. Finally, in section 6.4.2, nonaxisymmetric issues are touched upon briefly.

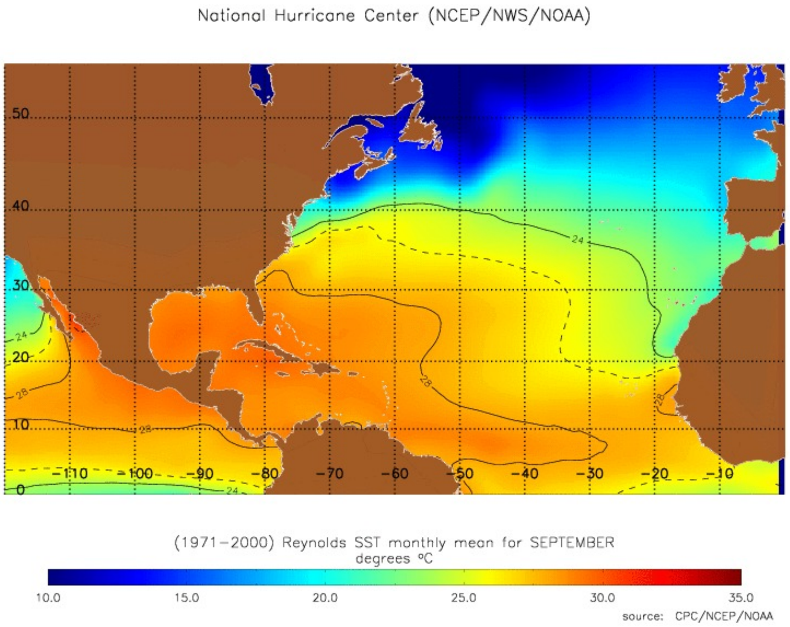

Figure 6.2: Long-term (1971-2000) monthly mean sea surface temperature in the Atlantic for September. The SST generally increases with decreasing latitude due to the increased absorption of incoming solar energy near the equator. Courtesy NHC.

6.1 Model results

We examine in the next subsection the latitudinal dependence of intensification rate (IR) at a series of fixed SSTs. Then, in the subsequent section that follows, we highlight the SST dependence of IR at a series of fixed latitudes.

6.1.1 Dependence on latitude for different SSTs

Figure 6.3 compares time series of maximum azimuthally-averaged tangential wind speed (left panels) and intensification rate (right panels) in a series of calculations for one of three different latitudes (10°N, 20°N, 30°N) combined with one of three different sea surface temperatures (26°C, 28°C, 30°C). As before, the intensification rate at time t is defined as the 24 hour change in maximum azimuthally-averaged tangential wind speed, i.e. $v_{max}(t+12$ h)$-v_{max}(t-12$ h). The black solid horizontal line in each right panel indicates the threshold value of 15 m s^{-1} day^{-1}. Values of IR exceeding this threshold are used to characterize rapid intensification.

The upper panels of Figure 6.3 show the time series of v_{max} and IR in the calculations with the lowest SST (26°C). It can be seen that the intensification is more rapid when the latitude is decreased. After 72 h, v_{max} for the vortex at 10°N is approximately 37 m s^{-1}. In contrast, at this time, v_{max} for the vortices at 20°N and 30°N are much less with values of $\sim$27 m s^{-1} and $\sim$20 m s^{-1}, respectively. Only the vortex at 10°N has an intensification rate exceeding the criterion for RI. This RI period begins at about 40 h and lasts about 20 h. The intensification rates of the vortices at 20°N and 30°N attain maxima of 11 m s^{-1} day^{-1} and 5 m s^{-1} day^{-1}, respectively.

The middle and lower panels of Figure 6.3 show the corresponding time series for SSTs of 28°C and 30°C. At these SSTs, all vortices undergo a period of RI and, as for the lowest SST, the intensification rate decreases with increasing latitude and the time at which RI begins occurs later. The vortices at 28°C and 30°C reach approximately the same[2] intensity after 72 h, and this intensity increases with SST (about 50 m s^{-1} at 28°C and 70 m s^{-1} at 30°C). These results confirm and extend those of Smith *et al.* (2015) examining the latitudinal dependence only. In particular, the results show that the dependence of the intensification rate on latitude becomes comparatively less important as the SST is increased.

Table 6.1 shows values of various parameters in the nine CM1 calculations, including: time at which rapid intensification starts (t_{start}), maximum intensification rate (IR_{max}), time at which this maximum is reached (t_{max}) and final intensity of the vortices after 72 h ($v_{max,72h}$).

---

[2] As pointed out by Nguyen *et al.* (2008) and Shin and Smith (2008), there will be an intrinsic variability of vortex intensity in calculations that start from slightly perturbed initial conditions on account of the stochastic nature of deep convection. Therefore, small differences between the intensity of two deterministic calculations of a few m s^{-1} should not be regarded as particularly significant.

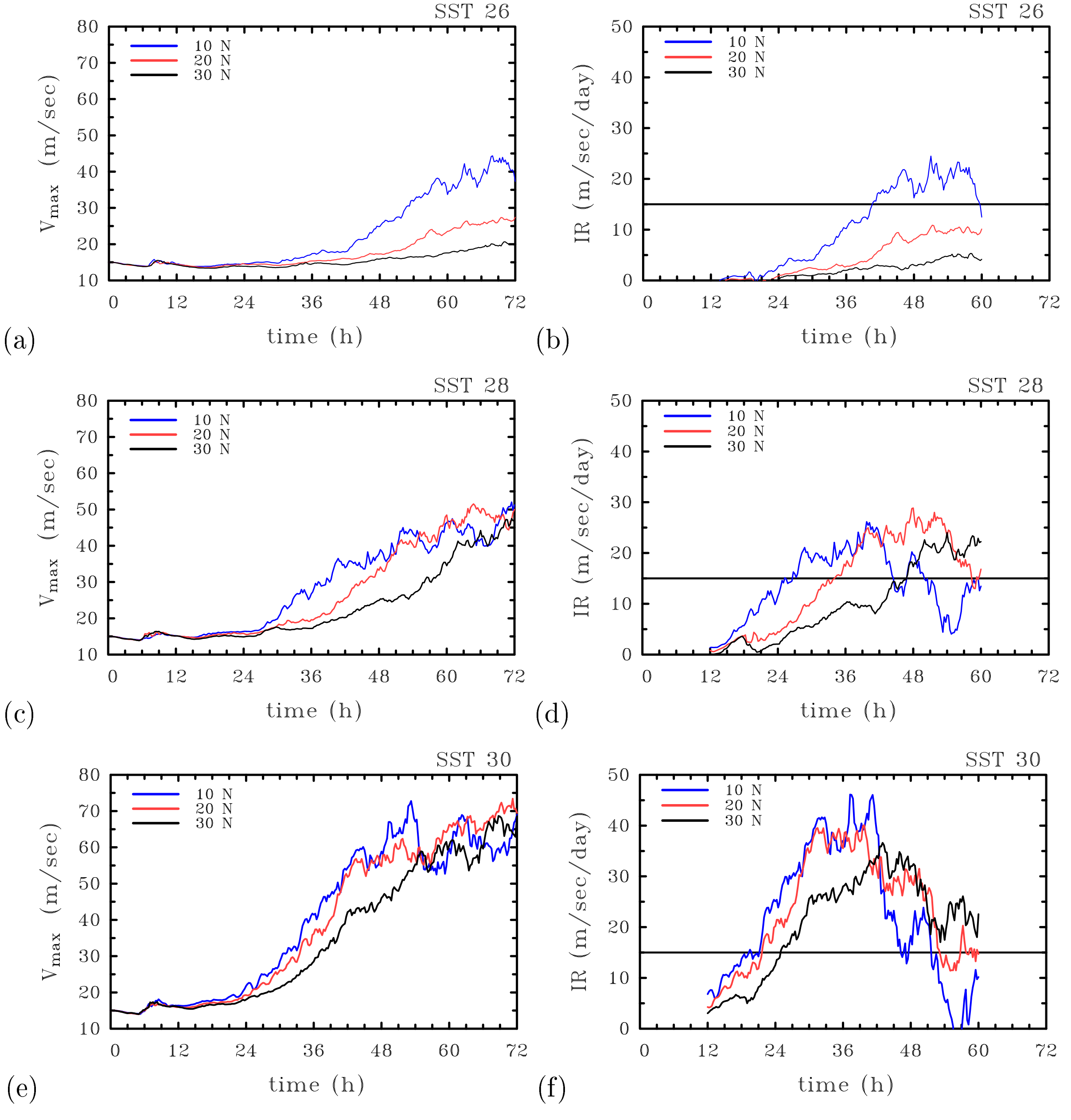

Figure 6.3: Time series of maximum azimuthally-averaged tangential wind speed (left) and intensification rate (right) in the nine CM1 calculations at three different latitudes (10°N, 20°N, 30°N) combined with three different SSTs: 26°C (upper panels), 28°C (middle panels) and 30°C (bottom panels).

SST (°C)	LAT (°N)	t_{start} (h)	IR_{max} (m s^{-1} day^{-1})	t_{max} (h)	$v_{max,72h}$ (m s^{-1})
26	10	40,75	25,0	51,00	37,3
26	20	/	10,9	51,25	27,4
26	30	/	5,3	58,00	20,0
28	10	25,25	26,2	39,75	51,3
28	20	34,25	28,9	48,00	50,0
28	30	47,00	24,0	54,00	47,2
30	10	19,50	46,1	37,25	69,0
30	20	21,75	40,1	39,75	69,5
30	30	25,00	36,6	43,00	68,6

Table 6.1: Values of various parameters in the nine CM1 calculations, including: time at which rapid intensification starts (t_{start}), maximum intensification rate achieved during the integration time (IR_{max}), time at which this maximum is reached (t_{max}) and final intensity of the vortices after 72 h ($v_{max,72h}$). Blank values in the third column indicate that rapid intensification did not occur in these two cases.

6.1.2 Dependence on SST at different latitudes

We examine now the dependence of vortex intensification on SST at various fixed latitudes. While the information on this dependence is contained in Figure 6.3, it may be helpful to reorder the curves in a way that highlights the dependence on SST as in Figure 6.4. In contrast to the dependence on latitude at a fixed SST, it is seen that there is a strong dependence of intensification rate and the time at which RI commences on the SST at *all* latitudes. As might be expected, the intensification is more rapid as the SST is increased (see right panels of Figure 6.4). Moreover, the onset of RI occurs earlier (when it occurs at all) and the duration of RI is longer as the SST is increased. For this reason, the final intensity after 3 days is larger for larger SSTs, although the difference is less at 10°N than at higher latitudes (possibly because the vortices at this latitude have achieved a greater degree of maturity). In the next section we explore the reasons for the foregoing behaviour.

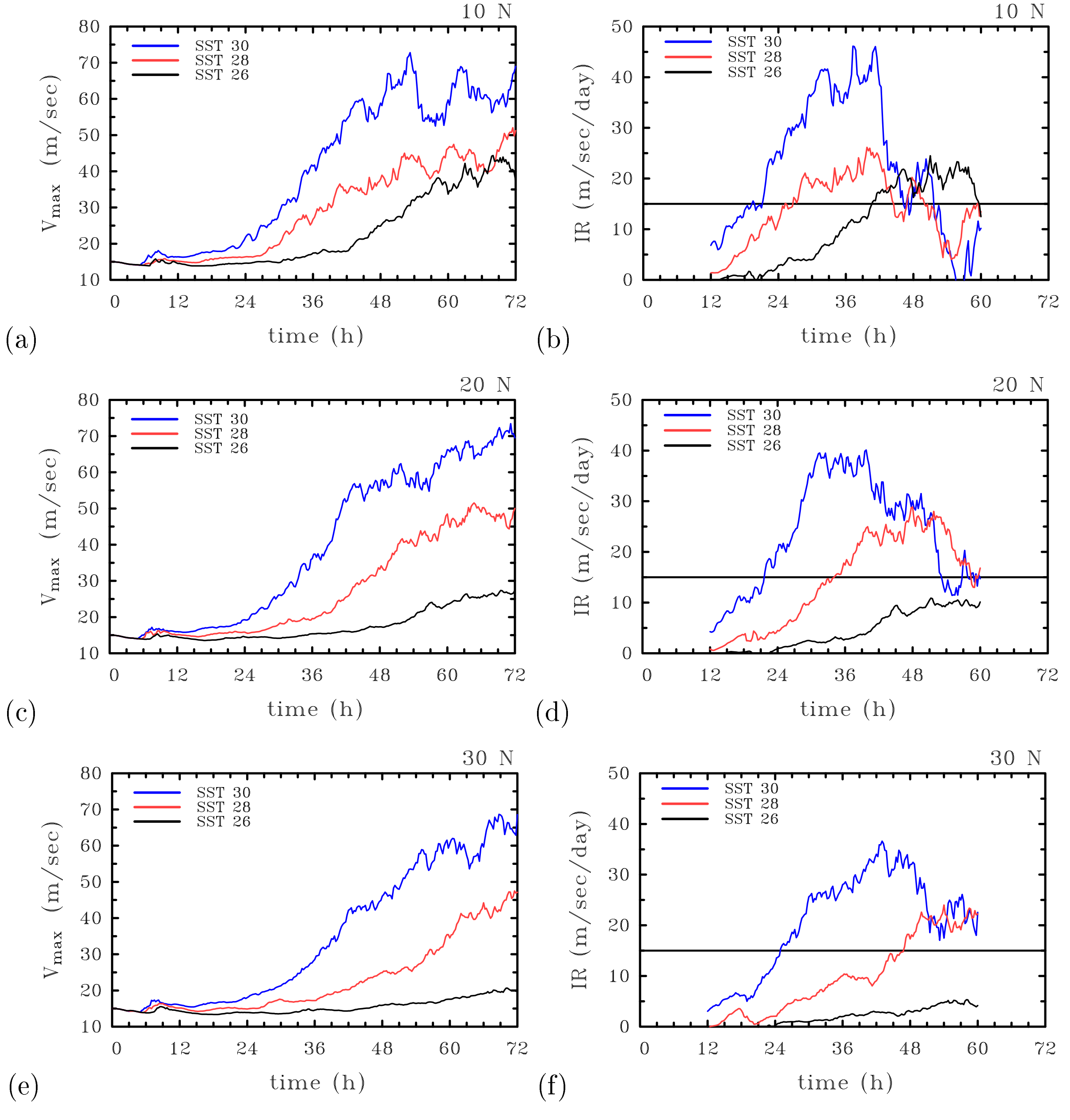

Figure 6.4: Time series of maximum azimuthally-averaged tangential wind speed (left) and intensification rate (right) in the nine CM1 calculations with three different SSTs (26°C, 28°C, 30°C) combined with three different latitudes: 10°N (top panels), 20°N (middle panels) and 30°N (bottom panels).

6.2 Interpretation of the SST dependence

In the previous section we sought to quantify the dependence of vortex intensification rate on SST at different fixed latitudes compared with the intensification rate dependence on latitude at different fixed SSTs. The aim, as outlined in the Introduction, was to assess the applicability of the results of Smith *et al.* (2015) to explain the observational climatology of RI of Kaplan and DeMaria (2003). We showed that, at a given latitude, the intensification rate is significantly larger and the intensification begins sooner for larger values of SST. Here we examine why there is this strong dependence of intensification rate on SST.

6.2.1 Boundary layer moisture budget

In seeking an explanation, the obvious place to start is to examine the differences in the azimuthally-averaged latent heat fluxes as a function of radius and time. This is because the saturation specific humidity increases exponentially with temperature, implying a strong dependence of surface evaporation on the SST and a possibly greater disequilibrium in moisture at the sea surface[3].

The surface latent heat fluxes are shown in Figure 6.5 for all nine experiments. For a fixed SST, the magnitude of the fluxes decreases with latitude and at a fixed latitude, it increases with increasing SST, the dependence on SST being much stronger than that on latitude. Even so, as shown in Chapter 5, an elevation of latent heat flux does not necessarily lead to an increase in low-level moisture and thereby to an increase in low-level equivalent potential temperature and CAPE. We showed that the amount of low-level moisture at 10°N is slightly less than that at 30°N (for a fixed SST of 28°C), in spite of the larger surface evaporation at 10°N. We pointed out that stronger convection at 10°N is accompanied by stronger downdraughts, which bring dry air from aloft to the boundary layer, thereby decreasing the low-level moisture.

We have examined the time-radius profiles of surface water vapour mixing ratio in all nine experiments (not shown). For SSTs of 26°C and 30°C the results are qualitatively similar to those for 28°C described above with the low-level moisture amount being generally less at lower latitudes than at higher latitudes. On the contrary, at a particular *fixed* latitude, the remarkable increase of surface enthalpy fluxes in the calculations with higher SSTs compared to those at lower SSTs is sufficient to result in appreciably larger amount of low-level moisture at higher SSTs. These higher values of low-level moisture are reflected in a larger equivalent potential temperature θ_e as indicated in Figure 6.6. This figure shows Hovmöller diagrams of azimuthally-averaged θ_e at a height of 1.1 km for all nine experiments. We show here θ_e in preference to mixing ratio because it not only increases monotonically with mixing ratio, but it is an approximately conserved quantity both in dry and moist ascent. Moreover, its radial distribution as it exits the boundary layer is *one* important factor affecting the radial distribution of diabatic heating rate, the other being the radial distribution of vertical velocity at this level (see e.g. section 6 of Smith *et al.* 2015b).

---

[3] In a bulk formulation, the moisture flux is proportional to the near-surface wind speed and the degree of disequilibrium, defined as the difference between the saturation specific humidity at the SST and the specific humidity of the near-surface air. Here, "near-surface" is taken conventionally as 10 m altitude.

6.2.2 Convective instability issue

At a given latitude, larger amount of low-level moisture (or equivalently, larger values of low-level θ_e) at higher SSTs, result in a larger degree of convective instability, as measured by CAPE. Panels (a), (b) and (c) of Figure 6.7 show Hovmöller diagrams of CAPE in the three calculations at 20°N. Because the initial vortices at a given fixed latitude are identical (i.e., possess exactly the same temperature and moisture fields), the CAPE at the initial time ($t = 0$ h) is the same in all three experiments. However, immediately after the simulation start CAPE is rapidly created by the surface fluxes. Between 3 to about 6 to 9 h (depending on the radius), there is a much larger increase in CAPE at higher SSTs on account of considerably larger surface enthalpy fluxes. Precisely, during this time period, CAPE exceeds 4000 J kg^{-1} in the calculation with 30°C, while it is only about 2500-3000 J kg^{-1} in the calculation with 26°C. After the onset of convection at about 6 to 9 h (the exact time is again dependent on the radius), the CAPE decreases in all three calculations to values lower than 1000 J kg^{-1}. However, as time proceeds, the loss of CAPE caused by the convection and the evolving downdraughts is partially replenished by the large surface fluxes in the calculations with SSTs of 28°C and 30°C. The replenishment of the surface moisture and hence of the CAPE is most effective in the calculation with 30°C. In contrast, CAPE remains below 1000 J kg^{-1} throughout the most of the inner region in the 26°C calculation. Figure 6.7d shows the difference between the time-radius distributions of CAPE in the calculations at 20°N with SSTs of 30°C and 26°C. After 36 h this difference exceeds 1500 J kg^{-1} throughout the innermost 200 km.

6.2.3 Diabatically-forced overturning circulation

Figure 6.8 shows time-radius distribution of the azimuthally-averaged diabatic heating rate, $<\dot{\theta}>$, in the middle troposphere (at a height of 6 km) in the three simulations at latitude 20°N. There is clearly a strong dependence of $<\dot{\theta}>$ on SST. As expected, the magnitude of $<\dot{\theta}>$ and its radial gradient, $\partial <\dot{\theta}> /\partial r$, are largest when the SST is 30°C and weaken considerably as the SST is decreased. In accordance with the classical axisymmetric balance theory for intensification above the boundary layer, a stronger radial gradient of $<\dot{\theta}>$ (a measure of the convective forcing in the balance theory) leads to a stronger secondary circulation. In particular, a negative radial gradient of the diabatic heating rate leads to radial inflow in the lower troposphere at radii outside the heating (Shapiro and Willoughby 1982). This inflow draws absolute angular momentum surfaces inwards above the boundary layer and because M is approximately materially conserved above the boundary layer, the inflow leads to a spin up of tangential wind speed there.

To quantify the foregoing effect in context of balance dynamics, we diagnose first the spatial distribution of the time average of $<\dot{\theta}>$ during a three hour time interval in the

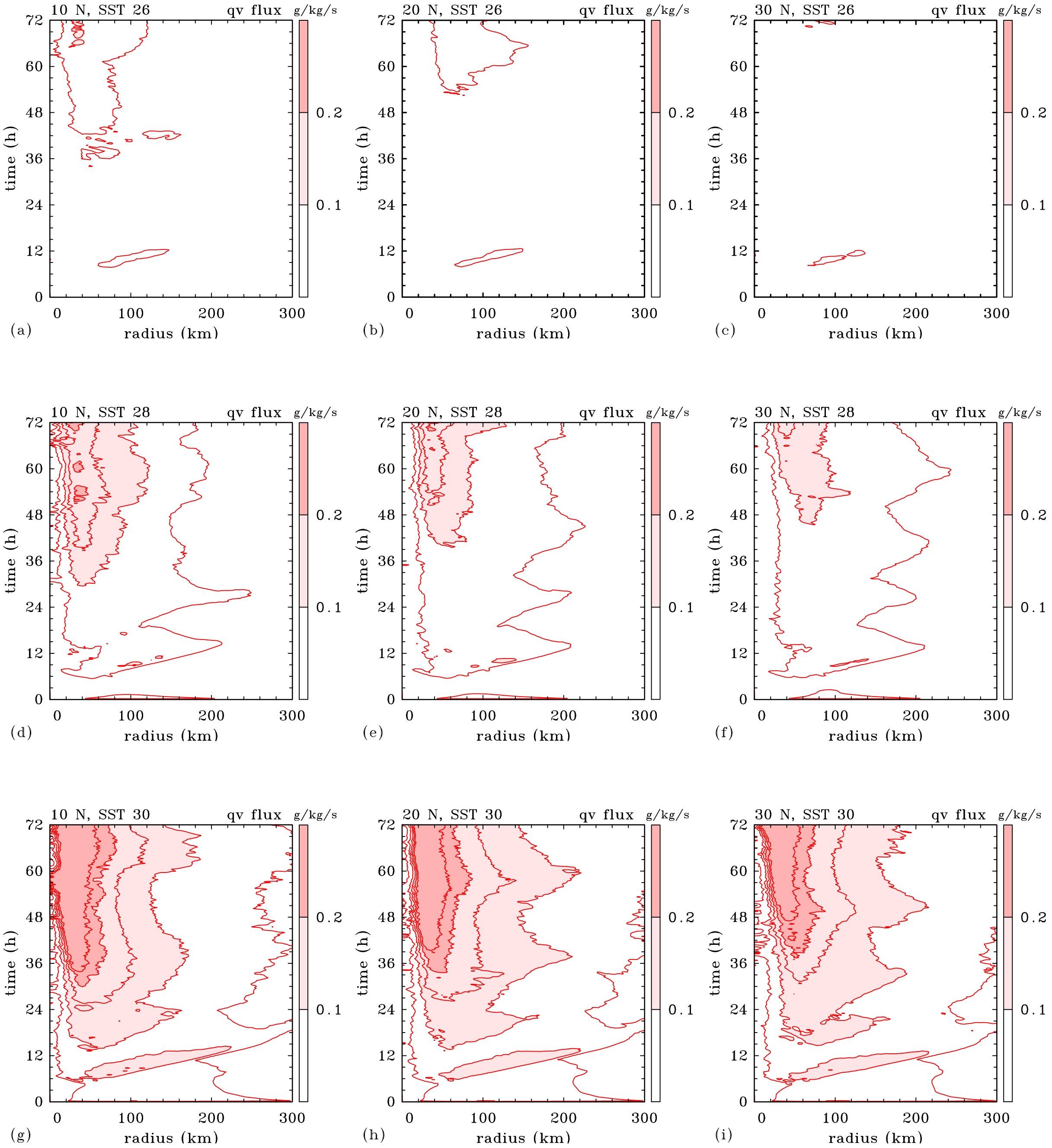

Figure 6.5: Time-radius plots of azimuthally-averaged surface water vapour fluxes in the nine CM1 calculations at 10°N (left), 20°N (centre) and 30°N (right) for an SST of 26°C (upper panels), 28°C (middle panels) and 30°C (bottom panels). Contour interval is 0.05 g kg^{-1} s^{-1}. Shading as indicated in the colour bar.

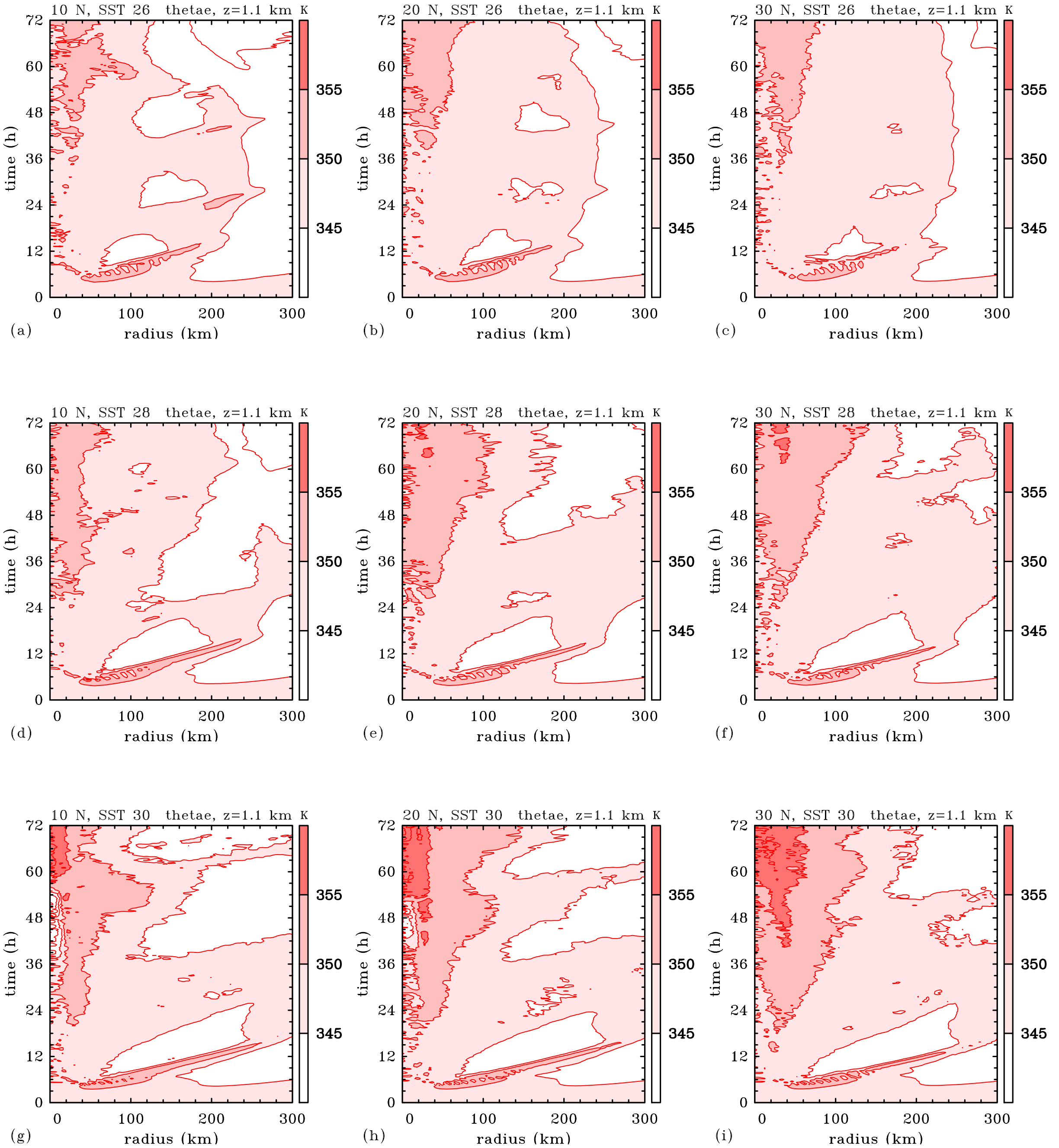

Figure 6.6: Time-radius plots of azimuthally-averaged equivalent potential temperature at a height of 1.1 km in the nine CM1 calculations at 10°N (left), 20°N (centre) and 30°N (right) for an SST of 26°C (upper panels), 28°C (middle panels) and 30°C (bottom panels). Contour interval is 5 K. Shading as indicated in the colour bar.

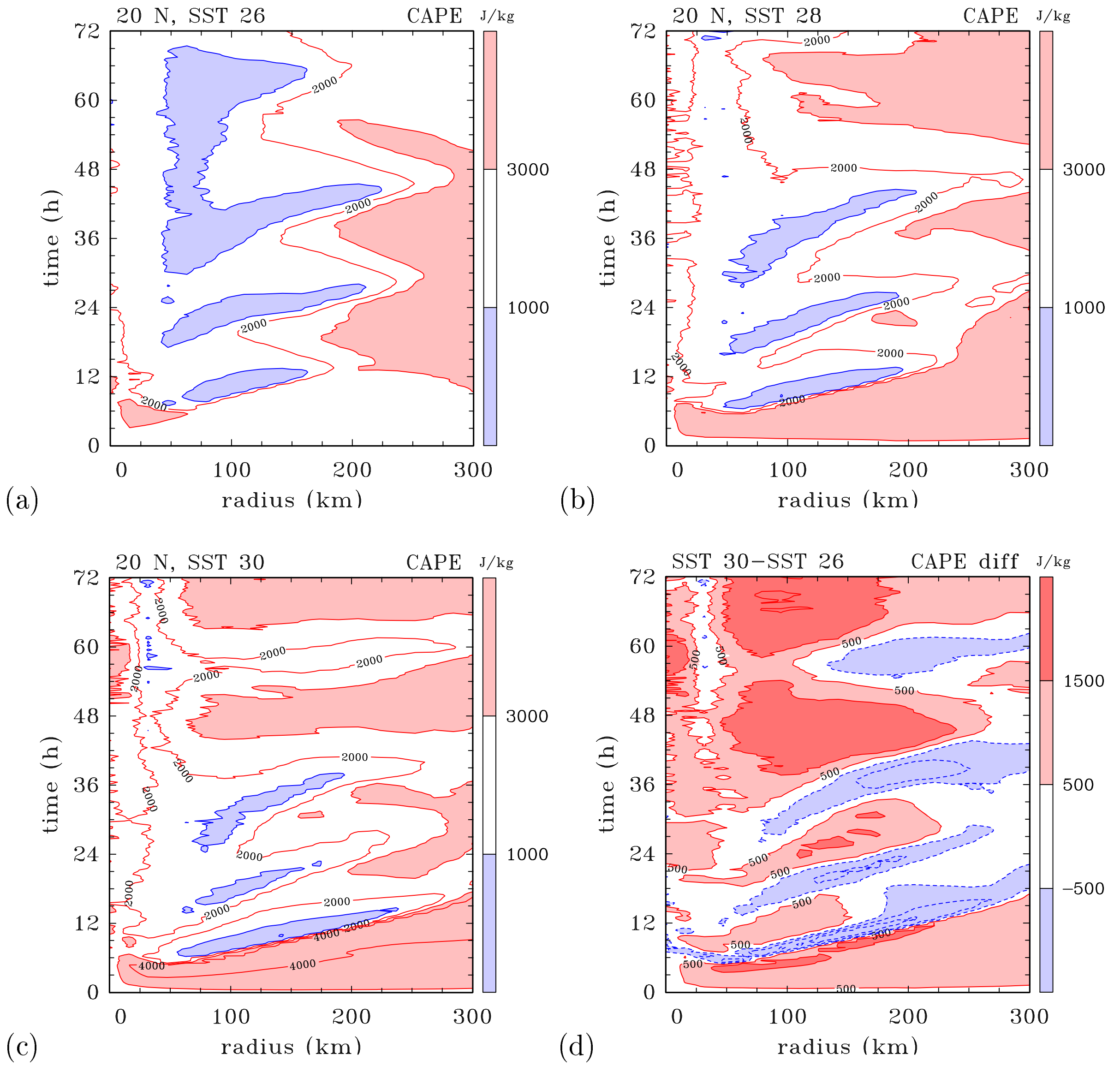

Figure 6.7: Time-radius plots of CAPE based on azimuthally-averaged thermodynamic data in the CM1 calculations at 20°N with an SST of (a) 26°C, (b) 28°C and (c) 30°C. Panel (d) shows the difference in CAPE between the calculations at 20°N with SST of 30°C and 26°C. Contour interval is 1000 J kg^{-1}. Shading as indicated in the colour bar.

middle of the rapid intensification phase for each of the three experiments. The height-radius distributions of this average are shown in the upper panels of Figure 6.9 for the three calculations at 20°N. Again it is clear that there is a large difference in the mean heating rates between the calculations. The maximum values of $<\dot{\theta}>$ reached in the calculations with SST of 26°C, 28°C and 30°C are 11 K h^{-1}, 17 K h^{-1} and 22 K h^{-1}, respectively.

Panels (d), (e) and (f) of Figure 6.9 show isotachs of radial and vertical velocity in the balanced secondary circulation obtained by solving the Sawyer-Eliassen equation for the

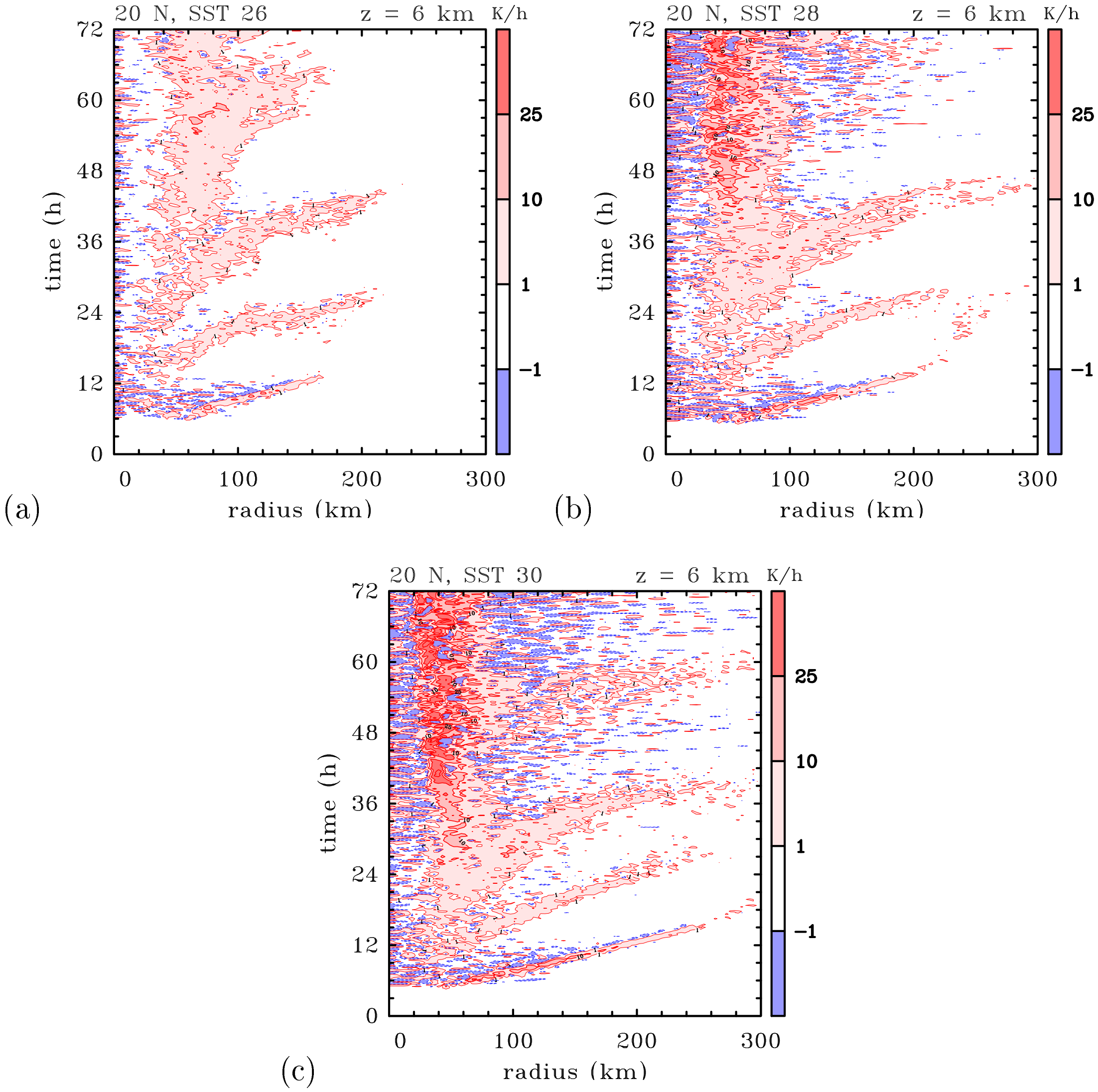

Figure 6.8: Hovmöller diagrams of azimuthally-averaged diabatic heating rate at a height of 6 km in a series of CM1 calculations at 20°N for an SST of (a) 26°C, (b) 28°C and (c) 30°C. Shading as indicated in the colour bar.

corresponding vortex and with the corresponding heating rate distribution from panels (a), (b) and (c) as forcing. Again, we solve Equation (14) of Bui *et al.* (2009), neglecting both frictional forcing and the "eddy terms". The streamfunction contours of the overturning circulation are shown in these panels also. Confirming the expectations, the balanced secondary circulation is the strongest in the calculation with the highest SST (30°C) and the weakest in the calculation with the SST of 26°C. In particular, the strongest vertical motion amounts to 1.1 m s^{-1} at 30°C, while it is only 0.5 m s^{-1} at 26°C. Similarly, the maximum low-level inflow velocity is 3.0 m s^{-1} for SST of 30°C, compared with 0.99 m s^{-1} in the calculation with the lowest SST (26°C).

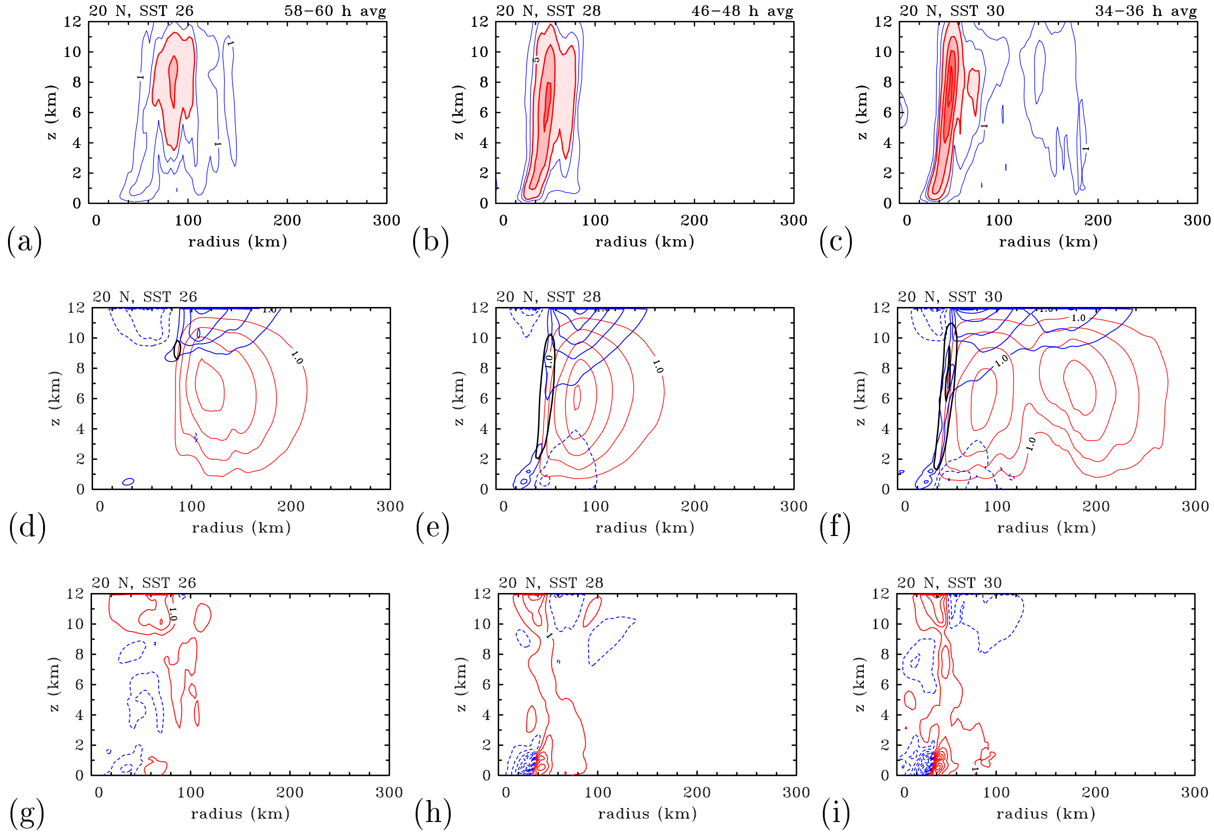

Figure 6.9: Height-radius plots of the time-averaged diabatic heating rate, based on azimuthally-averaged fields from the CM1 calculations at 20°N for an SST of (a) 26°C, (b) 28°C and (c) 30°C. Contour interval is 2 K h^{-1} for thin blue contours and 5 K h^{-1} for thick red contours. Values between 5 and 10 K h^{-1} are shaded light pink, values between 10 and 15 K h^{-1} are shaded light red and those greater than 15 K h^{-1} are shaded darker red. Panels (d), (e) and (f) show the corresponding streamfunction of the balanced secondary circulation obtained by solving the Sawyer-Eliassen equation with these heating rates as forcing terms (red contours, interval 1 x 10^8 kg s^{-1}). These panels show also the contours of radial wind speed (interval 1 m s^{-1}, positive values are solid blue, negative values are dashed blue) and vertical velocity (black contours, interval 0.5 m s^{-1}). Panels (g), (h) and (i) show the corresponding tendencies of the balanced tangential wind (contour interval 2 m s^{-1} h^{-1}, positive values are solid red, negative values are dashed blue).

Panels (g), (h) and (i) in Figure 6.9 show isotachs of the tangential wind tendency in the three calculations. As might be expected, the largest positive tendency of the tangential wind is found in the calculation with the SST of 30°C and amounts to 13.2 m s^{-1} h^{-1}. For SST of 28°C it is approximately 9.0 m s^{-1} h^{-1}, while at 26°C it is only 5.2 m s^{-1} h^{-1}.

6.2.4 Convective mass flux

Another diagnostic quantity that can be used to quantify the degree of convective activity is the vertical mass flux averaged over some area of a storm. Of particular interest is the difference between the azimuthally-averaged vertical mass flux at some middle tropospheric level and that near the top of the boundary layer. The sign of this difference provides an indication of the ability of deep convection to ventilate the air that is converging in the boundary layer. Moreover, the larger the difference the stronger is the inflow above the boundary layer on grounds of mass continuity. In turn, the stronger the inflow above the boundary layer, the stronger will be the spin up for a given radial gradient of absolute angular momentum in this region. This is essentially the conventional spin up mechanism, described in Montgomery and Smith (2014).

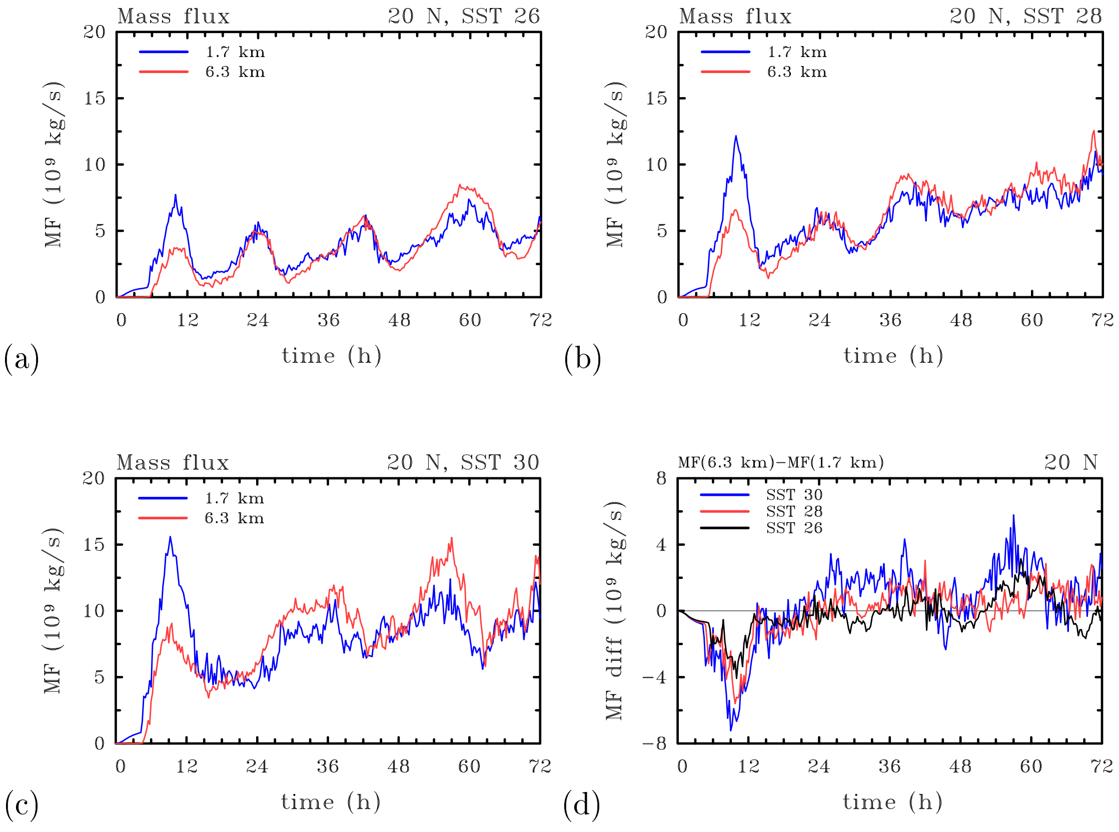

Figure 6.10: Time series of azimuthally-averaged radially integrated mass flux in the middle troposphere at a height of 6.3 km and near the top of the boundary layer at 1.7 km in the CM1 calculations at 20°N for an SST of (a) 26°C, (b) 28°C and (c) 30°C. These quantities are calculated by integrating the vertical mass flux, where it is positive, radially out to 300 km. Panel (d) shows the difference between the fluxes at 6.3 km and 1.7 km in the three calculations.

Panels (a), (b) and (c) of Figure 6.10 show time series of the radially integrated mass flux at heights of 6.3 km and 1.7 km in a series of calculations at 20°N. Examination of these figures reveals that the total value of this quantity increases with increasing SST at both observed heights. Figure 6.10d shows the difference of the corresponding mass flux curves between 6.3 km and 1.7 km in the three calculations at 20°N. Like diabatic heating rate, this difference is the largest when the SST is 30°C and the smallest when the SST is 26°C. The implication is that there will be stronger spin up above the boundary layer as the SST increases, consistent with the results shown at specific times during intensification in section 6.2.3. Results for latitudes 10°N and 30°N are qualitatively similar (not shown).

6.3 Synthesis

In this chapter we investigated why numerical model simulations of tropical cyclone intensification in a quiescent environment on an f-plane show a larger rate of intensification as the SST is increased. The effects of changing the SST were compared with those of changing the latitude. It was found that the dependence of intensification rate on latitude is largest when the SST is marginal for tropical cyclone intensification (26°C) and reduces in significance as the SST is increased to the values of 28°C and 30°C. Further, at a given latitude, intensification begins earlier and the rate of intensification increases with increasing SST on account of a significant increase of surface moisture fluxes from the warmer ocean. These higher fluxes result in higher values of near-surface moisture and equivalent potential temperature and a larger negative radial gradient of diabatic heating rate in the low to middle troposphere above the boundary layer. The larger radial gradient of heating rate leads to a stronger overturning circulation, which in turn gives rise to a stronger radial import of absolute angular momentum surfaces and therefore more rapid spin up. The difference between the radially integrated vertical mass fluxes in the middle troposphere and at the top of the boundary layer can be used as another indicator of the strength of the inner-core deep convection. It was shown that, at 20°N latitude, this difference increases with increasing SST, an indication that, collectively, deep convection has a progressively greater ability to ventilate the air that is converging towards the vortex centre as the SST is increased.

6.4 Two remaining issues

We have shown that the dependence of vortex intensification on SST in the prototype problem for intensification may be understood in terms of classical axisymmetric spin up mechanism (Montgomery and Smith 2014). However, there are two issues with the formulation and interpretation that need to be touched upon.

6.4.1 Dependence of the ambient profile on the SST

There is a potential issue in carrying out experiments at a fixed latitude when varying the SST, but keeping the ambient sounding the same. In reality, the sounding, itself, may be expected to have some dependence on the SST. One could envision a set of experiments in which the initial sounding is adjusted so as to be neutral to the model's moist convection as was done by Rotunno and Emanuel (1987, p548). One thrust of the Rotunno and Emanuel study was to demonstrate that tropical cyclone intensification does not require ambient CAPE. In essence, these authors showed that, starting from a prescribed initial vortex, the presence of wind-induced surface moisture fluxes generates adequate CAPE to support inner-core deep convection.

Elsewhere, Emanuel *et al.* (1994) have argued that levels of CAPE over the tropical oceans are minimal, sufficient only to offset the dissipation within clouds, although they use a definition of CAPE that assumes reversible adiabatic displacements. This definition includes the effects of condensed water on air parcel buoyancy and applies strictly to non-precipitating convection. On the other hand, recent observations of the environment of tropical disturbances have shown that, based on the assumption of pseudo-adiabatic ascent, there are significant levels of CAPE (Smith and Montgomery 2012). In the systems analysed by Smith and Montgomery, approximately 50% of soundings had CAPE values exceeding 1500 J kg^{-1} and approximately 10% had values exceeding 2500 J kg^{-1}. These amounts would be adequate to support modes of convective organization just as in the middle latitudes over land.

An unavoidable consequence of changing the SST without changing the initial ambient profile is that the vertical diffusion of heat and moisture near the surface may lead to a slow evolution of the ambient sounding, thereby changing the level of ambient CAPE during the integration period. While this change may not be appreciable during the comparatively short integration period here, it is an effect that calls for investigation and quantification.

The upper panels of Figure 6.11 show the time evolution of the far-field potential temperature deviation (specifically the difference between θ at a radius of 1000 km at time t and that at the initial time) in the lowest 300 m in the three simulations for latitude 10°N. The lower panels show the corresponding deviations in water vapour mixing ratio in the lowest 1 km. One might expect the magnitude of the deviations to be most extreme at this latitude. As expected, the deviations of both quantities are largest when the SST is 30°C and are almost imperceptible when the SST is 26°C. Since the near-surface air temperature of the Dunion sounding (26.7°C) exceeds 26°C, the θ actually decreases slightly with time

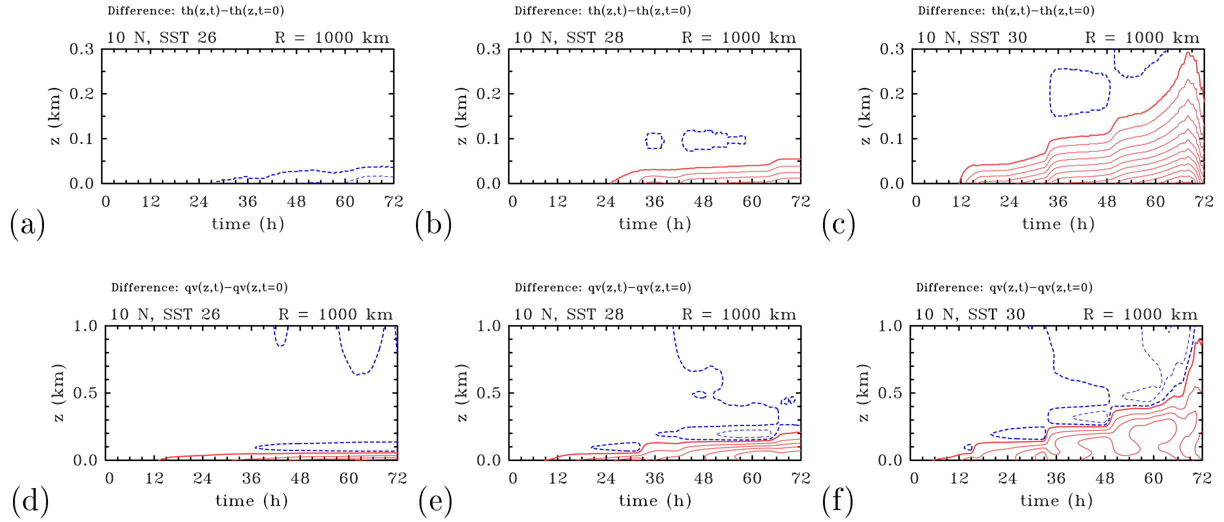

Figure 6.11: Panels (a), (b), (c): Height-time diagrams of the difference between azimuthally-averaged potential temperature at time t and that at the initial time ($t = 0$ h) in the lowest 0.3 km at a radius of 1000 km from the geometrical domain centre. Solid red contours indicate positive values, dashed blue contours indicate negative values. Contour interval is 0.1 K. The thick solid red contour is 0.1 K, the thick dashed blue contour is −0.1 K. Panels (d), (e), (f): Same diagrams, except for water vapour mixing ratio difference in the lowest 1.0 km. The first positive contour is 0.1 g kg^{-1} (thick solid red contour), the interval is 0.5 g kg^{-1} for positive values. The first negative contour is −0.1 g kg^{-1} (thick dashed blue contour), the interval is 0.2 g kg^{-1} for negative values. Shown are the results for the CM1 calculations at latitude 10°N.

when the SST is 26°C and because of the implied static stability, the decrease is confined to a very shallow layer of 50 m near the surface. In the calculations for SSTs of 28°C and 30°C, θ increases with time on account of the sensible heat fluxes from the warmer ocean surface. By 72 h, θ at the lowest model level has increased by about 1.2 K in the calculation with the highest SST (Figure 6.12a). In this most extreme case, an almost neutral layer develops in the lowest 300 m (specifically, the increase in θ across this layer reduces from 1.3°C to less than 0.2°C).

For all values of SST, there is an increase in the low-level moisture that extends through a deeper layer than the increase in potential temperature (up to about 1 km in the case of 30 deg SST), the maximum being on the order of 2 g kg^{-1} near the surface. The question is: what are the implications of these changes for the change in far-field values of CAPE. In the most extreme case, the average CAPE for the average vertical profile during the last 12 h period is about 500 J kg^{-1} higher than the initial value of approximately 2200 J kg^{-1}. The next question is: how significant is this increase in initial ambient CAPE. To answer this question we repeated the calculation for an SST of 30°C at a latitude of 10°N with the foregoing averaged profiles of temperature and moisture at the initial time. The

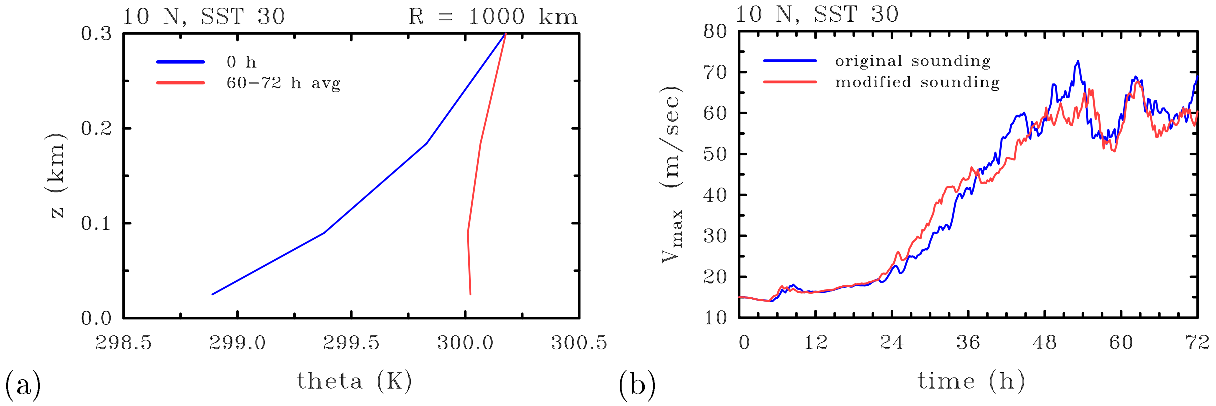

Figure 6.12: Panel (a): Potential temperature profile in the lowest 0.3 km at a radius of 1000 km (azimuthally averaged) in the CM1 calculation at a latitude of 10°N and SST of 30°C. Blue curve shows the profile at the initial time, red curve shows the profile averaged over the last 12 hours of calculation (60-72 h avg). Panel (b): Time series of maximum azimuthally-averaged tangential wind speed in the two simulations at a latitude of 10°N and SST of 30°C. Blue curve shows the evolution of v_{max} in the “original” (control) experiment. The red curve shows the evolution of v_{max} in the simulation where 60-72 h averaged ambient profile at a radius of 1000 km from the control experiment was used as the initial environmental sounding.

differences in intensity evolution between this calculation and the original one is shown in Figure 6.12b. Some small differences in the intensity evolution begin to appear after 24 h of integration, which is near the start of rapid intensification. From the study of Nguyen *et al.* (2008), such differences are to be expected on account of the stochastic nature of deep convection in the model. Between 24 h and 72 h, the standard deviation of the difference between the two intensity curves is ± 2.5 m s^{-1}, which on the basis of Nguyen *et al.*'s results would be judged to be not significant.

6.4.2 Nonaxisymmetric features

Satellite and radar observations indicate that tropical cyclones are highly asymmetric during their intensification phase and only in their mature stage do they exhibit a moderate degree of axial symmetry in their inner-core region (Montgomery and Smith 2014). This is certainly true of the calculations described here as exemplified by the patterns of vertical motion in the mid troposphere (at a height of 6.3 km) for an SST of 28°C and latitude 20°N in Figure 6.13. At 48 h the convection is organised in a partial ring (panel a) and by 72 h the ring has begun to consolidate while a band of outer convection has begun to form also (panel b). Despite this lack of complete symmetry, the arguments offered to explain the dependence of intensification rate on SST in section 6.2, as well as the arguments for the explanation of latitudinal dependence presented in section 5.2, are based on

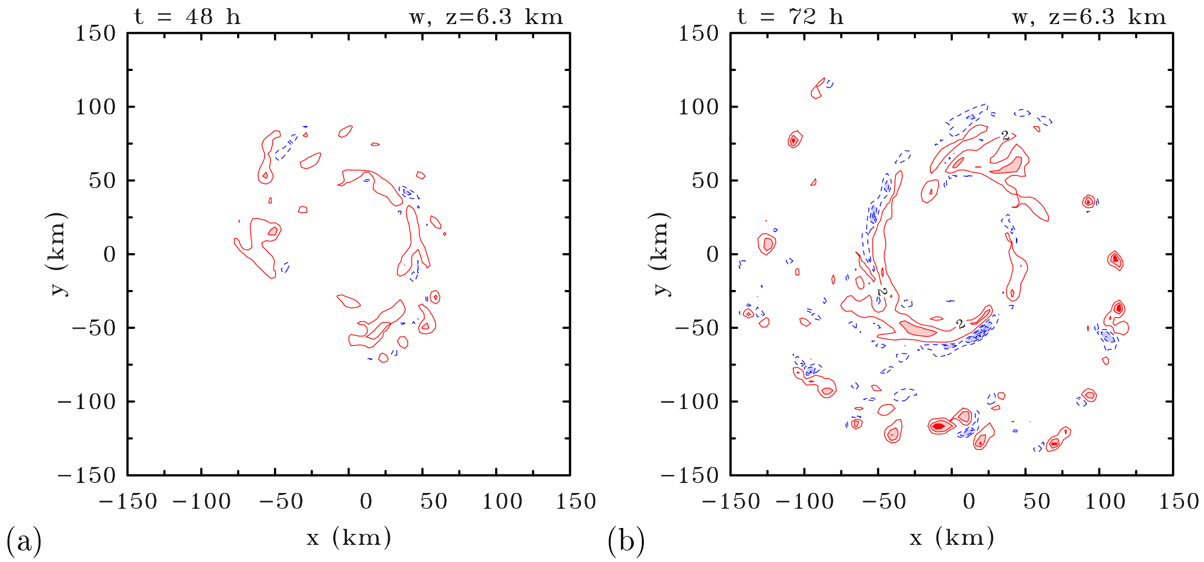

Figure 6.13: Horizontal cross sections of vertical velocity at a height of 6.3 km in the CM1 calculation corresponding to latitude 20°N and SST of 28°C at (a) 48 h and (b) 72 h. Solid red contours indicate positive values. Interval for positive contours is 4 m s^{-1}, starting with the value of 2 m s^{-1}. Values between 6 and 10 m s^{-1} are shaded pink and those greater than 10 m s^{-1} are shaded red. Dashed blue contours indicate negative values. Interval for negative contours is 2 m s^{-1}, starting with −2 m s^{-1}. Values lower than −4 m s^{-1} are shaded light blue.

an axisymmetric perspective that would apply to the azimuthally-averaged fields. More complete arguments would need to account also for eddy processes as discussed in (Persing *et al.* 2013).

Chapter 7

Summary and Outlook

7.1 Summary

Idealized numerical model experiments have been presented to examine the dependence of tropical cyclone intensification rate on both latitude and sea surface temperature (SST) in the prototype problem for tropical cyclone intensification in a quiescent environment on an f-plane. The numerical model used for the study is the three-dimensional, nonhydrostatic, state-of-the-art Bryan Cloud Model (CM1), introduced in Chapter 3.

In Chapter 4 a method to determine an axisymmetric balanced vortex with a prescribed tangential wind field distribution that is independent of latitude was reviewed. Based on this method, a tropical-cyclone-like vortex was implemented in the CM1 model as a new 3D initialization option and was used to initiate all numerical experiments carried out in this study.

In Chapter 5 the latitudinal dependence of tropical cyclone intensification was investigated. It was shown that the intensification begins earlier and is more rapid as the latitude is decreased. After considering a number of physical processes involved in the intensification of storms, it was concluded that the dynamics of the frictional boundary layer play a key role in the explanation (Smith *et al.* 2015). In an azimuthally-averaged view of the problem, the most pronounced quantitative difference between the CM1 simulations at 10°N and 30°N is the larger radial gradient of diabatic heating rate above the boundary layer at the lower latitude. These differences were attributed to the stronger vertical motion found in the middle troposphere at 10°N because the heating rate, itself, is approximately proportional to the vertical velocity. Since the values of CAPE in the 10°N calculation were found to be even slightly less than in the 30°N calculation, the differences in the vertical velocity diagnosed in the middle troposphere cannot be explained in terms of differences in updraught buoyancy. Following the work of Smith *et al.* (2015), the explanation for the stronger vertical motion at 10°N in the middle troposphere was therefore attributed to the larger vertical velocity exiting the boundary layer at this latitude.

In the context of axisymmetric balance dynamics, the stronger negative radial gradient of diabatic heating rate at 10°N produces a larger radial inflow in the low and middle troposphere, leading to an increase in the rate at which absolute angular momentum (M-) surfaces are drawn inwards. Although the radial gradient of M is larger at 30°N than at 10°N, the much stronger inflow at 10°N is sufficient to give the larger spin up rate at this latitude. These arguments for the dependence of intensification rate on latitude invoke the conventional spin up mechanism together with a boundary layer feedback mechanism linking the strength of the boundary layer inflow to that of the diabatic forcing (Smith *et al.* 2015). It was shown that the foregoing differences greatly surpass the effects of rotational stiffness (inertial stability) and evaporative-wind feedback that have been proposed in some prior studies.

The results of the CM1 calculations described above are entirely consistent with those of Smith *et al.* (2015), who used an older model with coarser horizontal resolution in their study, namely the Pennsylvania State University/National Center for Atmospheric Research Mesoscale Model (MM5).

The most important results that are novel in the tropical cyclone research field are contained in Chapter 6. Motivated by a desire to interpret observational data on tropical cyclone intensification rates, we examined the effects of changing the SST on the intensification rate of tropical cyclones at different latitudes. The results of the nine CM1 simulations taking combinations of three different latitudes (10°N, 20°N, 30°N) and three different SSTs (26°C, 28°C, 30°C) complement and extend those of Smith *et al.* (2015) examining the latitudinal dependence only. In particular, the results of the present study reveal important quantitative differences in the latitudinal dependence of intensification rate as the SST is changed. Specifically, the dependence on latitude is largest when the SST is marginal for tropical cyclone development (26°C) and reduces in significance as the SST is increased. Furthermore, it was shown that at a fixed latitude, vortex intensification begins earlier and is more rapid as the SST is increased.

A physical explanation for the dependence of tropical cyclone intensification rate on SST was offered in terms of the classical axisymmetric paradigm for tropical cyclone intensification. In brief, at a given latitude, an increase in the SST is accompanied by a significant increase in the surface water vapour fluxes and corresponding increases in the low-level moisture and equivalent potential temperature. Where boundary layer air is lofted into the vortex above, these increases lead to a larger radial gradient of diabatic heating rate in the low to middle troposphere and thereby to a stronger diabatically-forced overturning circulation. Again, the stronger inflow draws absolute angular momentum surfaces inwards at a higher rate leading to faster spin up. The difference between the radially integrated vertical mass fluxes in the middle troposphere and at the top of the boundary layer can be used as another indicator of the strength of the inner-core deep convection. It was shown that, at a given latitude, this difference increases with increasing SST, an indication that, collectively, deep convection has a progressively greater ability to ventilate the air that is converging towards the vortex centre as the SST is increased.

7.2 Future work

The foregoing explanations for the dependence of tropical cyclone intensification rate on latitude and sea surface temperature are based on an azimuthally-averaged perspective, but the flow exhibits significant departures from axial symmetry, especially during the rapid intensification phase. The flow asymmetries, which are a prominent feature of three-dimensional numerical experiments as well as of real storms, were discussed briefly, but remain a topic for future studies.

The present study of the physical processes governing the intensity change relates to hypothetical storms in environments with no background flow. However, in reality, one of the major impediments to improved intensity forecasts is believed to be associated with the interaction of a tropical cyclone with the ambient vertical wind shear (e.g., Riemer *et al.* 2010, Tang and Emanuel 2010). An extension of the present study to examine these effects would appear to be a fruitful avenue for future research.

Bibliography

[1] Blackadar AK. 1962: The vertical distribution of wind and turbulent exchange in a neutral atmosphere. *J. Geophys. Res.*, **67**, 3095-3102.

[2] Bryan GH, Fritsch JM. 2002: A benchmark simulation for moist nonhydrostatic numerical models. *Mon. Wea. Rev.*, **130**, 2917-2928.

[3] Bui HH, Smith RK, Montgomery MT, Peng J. 2009: Balanced and unbalanced aspects of tropical-cyclone intensification. *Q. J. R. Meteorol. Soc.*, **135,** 1715-1731.

[4] Dunion JP. 2011: Rewriting the climatology of the tropical North Atlantic and Carribean Sea atmosphere. *J. Climate*, **24**, 893-908.

[5] Eliassen A. 1951: Slow thermally or frictionally controlled meridional circulation in a circular vortex. *Astroph. Norv.*, **5**, 19-60.

[6] Emanuel KA. 1994: *Atmospheric convection.* Oxford University Press, Oxford, UK.

[7] Greenspan HP, Howard LN. 1963: On a time-dependent motion of a rotating fluid. *J. Fluid Mech.*, **17**, 385-404.

[8] Hendricks EA, Montgomery MT, Davis CA. 2004: On the role of "vortical" hot towers in formation of tropical cyclone Diana (1984). *J. Atmos. Sci.*, **61**, 1209–32.

[9] Kaplan J, DeMaria M. 2003: Large-scale characteristics of rapidly intensifying tropical cyclones in the North Atlantic Basin. *Wea. Forecasting*, **18**, 1093-1108.

[10] Kilroy G, Smith RK, Montgomery MT. 2015: Why do model tropical cylcones grow progressively in size and decay in intensity after reaching maturity? *J. Atmos. Sci.*, (submitted).

[11] Kepert JD. 2006a: Observed boundary layer wind structure and balance in the hurricane core. Part I: Hurricane Georges, *J. Atmos. Sci.*, **63**, 2169-2193.

[12] Montgomery MT, Smith RK. 2014: Paradigms for tropical cyclone intensification. *Aust. Met. Ocean. Soc. Journl.* (Bruce Morton Memorial Volume), **64**, 37-66.

[13] Montgomery MT, Nicholls ME, Cram TA, Saunders AB. 2006: A vortical hot tower route to tropical cyclogenesis. *J. Atmos. Sci.*, **63**, 355–86.

[14] Ooyama KV. 1969: Numerical simulation of the life cycle of tropical cyclones. *J. Atmos. Sci.*, **26**, 3-40.

[15] Nguyen SV, Smith RK, Montgomery MT. 2008: Tropical-cyclone intensification and predictability in three dimensions. *Q. J. R. Meteorol. Soc.*, **134**, 563-582.

[16] Persing J, Montgomery MT, McWilliams J, Smith RK. 2013: Asymmetric and axisymmetric dynamics of tropical cyclones. *Atmos. Chem. Phys.*, **13**, 12299-12341.

[17] Rotunno R, Emanuel KA. 1987: An air-sea interaction theory for tropical cyclones. Part II: Evolutionary study using a nonhydrostatic axisymmetric numerical model. *J. Atmos. Sci.*, **44**, 542-561.

[18] Shapiro LJ, Willoughby H. 1982: The response of balanced hurricanes to local sources of heat and momentum. *J. Atmos. Sci.*, **39**, 378-394.

[19] Shin S, Smith RK. 2008: Tropical-cyclone intensification and predictability in a minimal three-dimensional model. *Q. J. R. Meteorol. Soc.*, **134**, 1661-1671.

[20] Smith RK. 2006: Accurate determination of a balanced axisymmetric vortex. *Tellus*, **58A**, 98-103.

[21] Smith RK, Montgomery MT, Nguyen SV. 2009: Tropical cyclone spin-up revisited. *Q. J. R. Meteorol. Soc.*, **135**, 1321-1335.

[22] Smith RK, Montgomery MT. 2012: Observations of the convective environment in developing and non-developing tropical disturbances. *Q. J. R. Meteorol. Soc.*, **138**, 1721-1739.

[23] Smith RK, Montgomery MT. 2014: On the existence of the logarithmic surface layer in hurricanes. *Q. J. R. Meteorol. Soc.*, **140**, 72-81.

[24] Smith RK, Vogl S. 2008: A simple model of the hurricane boundary layer revisited. *Q. J. R. Meteorol. Soc.*, **134**, 337-351.

[25] Smith RK, Montgomery MT. 2015: Towards clarity on tropical cyclone intensification. *J. Atmos. Sci.*, **72**, 3020-3031.

[26] Smith RK, Kilroy G, Montgomery MT. 2015: Why do model tropical cyclones intensify more rapidly at low latitudes? *J. Atmos. Sci.*, **72**, 1783-1804.

[27] Smith RK, Zhang J, Montgomery MT. 2015b: The dynamics of intensification in an HWRF simulation of Hurricane Earl (2010). *Q. J. R. Meteorol. Soc.*, (submitted).

[28] Tang B, Emanuel KA. 2010: Midlevel ventilation's constraint on tropical cyclone intensity. *J. Atmos. Sci.*, **67**, 1817-1830.

[29] Wilhelmson RB, Chen CS. 1982: A simulation of the development of successive cells along a cold outflow boundary. *J. Atmos. Sci.*, **39**, 1466-1483.

[30] Willoughby HE. 1979: Forced secondary circulations in hurricanes. *J. Geophys. Res.*, **84**, 3173-3183.

[31] Willoughby HE. 1995: Mature structure and evolution. *Global perspectives on tropical cyclones.* Elsberry RL (ed.), World Meteorological Organization, Geneva.

[32] Zhu H, Smith RK. 2002: The importance of three physical processes in a minimal three-dimensional tropical cyclone model. *J. Atmos. Sci.*, **59**, 1825-1840.

[33] Zhu H, Smith RK. 2003: Effects of vertical differencing in a minimal hurricane model. *Q. J. R. Meteorol. Soc.*, **129**, 1051-1069.

Eidesstattliche Erklärung

Hiermit erkläre ich, die vorliegende Masterarbeit selbstständig verfasst zu haben und keine anderen als die in der Arbeit angegebenen Quellen und Hilfsmittel benutzt zu haben.

München, 30. September 2015

Nina Črnivec

Acknowledgements

At first I would like to thank my supervisor, Prof. Dr. Roger Smith, who provided me with the opportunity to join his team and suggested such an interesting topic for my thesis. I am extremely thankful for your guidance, valuable comments and encouragement from the start until the end of my study. Thank you for the immense knowledge you shared with me, it was so inspiring!

Furthermore, I would like to thank Prof. Dr. George Craig in advance for taking the time and examine this master thesis, and for general support.

Next, I want to thank my colleague, Dr. Gerard Kilroy, for the continuous help throughout the entire year. Thank you for introducing me the numerical model and for the assistance with all sorts of technical problems. Thank you also for the language corrections and insightful comments which improved the quality of this thesis.

I would like to thank Heinz Lösslein for helping with technical problems.

I also want to thank all other temporary members of our Tropical Meteorology Research Group - Dr. Christoph Schmidt, Sebastian Müller and Minhee Chang - for creating a nice working atmosphere. Especially, I want to thank Dr. Christoph Schmidt for his help with some translations to German.

I want to thank Dr. George Bryan for providing his numerical model.

Last but not least, I want to thank my friends and family, especially my parents, who have always generously supported me.